THE PLASMA ENVIRONMENT OF MARS

A.F. NAGY[1], D. WINTERHALTER[2], K. SAUER[3], T.E. CRAVENS[4], S. BRECHT[5], C. MAZELLE[6], D. CRIDER[7], E. KALLIO[8], A. ZAKHAROV[9], E. DUBININ[3], M. VERIGIN[9], G. KOTOVA[9], W.I. AXFORD[3], C. BERTUCCI[6] and J.G. TROTIGNON[10]

[1]*University of Michigan, Atm Oc & Space Sciences, 1416 Space Research, Ann Arbor, MI 48109, U.S.A.*

[2]*Jet Propulsion Laboratory, California Institute of Technology, 4800 Oak Grove Drive, Pasadena, CA 91109, U.S.A.*

[3]*Max-Planck-Institut für Aeronomie, Max-Planck-Str. 2, 37191 Katlenburg-Lindau, Germany*

[4]*University of Kansas, Lawrence, U.S.A.*

[5]*Bay Area Res Corp, Orinda, CA 94563, U.S.A.*

[6]*Centre d'Etude Spatiale des Rayonnements/CNRS, Toulouse, France*

[7]*Catholic University of America, Department of Physics, Washington, D.C., 20064, USA*

[8]*Finnish Meteorological Institute, Geophysical Research, Helsinki, Finland*

[9]*Space Research Institute, Russian Academy of Sciences, Ul. Profsoyuznaya 84/32, Moscow, Russia GSP-7 117997*

[10]*LPCE/CNRS, Laboratoire de Physique et Chimie, de l'Environnement, 3A, Ave. de la Recherche Scientifique, F-45071 Orleans Cedex 2, France*

(Accepted in final form 14 March 2003)

1. Introduction

When the supersonic solar wind reaches the neighborhood of a planetary obstacle it decelerates. The nature of this interaction can be very different, depending upon whether this obstacle has a large-scale planetary magnetic field and/or a well-developed atmosphere/ionosphere. For a number of years significant uncertainties have existed concerning the nature of the solar wind interaction at Mars, because of the lack of relevant plasma and field observations. However, measurements by the Phobos-2 and Mars Global Surveyor (MGS) spacecraft, with different instrument complements and orbital parameters, led to a significant improvement of our knowledge about the regions and boundaries surrounding Mars.

Figure 1.1 depicts the insights gained, primarily, from the analyses of data from the two missions. Results from theoretical work and numerical simulations helped greatly to place the observations into a self-consistent global framework. The main signatures, defined by the different plasma processes at work, can be summarized as follows:

(1) The bow shock stands off an effective obstacle at a distance expected from gas-dynamic and/or magnetohydrodynamic approximations. The thickness of the

Space Science Reviews **111:** 33–114, 2004.

magnetosheath, the region between the shock and the effective obstacle, is on the order of the solar wind proton gyro-radius, but thinner than the gyro-radius of heavy ions from the planet. Significant mass-loading takes place within the magnetosheath, indicating the existence of an extended hydrogen/oxygen exosphere.

(2) The Magnetic Pileup Region (MPR) is a region dominated by planetary ions. A well-defined boundary, the Magnetic Pileup Boundary (MPB), separates the MPR from the magnetosheath. The MPB is a thin, sharp transition that deflects where the solar wind proton density drops sharply, but not the solar wind electron density nor the solar wind magnetic field. (Previously, the MPB was called the Protonopause, the Planetopause, and various other names.) Within the MPR, on the dayside, the solar wind magnetic field piles up and prominently drapes about Mars. On the dayside, the MPR is limited from below by the ionosphere or the exobase, depending on solar wind conditions. On the nightside, the MPR is bounded by the tail region stretching far behind the planet. The MPR and the MPB are also observed at Venus and comets, and evidence is emerging that they are common features of the interaction of the solar wind with ionospheres of un-magnetized (or weakly magnetized) bodies.

(3) A plasma boundary is observed in the supra-thermal electrons ($>$ 10 eV, MGS data), which hints at the existence of a boundary between the Magnetic Pileup Region and the ionosphere below. However, without thermal ion and electron measurements at the relevant altitudes, it is impossible to determine whether this boundary is an 'ionopause' in the conventional sense. Indeed, it has long been known from Viking measurements, that the ionospheric thermal pressure at Mars is usually insufficient to balance the total pressure in the overlying Magnetic Pileup Region. Thus it is expected that the Martian ionosphere is magnetized, much like Venus' ionosphere during times of high solar wind dynamic pressure and/or low fluxes of ionizing solar radiation. The magnetic pressure associated with this ionospheric field will supplement the ionospheric thermal pressure, possibly enough to balance the overlying MPR pressure. Locally, crustal magnetic fields vastly complicate the topology of the ionosphere and the 'ionopause'.

In subsequent sections of this chapter the magnetosheath and nature of the Magnetic Pileup Region and the Magnetic Pileup Boundary will be discussed, as well as the characteristics of the ionosphere.

2. The Magnetosheath

All solar system objects that are impenetrable obstacles to the solar wind, either by having a sufficiently large intrinsic magnetic field or a dense enough ionosphere, form a bowshock. Because of the geometric aspect of an obstacle such as a planet or comet, the bow shock is detached, and the region between the shock and the

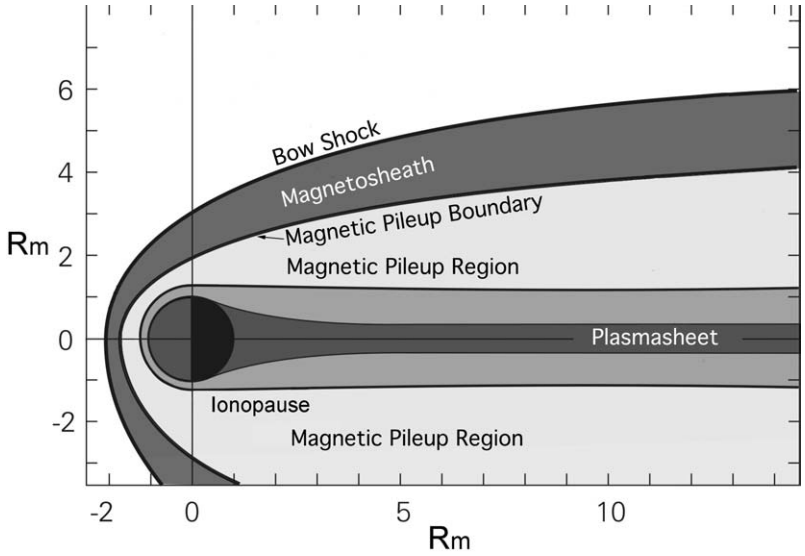

Figure 1.1. A sketch of the structure of the Martian plasma environment, depicting the major boundaries and regions in the equatorial plane. The scales R_M are Mars radii.

obstacle is termed the magnetosheath. The shock-heated and turbulent solar wind plasma and magnetic field signatures of magnetosheaths are similar from object to object, and are readily identified in the data.

In the case of objects with extended exospheres, such as Mars, Venus and comets, heavy ions of planetary or cometary origin significantly modify the overall ion dynamics within the magnetosheath. They appear to be also responsible for the deflection or termination of the solar wind proton flow at the object boundary.

At Mars, remarkable fluxes of planetary ions were observed far from the planet at the terminator bow shock ($\sim 2.8\ R_M$) (Dubinin *et al.*, 1993, 1995). It is not clear whether this observed abrupt increase in the number density of planetary ions is caused only by an increase in the impact ionization rate at the shock front. A sudden appearance of a large number of newly ionized ions (mainly protons) resembles the well-known phenomenon of the ionizing front associated with the Alfvén concept of critical ionization (e.g., Angerth *et al.*, 1962). In ionizing fronts the ionization occurs mainly at the leading edge of a neutral gas as it moves through the plasma. The hydrogen atmosphere of Mars has a large scale height and there are no reasons to expect an appearance of a narrow ionizing front. On the other hand a bow shock and ionizing front have similar substructures. They share charge separation electric fields, and drifts of the electrons in $\mathbf{E} \times \mathbf{B}$ fields, which can destabilize the wave turbulence and lead to the appearance of hot electrons that may initiate avalanche. However, estimates made by Dubinin *et al.* (1993) show that in order to support a self-sustained avalanche the number density of neutrals must be much higher than one may expect at such altitudes.

The Martian magnetosheath is of small spatial extent, with a thickness that is comparable with the gyroradius of the protons. Given the lack of space, the absence of complete thermalization of solar wind and exospheric protons is expected, and is indeed observed (Dubinin *et al.*, 1993). A feature of bi-ion plasma flows is the appearance of bi-ion waves behind the shock. These waves are related to the periodic momentum exchange between the differentially streaming proton and heavy ion fluids. Relative streaming arises because of the difference in inertia, which in turn leads to the generation of the motional electric fields in the reference frames of both streaming ion fluids and therefore results in a strong coupling between the ions. These waves may steepen and give rise to multiple shocklets. Indeed, Phobos-2 and MGS observations provide us the examples of such structures (Dubinin *et al.*, 1996, 1998; Dubinin and Sauer, 1999; Acuña *et al.*, 1998). Similar aspects of turbulent interaction between the protons and newly-born ions are also discussed by Breus and Krymskii (1992) and Breus *et al.* (1992).

Figure 2.1 shows the combined time-energy spectrogram of the proton and oxygen ion fluxes during a long pass of the Phobos-2 spacecraft through the magnetosheath region. The bow shock crossing (00:20 UT) is identified by the sudden heating of the protons. Then a gradual cooling takes place with a subsequent shock-like transition at 01:40 UT, which is accompanied by the appearance of oxygen ion fluxes. The sequence of events, starting with the sudden heating and followed by the drop in the bulk speed and subsequent cooling, is repeated several times.

The variations in the proton and heavy ion velocities are out of phase. Decreases in the proton speed are accompanied by acceleration of O^+ ions. The re-acceleration and the cooling of the protons are accompanied by a decrease of the O^+ velocity, and a broadening of their spectra. The plasma is not fully recovered after the passage of shocklets, indicative of a multiple, step-like, transition to the downstream state.

The heavy ion density increases with decreasing distance to the planet. Since the height of the potential barrier at a shocklet increases with increasing heavy ion density, one may expect that there is a distance from the planet where the solar wind protons will be unable to penetrate further, and a boundary is formed. While this boundary is impenetrable to the protons, the heavies and, importantly, the electrons carrying the magnetic field, go through it. Associated changes of the magnetic field amplitude and direction characterize the apparent border between the magnetosheath and the adjacent region. More details for this scenario of plasma boundary formation are discussed next.

3. The Magnetic Pileup Region (MPR) and Boundary (MPB)

Both Phobos-2 and MGS observations indicate that one or more boundaries exist in the lower magnetosheath across which sharp changes of the plasma and field parameters occur. For example, the magnetometers on Phobos (FGMM, MAGMA)

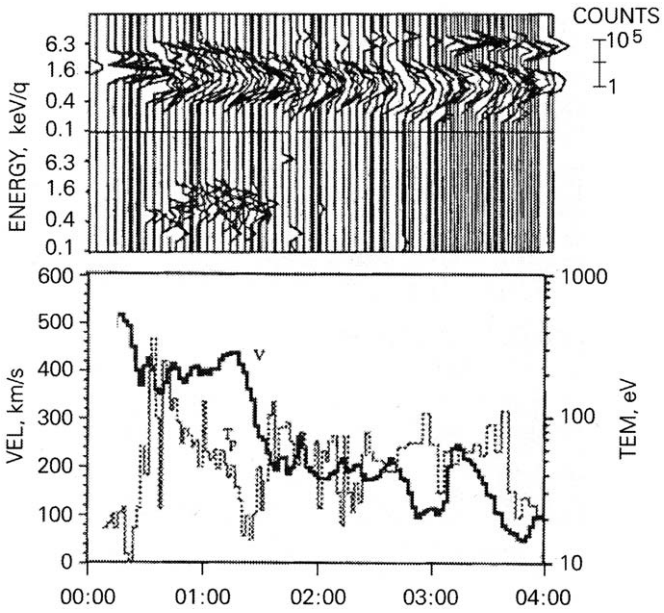

Figure 2.1. Combined energy-time spectrograms of the proton and oxygen ion fluxes measured by sunward and sideward looking sensors along Phobos-2's elliptical orbit on February 15, 1989 (top panel). The bulk velocity and temperature of the solar wind protons are in the bottom panel (from Dubinin *et al.*, 1996).

identified a boundary by a rotation of the magnetic field direction and a decrease in turbulence (Riedler *et al.*, 1989). The boundary, labeled 'Planetopause', was located at a subsolar radius of about 1.25 R_M (R_M: Mars radius). Using the Planetopause as the obstacle boundary that deflects the solar wind flow, a good fit of the observed bow shock location was obtained in gas-dynamic calculations.

Other instrument also detected boundaries. They were introduced as the magnetopause (Rosenbauer et al., 1989; Lundin et al., 1989), the Protonopause (Sauer *et al.*, 1994), and the ion composition boundary (Breus et al., 1991). However, one significant handicap that the Phobos-2 mission suffered under was the large spacecraft periapsis altitude of about 850 km above the surface. The large altitude precluded a decisive statement about the nature of the obstacle. Particularly, no conclusive evidence for the presence or absence of an intrinsic magnetic field could be obtained. The situation fundamentally changed when MGS went down to around 100 km, repeatedly, for many periapses.

Figure 3.1 shows the magnetic field magnitude recorded by MGS during an early elliptical orbit during which the spacecraft explored all the interaction regions from the solar wind to a low altitude periapsis. The bow shock (BS) and an inner 'cavity boundary' (CB) are clearly observed both inbound and outbound. The most prominent signature in this time series of the magnetic field strength is the sudden, strong and sharp jump observed on both sides at the location marked 'MPB' where

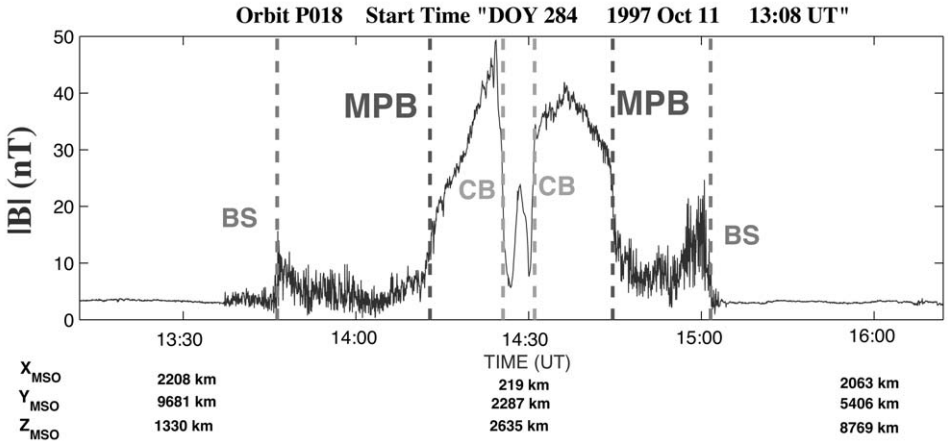

Figure 3.1. Magnitude of the magnetic field recorded by Mars Global Surveyor during an early elliptical orbit (October 11, 1997) around the periapsis (14:28 UT, altitude 120 km, 17.6 local time) displaying the major plasma boundaries symmetrically on both sides (after Mazelle *et al.*, 2002): BS, MPB and CB denote the bow shock, the magnetic pile-up boundary and the magnetic 'cavity boundary', respectively. The horizontal axis shows both time and the spacecraft coordinates in the Mars-centered solar orbital (MSO) system (the X-axis points from Mars to the Sun, the Y-axis points antiparallel to Mars' orbital velocity, and the Z-axis completes the right-handed coordinate system).

MPB stands for the 'Magnetic Pile-up Boundary'. The field magnitude increases dramatically by a factor of about 3 (e.g., outbound) over the very small distance of the order of 100 km. Moreover, the MPB clearly separates two very different regions: a magnetosheath with low amplitude and turbulent magnetic fields, and a region of high pile-up fields, the 'Magnetic Pile-up Region', where the solar wind magnetic field is piled-up and draped about the ionosphere. A similar magnetic pile-up region was found to be present at Venus (Zhang *et al.*, 1991).

The name of the boundary, Magnetic Pileup Boundary, arbitrarily emphasizes the behavior of the magnetic field. Equally correct would have been other names from the literature emphasizing other plasma components, or an instrument-neutral designation such as 'Mantle Boundary' and 'Mantle'. But after long discussions among investigators from both missions, the 'Magnetic Pile-up Boundary' and 'Magnetic Pile-up Region' terminology was adopted. The more important point is that after the analysis of all available plasma parameters from Phobos-2 and Mars Global Surveyor a better understanding of the boundary's physical nature was obtained. Below, a summary of Phobos-2 and Mars Global Surveyor observations is given which will help to clarify that the several boundaries observed in the magnetosheath are one and the same plasma boundary.

3.1. THE MAGNETIC PILEUP BOUNDARY

The MPB is always present, even when no 'cavity boundary' is observed. Figure 3.2 illustrates such a case with the bow shock and MPB crossings detected by

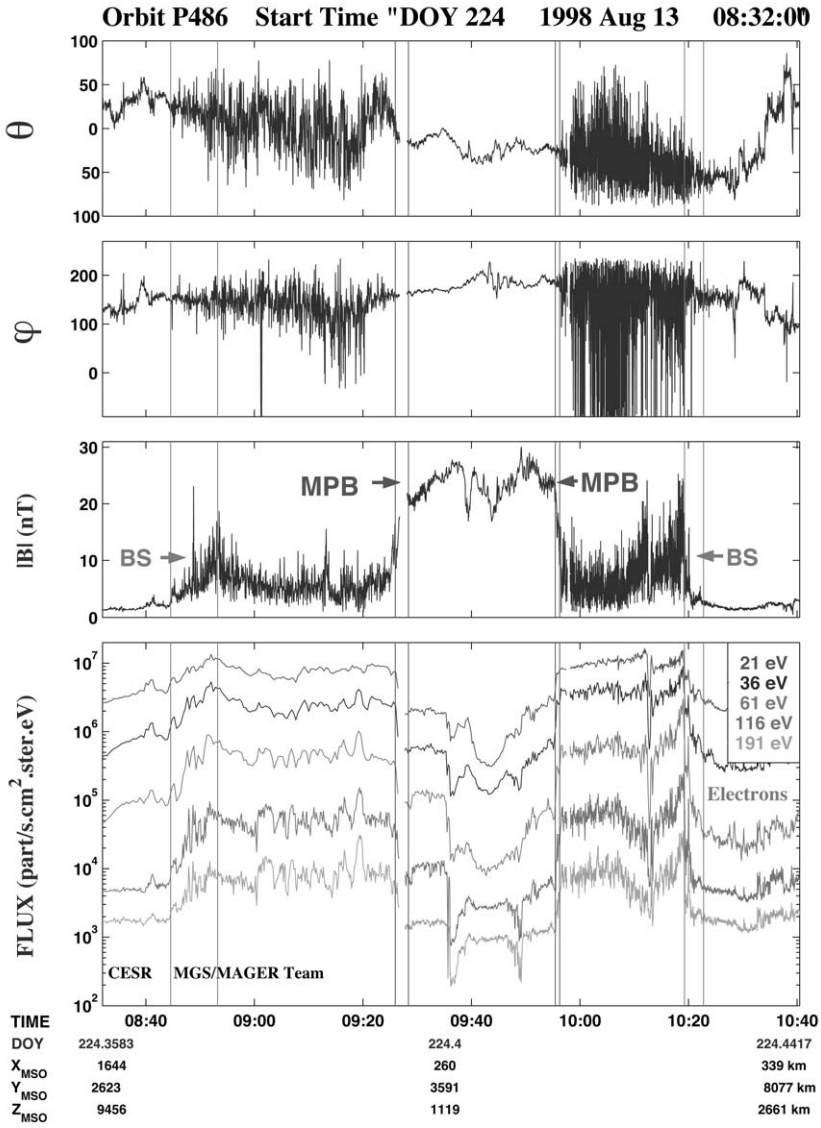

Figure 3.2. Magnetic field and electron data recorded by the Mars Global Surveyor MAG/ER experiment on August 12, 1998 (after Vignes *et al.*, 2000). The three upper panels display the elevation, azimuth angles and the magnitude, respectively, in the MSO system. The lower panel depicts electron fluxes for five energy ranges.

the Mars Global Surveyor magetometer/electron reflectometer (MAG/ER) experiment near the dawn – dusk meridian plane. The coordinate system used is the Mars-centered Solar Orbital (MSO) coordinate system: the X-axis points from Mars to the Sun, the Y-axis points antiparallel to Mars' orbital velocity and the Z-axis completes the right-handed coordinate system. The magnetic field azimuth (with $\varphi = 0$ antisunward here), elevation with respect to the (X, Y) plane and amplitude are plotted in top panels 1, 2 and 3. The last panel shows the electron fluxes for five energy ranges labeled with their geometrical mean energy. Each bow shock (BS) and MPB crossing is indicated between two vertical lines showing the apparent thickness of the boundary. The magnetosheath which can be defined as the region between the bow shock and the MPB is characterized by a huge variability both in the field magnitude and direction, which is particularly obvious on the two upper panels of the figure.

The MPB is revealed as a sharp discontinuity where the magnetic field magnitude suddenly rises by a factor between 2 and 3, where a strong reduction of the field's directional variability occurs, and where the suprathermal electron fluxes dramatically drop by often more than one order of magnitude (see, e.g., the 61 and 116 eV electron fluxes in Figure 3.2). The MPB signature in the field magnitude is sometimes less obvious when observed near noon local time, but both the sharp change in the field direction and the variability, and the change in the electron fluxes are always clearly observed for every crossing from the magnetosheath to the MPR. All the MPB crossings are thus identified in the MGS data by three simultaneous signatures: a more or less sharp increase of the magnetic field magnitude, a correlated reduction of the electron fluxes for energy greater than 10 eV, and a decrease in the fluctuations of the magnetic field.

The Plasma Wave System (PWS) aboard Phobos-2 recorded the spectra of plasma waves in the frequency range 0–150 kHz and also measured the plasma density using a Langmuir probe (Grard *et al.*, 1989a, b). Figure 3.3 shows an example of wave measurements during the fourth elliptical orbit of Phobos-2. The bow shock and the MPB were encountered on February 11, 1989 at 11:03 UT and 11:24 UT, respectively. As can be seen, the signatures of both plasma boundaries are quite clear in the PWS data. The parameters shown are from top to bottom: (1) the dynamic spectrogram of the wave electric field measured by the dipole antenna in the range 3–60 decibels above 1 μV m^{-1}Hz$^{-1/2}$, (2) the root-mean-square of the current collected by the cylindrical Langmuir probe, (3) the high frequency variation of this signal, (4) the electric field averaged over the 100 Hz–6 kHz frequency bandwidth, and (5) its high frequency variation.

The bow shock is followed by a significant increase in the level of the broadband emissions (top panel), which are thought to be electroacoustic noise associated with the dissipation of the solar wind kinetic energy. This wave activity fades away as Phobos-2 approaches the MPB (Grard *et al.*, 1989, 1991, 1993). Panels 3 and 5 (from the top) also reveal that the plasma turbulence usually observed behind the shock decreases and reaches a minimum in front of the MPB. Here the Langmuir

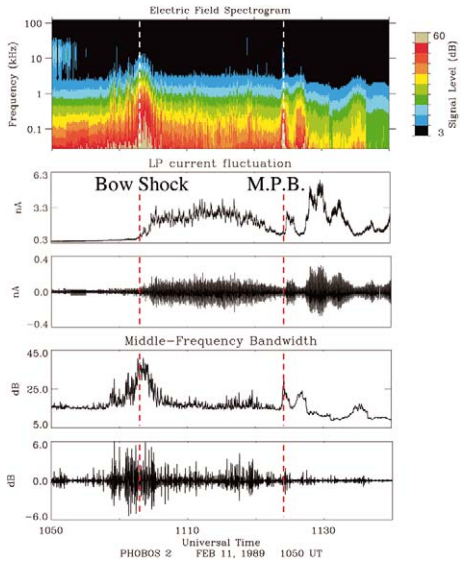

Figure 3.3. Electric field and plasma measurements in the Martian space environment from the plasma wave system onboard Phobos-2. From top to bottom: electric field spectrogram, Langmuir probe current fluctuation, high frequency variation of it, intensity of the electric field averaged over the 100 Hz−6 kHz frequency bandwidth, and high frequency variation of this signal. Crossings of the bow shock and MPB at 11:03 UT and 11:24 UT, respectively, are marked.

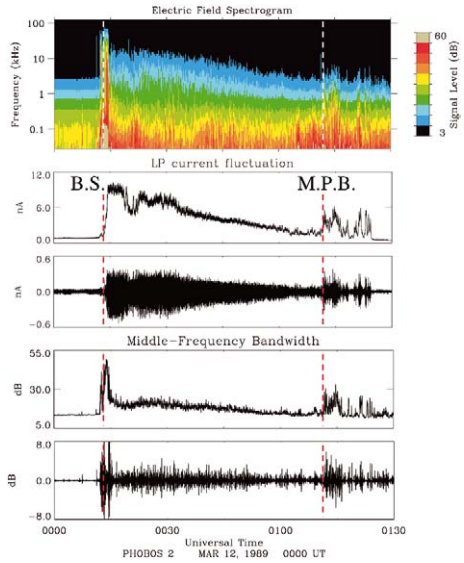

Figure 3.4. Similar to Figure 3.3. The bow shock, and MPB, were encountered along one of the Phobos-2 circular orbits around the red planet at 00:13:30 UT and 01:11:30 UT on March 12, 1989, respectively.

probe current fluctuation is very low (panel 2), indicating a low electron plasma density.

The broadband activity then suddenly increases again as seen in panel 1, and in the turbulence level (panels 3 and 5), as well as in the electron plasma density (panel 2). Thermal electron populations, called plasma clouds, reminiscent of the Venus plasma clouds, are indeed commonly observed behind the MPB. Their density may be as high as 700 cm^{-3} and their temperature is on the order of 10^4 K (Grard *et al.*, 1989, 1991). This is confirmed by the PWS parameters plotted in Figure 3.4, which is similar to Figure 3.3. Here, Phobos-2 crossed the shock at 00:13:30 UT, and the MPB at 01:11:30, March 12, 1989.

The magnetic field measurements are well correlated with the PWS data in identifying both the bow shock and the MPB (Figure 3.5). At the MPB the magnetic field rotation and the drop in the magnetic turbulence level is co-located with the characteristic PWS signatures as described above. The jump in the Langmuir probe current at the MPB indicates a strong increase of the electron density.

Direct measurements of the dynamics of protons and planetary ions by the plasma instruments TAUS and ASPERA are of essential importance for the understanding of the nature of the Magnetic Pile-up Boundary. Figure 3.6(a) depicts the first elliptical orbit of Phobos-2 on February 1, 1989 (Rosenbauer *et al.*, 1989), showing illustratively the inbound crossings of the bow shock and the MPB on the dayside, and outbound crossings in reverse order in the tail. Figure 3.6(b) shows the energy-time spectrogram of ions measured by TAUS along this orbit. The narrow distribution of the solar wind protons (left panels) is suddenly being heated and slowed at approximately 18:15, indicating passage through the bow shock. A short time later, at roughly 18:35, the proton flux is effectively terminated. At the same time planetary ions appear (right panel) (Rosenbauer *et al.*, 1989). The drop of the proton density at about 18:35 UT coincides with the inbound MPB position determined from the magnetic field measurements (Riedler *et al.*, 1989; Sauer *et al.*, 1990, 1992). The planetary ion fluxes continue to a distances of about 10 R_M. The change back to the solar wind (magnetosheath) ion composition occurs at about 23:30 UT, where the MPB is crossed outbound.

The outbound MPB crossing is also shown in Figure 3.7, where ASPERA density measurements and TAUS data are plotted together with the MAGMA magnetic field variation (Lundin *et al.*, 1989). The MPB is marked by the steep decrease in magnetic field amplitude and the strong change of the B_x component. Crossing this boundary from the MPR towards the magnetosheath side, the density of planetary ions (thin line) decreases, whereas the proton density (thick line) simultaneously increases.

A last example of multi-instrument detection of the MPB is given in Figure 3.8. Measurements are shown during one of the Phobos-2 closest approaches to the dayside of Mars, on February 8, 1989. The top panel represents the magnetic field magnitude. The bow shock was crossed at 05:35 UT. The decrease in the floating potential (second panel), which is positive in the solar wind due to photoelectrons,

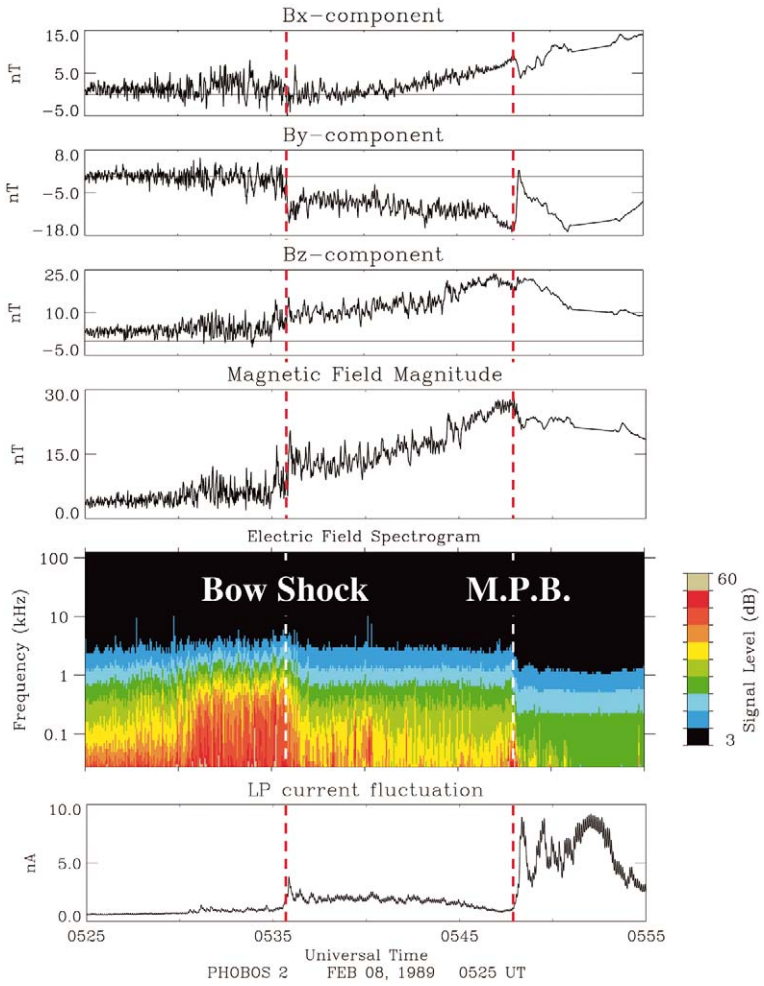

Figure 3.5. Magnitude and orientation of the magnetic field vectors measured during the third Phobos-2 elliptical orbit (Riedler *et al.*, 1989) (top four panels). Electric field dynamic spectrogram and root-mean-square of the current collected with the PWS Langmuir probe (bottom two panels). The crossings of the bow shock (05:35:50 UT) and MPB (05:48 UT) are marked by vertical dashed lines.

is caused by an increase in the density of ambient electrons. The electron number density (third panel) is derived from the measurements of the potential difference between the conducting spacecraft at floating potential and the negatively biased electric field probe. The results of the Langmuir probe, which could measure only a dense plasma ($n_e > 10\ \mathrm{cm}^{-3}$), are shown in the fourth panel. The next two panels depict the proton number density and the bulk speed measured by the ASPERA. At 05:48 UT, at the altitude of 880 km, the magnetic field reached a maximum and the proton fluxes dropped. However, in contrast to the entry into a true Earth-like magnetosphere, a sudden increase in the electron number density was observed.

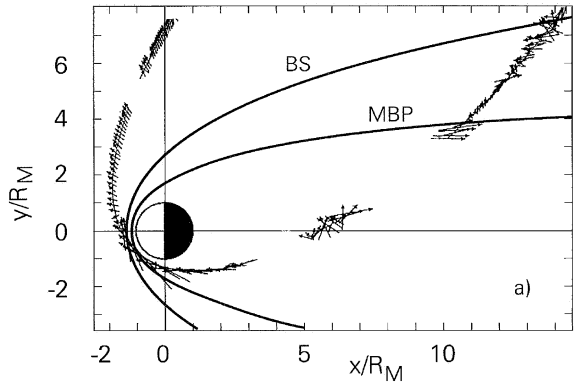

Figure 3.6. (a) View of the plasma boundaries in the equatorial plane, with arrows depicting the magnetic field vectors measured by Phobos 2 along the elliptical orbit on February 1, 1989. (b) Energy-time spectrograms of ions measured by TAUS during that orbit. The fluxes of the solar wind protons, left panel, and heavy ions ($m/q > 2$) of planetary origin, right panel, are shown (from Rosenbauer *et al.*, 1989). The crossings of the bowshock and MPB are indicated at the left.

This increase in n_e corresponds to the appearance of the planetary ions (the seventh panel). The bottom panel shows the wave activity in three frequency ranges. The increase of the wave activity at 05:48 UT in the frequency range of 5–50 Hz was attributed to the interaction between the two ion populations (Grard *et al.*, 1991).

3.2. THE MPB LOCATION AND SHAPE

Attempts to characterize the location and shape of the boundary in the lower magnetosheath were first carried out using the Phobos-2 measurements. The major obstacles to a clear characterization were (1) the basic nature of the boundary (e.g., magnetopause versus Venus-like, etc.), and (2) the relative small number of boundary crossings by the spacecraft. Although there was no consensus of what kind of boundary it was, there were little doubts about its existence.

These problems were resolved by the Mars Global Surveyor mission, which showed that there is no global intrinsic magnetic field (and therefore no magnetopause), and which crossed the boundary many thousand times. With these measurements it is clear that this is a plasma boundary, that is formed by the interaction of the solar wind with the Martian exosphere/ionosphere. Furthermore, this kind of boundary may in fact be a general characteristic associated with non-magnetic solar system bodies which are surrounded by a gaseous envelope.

The MPB crossing locations inferred from the Phobos-2 PWS observations are shown in Figure 3.9 (diamonds). The off-center models of the bow shock (solid line) and MPB (dotted line) derived by Trotignon *et al.* (1993, 1996) are also displayed. On the vertical axis, $(Y'^2+Z'^2)^{1/2}$ is the distance of the Phobos-2 spacecraft from the aberrated tail X' axis, where (X',Y',Z') denote the aberrated Mars solar orbital system. It is worth noting that the orbital motion of the planet makes the

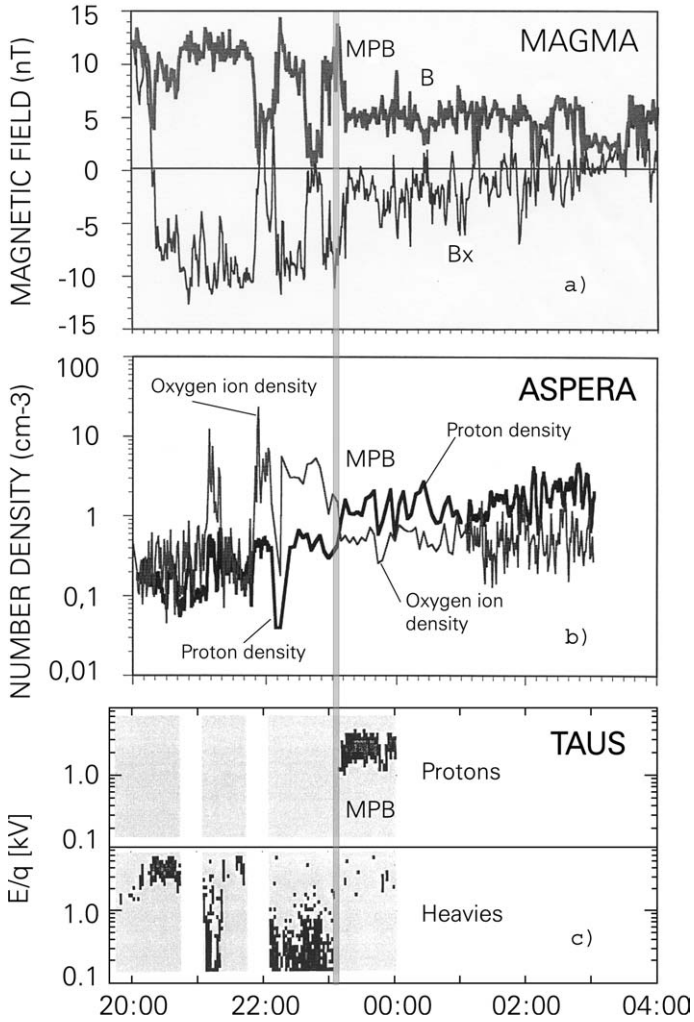

Figure 3.7. For the outbound crossing of the MPB at about 23:30 UT on February 1–2, 1989 seen in Figure 3.6, the magnetic field magnitude and x-component are shown in the top panel. The number density of protons (thick line) and planetary ions (thin line) are displayed in the center panel. The bottom panel displays the energy/charge measurements for this interval.

apparent direction of the solar wind flow deviate from the anti-sunward direction, therefore a 4° aberration angle has to be considered. Moreover, a better fit to the observations is obtained by allowing the foci of the conic, used to derive the bow shock and MPB models, to lie along the X' symmetry axis, as opposed to being fixed on the origin, i.e., the planet center (Slavin and Holzer, 1982).

Figure 3.9 also shows that there are only four observations on the dayside, and none near the sub-solar point. For this reason two conic sections were used to best fit the observed MPB locations: one on the night side of Mars, for $X' < 0$, and the

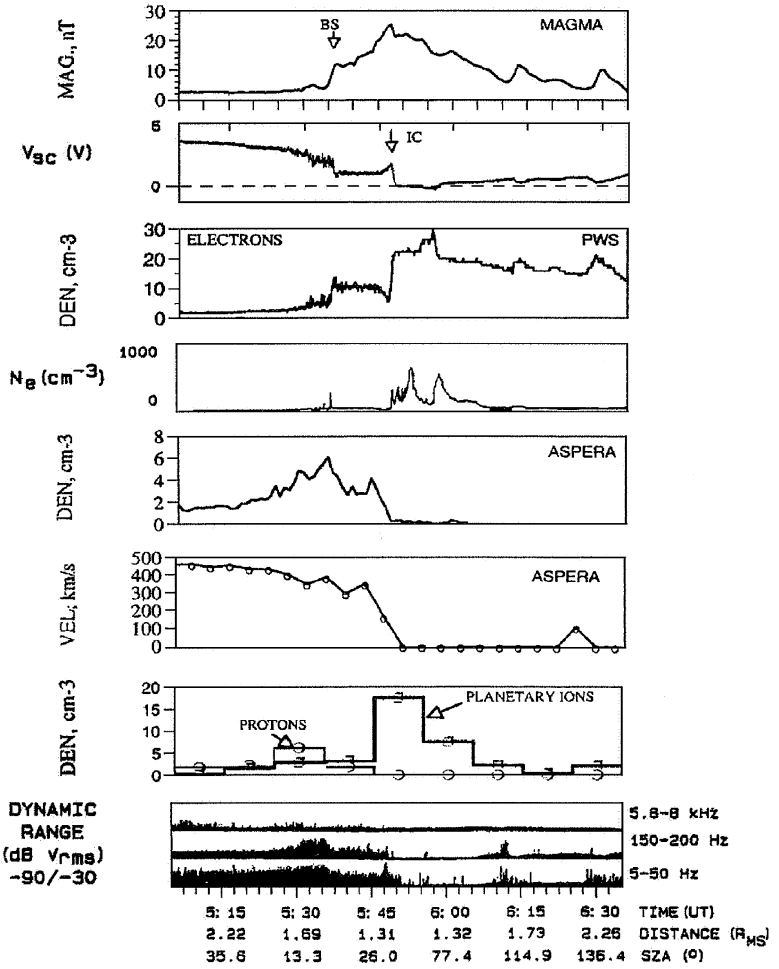

Figure 3.8. From top to bottom are the magnetic field magnitude, the spacecraft potential, the electron number density derived from the potential measurements, the x-component of the proton velocity, the density of planetary ions, and the electric field fluctuations in three frequency ranges along Phobos-2's third elliptical orbit on February 8, 1989 (from Dubinin *et al.*, 1996).

other on the dayside, for $X' > 0$. The night side fit was calculated first, because most of the crossing events occurred there. The dayside conic was then obtained by ensuring the continuity in amplitude and derivative between the two conics at $X' = 0$ (Trotignon *et al.*, 1996). The solid line in Figure 3.9 is the result of this process.

From this analysis the average planetocentric standoff distance of the MPB was found to be about 1.2 R_M (4050 km) at the subsolar point, and 1.4 R_M (4640 km) at the terminator, where Mars' radius R_M was taken to be 3390.5 km. These values are in good agreement with the ones given by Riedler *et al.* (1989), and Verigin *et al.* (1993). The Martian tail diameter was found to be 4.2 R_M at $X' = -2.3\ R_M$,

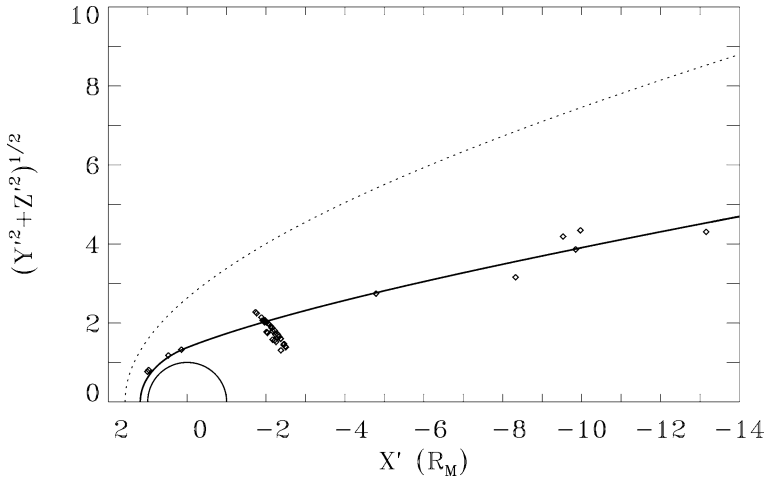

Figure 3.9. Crossings of the Magnetic Pile-up Boundary identified from observations by the plasma wave system aboard Phobos-2. There are 45 crossings (diamonds), of which only 4 are on the dayside. Models of the bow shock (dotted line) and the MPB (solid line), as derived by Trotignon *et al.* (1993, 1996). (X',Y',Z') are the aberrated Mars solar orbital coordinates in units of Mars radii R_M ($1R_M = 3390.5$ km); A 4° aberration angle was considered.

and 7.6 R_M at $X' = -10\ R_M$. The Martian tail diameter (normalized by the planet's radius) appears to be about twice as large as the width of the Venus' induced magnetotail. Some interpreted the large diameter of the tail, reasonably so, as evidence for the presence of an intrinsic global magnetic field (e.g., Verigin *et al.*, 1993).

The Mars Global Surveyor measurements have now anchored many of the Phobos-2 observational uncertainties. The MPB was crossed by MGS during most of the elliptical orbit phases of the mission. During this phase of the mission, the highly inclined orbital plane explored a large range of local times and solar zenith angles, although the coverage was not uniform (for instance there is no data for MPB crossings below 20° solar zenith angle).

Figure 3.10(a) displays 488 MPB crossings by MGS from September 12, 1997 to August 29, 1998, in aberrated cylindrical coordinates (from Vignes *et al.*, 2000). The overall shape of the MPB was obtained by fitting an axi-symmetric conic section to the observed boundary crossings. The post-terminator crossing positions are much more variable than the ones on the dayside, and are not always easily identifiable. The magnetic signature of the MPB often appears to be weak and gradual at $X' < -2\ R_M$. This is at least in part due to the crossing geometry, since MGS crosses the boundary more tangentially in the post-terminator regime. The difficulties in identification may be reflected in the increased scatter of the data points far from the terminator (cases with poorly defined crossings were not included in this study).

The average planetocentric stand-off distance of the MPB was found to be about 1.3 R_M (4400 km) at the subsolar point, and about 1.5 R_M (5000 km) at the ter-

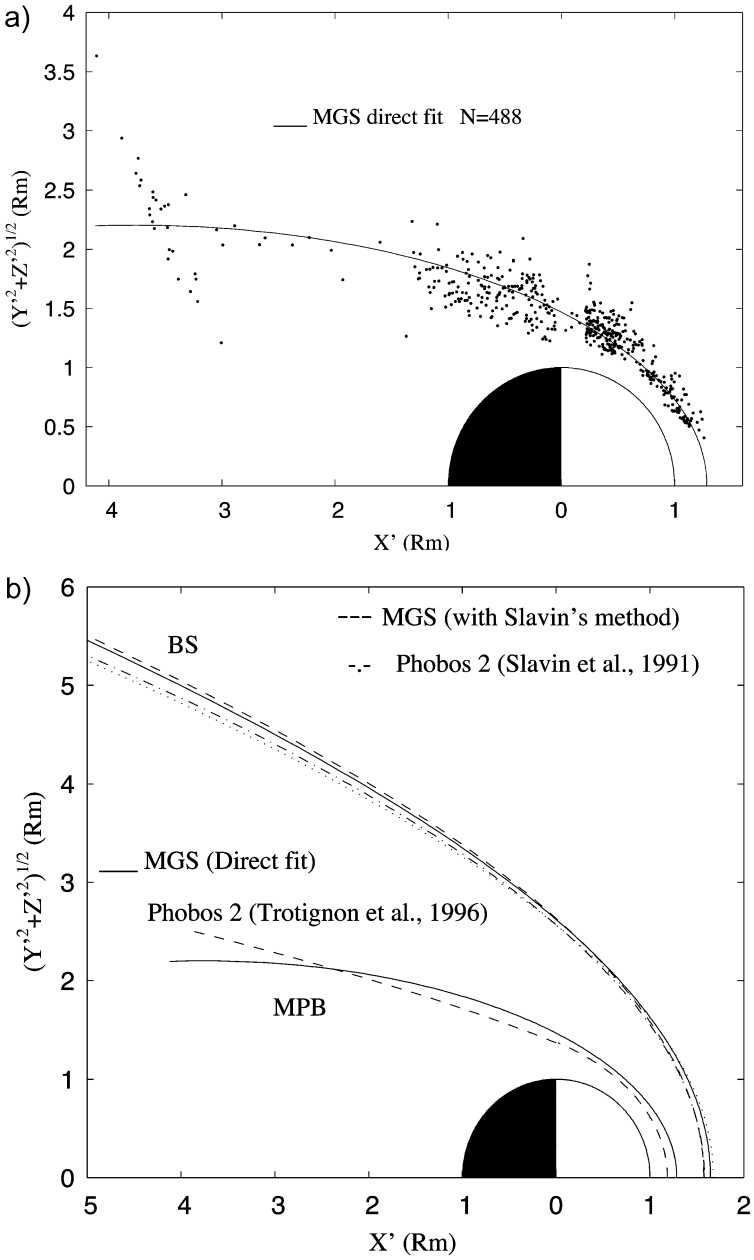

Figure 3.10. (a) MPB fit from MGS crossings during the first year of the mission in aberrated Mars-centered Solar Orbital (MSO) coordinates; (b) Comparison between Martian BS and MPB fits from MGS and Phobos-2 in aberrated MSO system (from Vignes *et al.*, 2000).

minator, using $R_M = 3390$ km. These values are in reasonably good agreement with the ones given by Trotignon *et al.* (1996) from a similar study using the 45 Phobos-2 'Planetopause' crossings in the equatorial plane (see Figure 3.9).

Figure 3.10(b) from Vignes *et al.* (2000) compares the shape and location results of the MPB inferred from these two studies and also helps to visualize the relative location of the MPB compared to the bow shock. The resulting fits for the MPB are very close, especially in view of the fact that Trotignon *et al.* (1996) used different criteria to define the boundary crossings, and had only 4 boundary crossings available on the dayside.

These results show that Phobos-2 and MGS explored the same plasma feature in the environment of Mars, the MPB, and that the MPB is a permanent plasma boundary. The location of the MPB is highly variable on a day-to-day basis. Its altitude seems to depend on planetary latitude especially in the southern hemisphere, which is the region that contains the strongest crustal magnetic fields (Crider *et al.*, 2002). But the high variability can also be produced by plasma processes associated with mass loading, such as the variation of the local convective electric field. This is the case for the bow shock, which is sensitive to variations of the upstream IMF orientation (Vignes *et al.*, 2002). The Phobos-2 and MGS missions occurred during very different phases of the solar cycle, but Figure 3.10(b) reveals that the mean bow shock locations appear very consistent.

Taking a subset of the MGS MPB crossings to filter out the effects of the crustal magnetic fields in the southern hemisphere and the possible pickup ion asymmetry in IMF coordinates due to the electric field direction, the distance of the MPB at the terminator is 241 km (or 20%) closer to Mars on average when the solar wind pressure exceeds 1.1 nPa, as shown in Figure 3.11. The response of the MPB to solar wind pressure may be indicative of a residual/leakage magnetic field resulting from the anomalies. Krymskii *et al.* (2002) discuss such a leakage of magnetic flux from the southern hemisphere.

3.3. Magnetic field draping

The magnetic field morphology of the solar wind interaction with Mars, just like the solar wind interaction with Venus and comets, is dominated by the 'draping' of interplanetary magnetic field (IMF) lines around the planet. In fact, most of the current understanding of magnetic field draping comes from investigations of Venus and comets starting with Alfvén's (1957) theory and subsequent applications (e.g. Luhmann, 1986; Schwingenschuh *et al.*, 1987; Cloutier *et al.*, 1999; Mazelle *et al.*, 2002). Figure 3.12 is a sketch depicting the magnetic field lines, and the parameters defining the draping geometry.

Locally, the field is expected to be predominately horizontal relative to a spherical surface on the dayside, or $|B_\phi| \gg |B_r|$, where B_ϕ is the azimuthal component of the magnetic field, and B_r is the radial component in spherical coordinates. The angle that the magnetic field makes to the local horizontal is the inclination

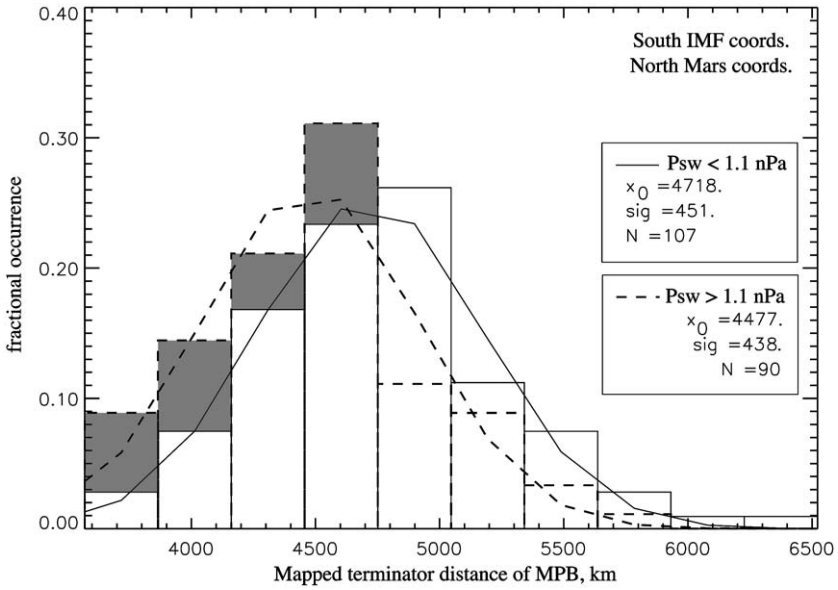

Figure 3.11. Histograms showing the distance of MGS MPB crossings mapped to the terminator plane. The shaded histogram includes all crossings in which the upstream solar wind ram pressure was greater than 1.1 nPa. The white histogram shows the lower solar wind pressure crossings. The curves are the Gaussian fits to the histograms. The associated parameters are shown in the boxes. x_0 is the average MPB distance (mapped to terminator plane) in km, sigma is the width of the gaussian, N is the number of points included in the distribution (from Crider *et al.*, 2003).

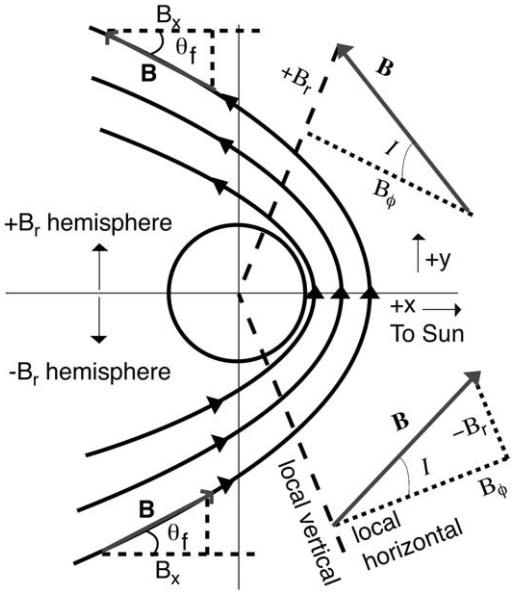

Figure 3.12. Sketch depicting the geometry of draped magnetic field lines at Mars. Positive x is toward the Sun, $+z$ is up from the ecliptic plane.

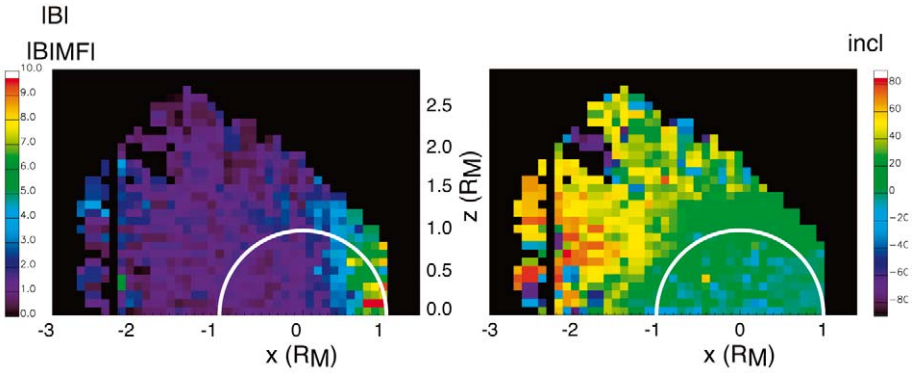

Figure 3.13. The left-hand panel is the MGS composite of the magnetic field magnitude around Mars. The right side shows the inclination angle as a function of position (see text).

angle, or $i = \arcsin(B_r/|\mathbf{B}|)$. In the dayside magnetosheath, the inclination angle is assumed to be small, and to have its sign vary with hemisphere. That is, in the upper half of Figure 3.12 the radial component is small and points away from the planetary center, giving rise to a positive angle i. In the lower half of the figure, B_ρ is towards the planet, yielding a negative i. The magnetic field in the tail is oriented more nearly radial than it is on the dayside. One determines the average direction of the induced magnetotail using the flare angle, θ_f. The flare angle is defined as the angle the magnetic field makes with the x-axis, $\theta_f = \arccos(B_x/|\mathbf{B}|)$.

The most comprehensive data set regarding magnetic field draping comes from the Mars Global Surveyor spacecraft owing to its extensive coverage in altitude and local time during its elliptical orbit mission phase. Crider *et al.* (2001, 2002) used the MGS data to determine the average magnetic field configuration resulting from the solar wind interaction with Mars. The data are grouped in spatial bins that are cubes with length of 0.1 R_M per side. Each segment of an MGS orbit that falls within a bin contributes one magnetic field value to the bin average. The images in Figure 3.13 are the projection of these bins onto a single half-plane. The left panel is the magnitude of the field and the right panel is the inclination angle.

The average draping parameters found for certain regions of interest are summarized in Table 3.1. The magnetic field values in this survey are all taken from positions far away from known crustal magnetic sources. Therefore, the topology is due primarily to the solar wind interaction.

The left panel in Figure 3.13 shows that the magnetic field magnitude ($|\mathbf{B}|$) is highest in front of the planet. $|\mathbf{B}|$ decreases with increasing solar zenith angle and increasing altitude. The right panel in Figure 3.13 shows a large green area close to the planet where the magnetic field is primarily horizontal. The average inclination angle, $\langle i \rangle$, increases from 0° at local noon to 10° at the terminator. Note that these values are adjusted in sign by hemisphere such that a positive value is expected (Crider *et al.*, 2001).

TABLE 3.1
Draping parameters from the Mars Global Surveyor magnetometer data.

Parameter	Average	Standard dev.
$\|\mathbf{B}\|$ (day)	20.7	$\pm$1 4.7
$\|\mathbf{B}\|$ (night)	11.6	$\pm$ 7.6
θ_f (day)	57.6	$\pm$ 26.6
θ_f (night)	40.0	$\pm$ 27.8
i (day)	5.6	$\pm$ 13.6
i (night)	12.5	$\pm$ 33.6

Crider *et al.* (this issue) also find that the inclination angle increases with altitude on the dayside. On the night side, the magnetic field tends to be highly inclined to the local horizontal. This is the magnetic field geometry that is expected in the magnetotail (e.g., McComas *et al.*, 1986). Nearly radial magnetic fields, such as these, have strong implications for the existence of night side ionospheric holes at Mars, as were observed at Venus (Marubashi *et al.*, 1985). However, the possibility remains that the magnetic field in the Martian wake contains a significant contribution from magnetic flux of planetary origin that leaks out into the tail (Krymskii *et al.*, 2002).

Bertucci *et al.* (2003a) studied the variation of draping across the MPB, using the simple approach shown in Figure 3.14. As the MGS trajectory crosses field lines closer and closer to the planet , it is clear that $|B_x|$ should tend to increase due to draping. However, one must consider the 3-dimensional field geometry. Figure 3.14 shows a $y-z$ projection at some $x > 0$ of the IMF transverse component $\mathbf{B_T}$ with its two cylindrical component B_r and B_t, as well as the projected MGS trajectory. A consideration of successive slices at different x positions helps to show that in a draping regime, the changes in B_x will be accompanied by a variation of $\mathbf{B_T}$ such that its radial cylindrical component B_r and B_x will be correlated. In the Martian magnetosheath, the magnetic field direction is highly variable and, despite the incipient draping, no correlation would be expected. However, in the magnetic pileup region, the magnetic field becomes more regular and stable, and in general, $|B_x|$ is smaller than the transverse component $|B_T| = (B_y^2 + B_z^2)^{1/2}$. The latter is a necessary condition for draping to exist.

The results of the correlation analysis between B_x and B_r are summarized in Figure 3.15 for one representative MGS orbit. In the Martian magnetosheath, upstream of the MPB (panel on the left), the lack of correlation shows that the draping is undetectable. In contrast, in the magnetic pileup region (downstream of the boundary), the very high linear correlation coefficient reveals a dramatic

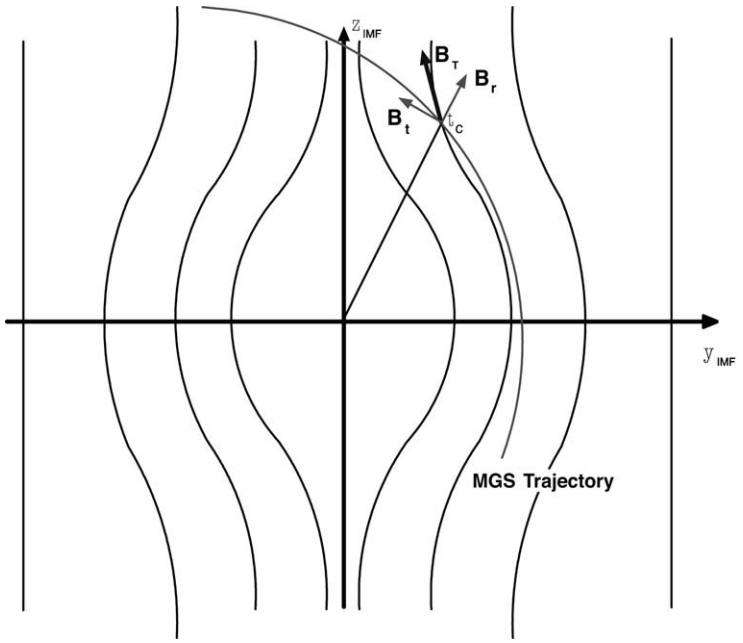

Figure 3.14. Slice perpendicular to V_{SW} of the 3D field line pattern and projection of the MGS trajectory, containing the spacecraft position at some $x_{IMF} > 0$. B_r is the radial cylindrical component of the transverse magnetic field B_T at the spacecraft position. The draping at Mars revealed by the correlated variation between $B_{x'}$ and B_r (Bertucci *et al.*, 2003a).

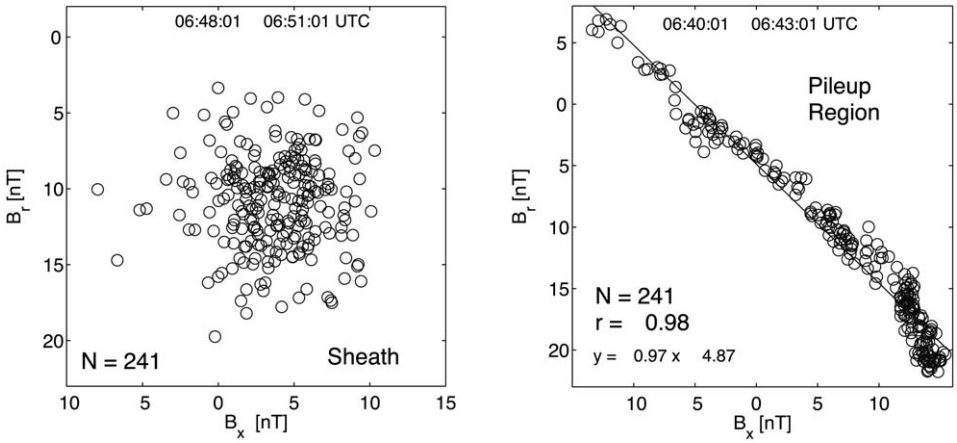

Figure 3.15. $B_{x'}$ versus B_r in the Martian magnetosheath (left panel), and in the pileup region (right panel) for a representative MGS orbit. In each panel, the number of points (N) and the correlation coefficient (r) corresponding to the best linear least-square fit is shown (Bertucci *et al.*, 2003a).

increase in the draping as the magnetic field configuration becomes regular (right panel). This striking result shows that the Martian MPB represents the outer edge of the region where the draping effect becomes prominent. Furthermore, this feature can be used to identify the MPB, especially when the signature on the magnetic field intensity is ambiguous.

The draping enhancement across the MPB is a common feature also at comets. In particular, Israelevich *et al.* (1994) have used this same method with the Giotto spacecraft magnetometer data and obtained very similar results at comet P/Halley. The MPB (crossed on the dayside) separates the cometary magnetosheath, where there is no evidence of significant draping, from the magnetic pile-up region where there are strongly draped fields. Similar properties have also been observed for the MPB crossing (also on the dayside) by the Giotto spacecraft at comet P/Grigg-Skjellerup (Neubauer *et al.*, 1993), and across the magnetic tail of comet P/Giacobini-Zinner by the ICE satellite. Slavin *et al.* (1986) report turbulent, weakly draped magnetic fields in the ionosheath, while at the interior of the tail boundary the magnetic field increases in magnitude and adopts a draped configuration. The latter observation enforces the idea that not only at comets, but also at Mars, the magnetotail boundary and the MPB are one and the same plasma boundary (Neubauer, 1987; Mazelle *et al.*, 2002). Recently, Bertucci *et al.*, (2003b), using the same method as Bertucci *et al.*, (2003a), reported a strong enhancement of the magnetic field draping at the outer part of the magnetic barrier region at Venus as a clear evidence for a magnetic pileup boundary.

3.4. Observations of low frequency waves at the MPB

Compared to the broad spectrum of waves usually observed in the magnetosheath, the vicinity of the Martian MPB often contains well-defined compressive, low frequency waves. This should not be surprising, since around the MPB plasma properties, such as the plasma $\beta(= 8\pi nkT/B^2)$, and the particle anisotropy, change significantly. Figure 3.16 shows MGS MAG/ER data for a $\sim$ 10 a.m. local time orbit (Bertucci *et al.*, 2002). The MPB is crossed a few seconds after 04:36 UTC, at $\sim$ 700 km altitude. On both sides of the boundary the magnetic field, steady in direction, displays high-amplitude compressive fluctuations. The timescale of these fluctuations is of the order of a few tens of seconds (typically, 20s), well below the local proton gyrofrequency on both sides of the boundary. On the upstream side, the oscillations in $|B|$ are 'tooth shaped', i.e., a series of dips superimposed on a nearly constant background value (type '1'). Inside the MPB, the waves are quasi-monochromatic and much more coherent (type '2'). An analysis of the MAG data together with the ER data at both sides of the MPB is very useful in order to identify the modes to which these waves are associated. An examination of the suprathermal electron fluxes shows that they are anticorrelated with $|B|$ upstream from the MPB, while downstream, the two quantities are correlated (vertical point-

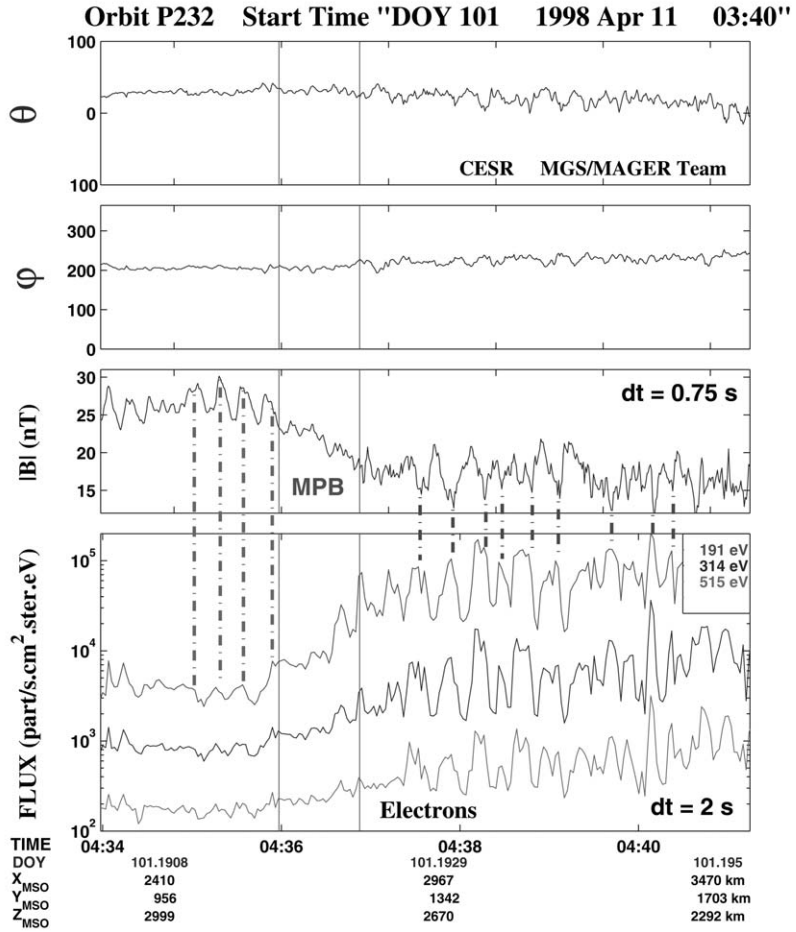

Figure 3.16. Observations by MAG/ER of compressive, linearly polarized low frequency waves around the MPB for an orbit for $a \sim 10$ a.m. local time orbit. Point-dashed lines emphasize the anti-correlation (correlation) between the electron fluxes and $|B|$ upstream (downstream) from the boundary, revealing mirror mode-like (fast mode-like) waves, respectively (from Bertucci *et al.*, 2002).

dash lines). In this figure, only the 190–520 eV range is depicted for clarity, but the same behavior is observed in all suprathermal energies ($E > 10$ eV).

For each wave event, an ambient field vector B_0 is computed by time-averaging the individual vector measurements over the event duration. By defining a mean field coordinates system with one axis along B_0, one can separate the wave magnetic field component along this direction (the compressive component $B_\parallel$), from the perpendicular components. On both sides of the MPB, the oscillatory signal is primarily in the $B_\parallel$ component. This means that the waves are linearly polarized along $\mathbf{B}_0$. The minimum variance analysis (MVA) gives wave vectors $\mathbf{k}$ nearly perpendicular to $\mathbf{B}_0(\theta_{KB} = 89°$ and $88°$, upstream and downstream from the MPB

respectively). Computation of the aflvénic magnetic field wave components in the direction $\mathbf{k}\times\mathbf{B}_0$, and magnetosonic wave components along $\mathbf{k}\times(\mathbf{k}\times\mathbf{B}_0)$, also shows that the oscillations are fully reproduced in the magnetosonic component alone. For numerous MGS orbits the low frequency waves observed in close vicinity of the MPB are always compressive and linearly polarized, with propagation nearly normal to $\mathbf{B}_0$. Such waves are observed neither in the magnetosheath proper (closer to the bow shock) nor in the solar wind. The occurrence of these waves is another characteristic feature of the Martian MPB. As a result of a survey of 282 MPB crossings by MGS, type 1 waves occur in at least 48%, type 2 waves in at least 27%, and both modes simultaneously in at least 18% of the observations. Finally, at least 11% of the observations show neither type 1 nor type 2 waves.

The characteristics of the waves upstream from the boundary (linearly polarized, quasi-perpendicular propagation, anti-correlation between $|B|$ and the suprathermal electron density) are those of mirror mode waves. This purely kinetic mode is stationary in the plasma frame ($\omega_r = 0$) for a homogeneous medium. It is driven by anisotropies in the plasma pressure ($\beta_\perp/\beta_{||} > 1 + 1/\beta_\perp$, where $\beta_\perp$ and $\beta_{||}$ are the perpendicular and parallel plasma β), especially when β is high. At Mars these waves have length scales of several upstream proton gyroradii, which is consistent with theoretical properties. One of the possible sources for generating anisotropies is the heating of the ion population (mainly perpendicular to $\mathbf{B}$) downstream from quasi-perpendicular shocks. However, mirror mode waves at Mars appear to be independent of the shock's geometry. On the other hand, they appear always attached to the boundary, as if they are generated upstream from the MPB, grow and are convected down to the MPB in the decelerated flow. Distributions (likely highly non-gyrotropic) of newborn pickup ions (especially heavies, e.g., O^+) also contribute to large $\beta_\perp$ values upstream from the MPB, where the β is high since the ambient magnetic field has a low magnitude on average, and the thermal pressure of the shocked solar wind is high. In the case of comets, mirror-mode waves have been reported on the outer side of the magnetic tail boundary of P/Giacobini–Zinner (Tsurutani *et al.*, 1999). This is more evidence of the connection between the dayside MPB and the magnetic tail boundary.

The properties of the waves downstream from the MPB (type 2) coincide with those of magnetosonic fast-mode waves, and their nature is very different from that of mirror mode waves. Moreover, the β strongly decreases at the MPB since the magnetic pressure is much higher in the MPR, and the hot solar wind particle populations are replaced by colder populations of planetary origin. Thus, downstream of the MPB, the plasma becomes stable to the mirror mode, and the mirror mode waves are replaced by magnetosonic fast-mode waves. However, in light of their large amplitude and the small scale of the MPR, it is difficult to explain the fast mode waves as arising from locally growing plasma microinstabilities (especially ones with perpendicular propagation). Alternatively, the waves can be interpreted as stationary, bi-ion waves standing downstream of the MPB (e.g., Sauer *et al.*, 1990). Interestingly, the same relationship of mirror mode and fast magnetosonic

mode (Mazelle *et al.*, 1989) was reported by Mazelle *et al.* (1991) at both sides of comet P/Halley MPB. In a related study, Glassmeier *et al.* (1993) suggest an equivalent interpretation for the waves at the MPB. However, further studies still need to be done in this respect.

3.5. THE NATURE OF THE MPB/MPR – DISCUSSION

The extensive magnetic field measurements by MGS down to altitudes below 100 km established that at present there is no planetary dynamo operating in Mars. While the remnant fields are locally strong, they are too weak to stop the solar wind, on a global scale, at the observed distances. Thus the interpretation of the 'obstacle boundary' as a magnetopause is, in the classical sense, inappropriate.

Further, since the first spacecraft measurements around Mars it has been known (or at least strongly suspected), that the ionospheric pressure is also typically insufficient to stop the solar wind at the observed distances. Therefore, an alternate explanation of the interaction is required.

If one combines the results of Phobos-2 and MGS data analyses, the signatures of the Magnetic Pile-up Region and the Magnetic Pile-up Boundary can be summarized as follows:

(1) Moving from the magnetosheath to the MPR, the magnetic filed piles up, accompanied by magnetic field rotation.
(2) There is a drop in the magnetic field fluctuations.
(3) There is a drastic change of ion composition: the proton density decreases, commensurate with an increase of planetary ion density.
(4) There is a sharp increase of the electron density.
(5) The electron temperature drops.
(6) Localized high-frequency emissions appear.
(7) The MPB is a permanent feature of the interaction.
(8) Two interaction mechanisms that potentially could account for all or part of these characteristics are charge exchange, and mass loading.

Breus *et al.* (1989), Ip (1992) and Ip *et al.* (1994) have suggested that charge-exchange of the solar wind protons with an oxygen-rich atmosphere may cause the termination of the proton fluxes. However, Lichtenegger *et al.* (1997) have shown that this process can only lead to a significant depletion of the solar wind in a small region above the subsolar region at low altitudes. The absorption by oxygen leads to a significant effect only below about 1500 km, while neutral hydrogen has only a small influence on the solar wind loss at Mars.

A complication in the charge-exchange calculation is the relatively large gyroradius of the protons compared with scale of the system. Consideration of their finite gyroradius indicates that the path through the absorption region is elongated, effectively increasing the losses. Nevertheless, the total absorption near the terminator in the altitude region between 500 and 1500 km is only about 1% to 6% (similar to Venus (Gombosi *et al.*, 1981)). It is worth noting that the calculations by

Lichtenegger *et al.* (1997) were made for solar-maximum conditions, which were appropriate for the Phobos observations.

Lichtenegger and Dubinin (1999) reexamined the mechanism of charge-exchange, motivated by the MGS results and in anticipation of Nozomi mission results. They used the model by Krasnopolsky and Gladstone (1996) to calculate the solar wind absorption for solar minimum and solar maximum conditions. At solar minimum, when the density of hydrogen constituents (H and H_2) is expected to be much higher, the absorption was found to reach more than 20%. The neutral densities are too low at the required distances, therefore it was thought unlikely that charge-exchange processes are dominantly responsible for the observed proton flux termination.

Sauer *et al.* (1990, 1992, 1994, 1995) have suggested that the sharp boundary terminating the access of the solar wind is caused by the direct interaction of the solar wind protons with heavy ions of planetary origin, a mass-loading process. In addition to the features related to the extended atmosphere, the importance of the ion gyroradius effect is unique at Mars. The pick-up gyroradius of the O^+ ions significantly exceeds the characteristic size of the system upstream of the bow shock, and it becomes comparable with the magnetosheath width at closer distances. In such a configuration a relative streaming of the different ion species is possible. The existence of a second ion population leads to an additional coupling between the ions and electrons through the Lorentz forces and the charge neutrality requirement. Even a small admixture of heavy ions into a proton-electron plasma significantly modifies the flow properties (Dubinin and Sauer, 1999). These issues are discussed further in the Section 6, 'Theory and Modeling'.

4. The Tail Region

The first measurements in the Martian tail were obtained during the Mars-5 mission (Gringauz *et al.*, 1975; Dolginov *et al.*, 1976a; Vaisberg *et al.*, 1975). The measurements led to a qualitative demonstration of the compressibility of the Martian magnetotail with increasing solar wind ram pressure. A boundary layer was revealed, and measurements of ion spectra with unusually high energies also led to speculations concerning the existence of the magnetotail plasma sheet, even though Mars-5 did not reach the inner region of the Martian tail (Dolginov *et al.*, 1976b; Gringauz *et al.*, 1976).

The plasma investigations of the Phobos mission for the first time measured directly the features of the deep tail region, as well as the plasma characteristics in the equatorial region of the Martian tail (the MGS orbits did not include the tail region to an appreciable extend).

4.1. HINTS OF A PLANETARY MAGNETIC FIELD

It is well known that the typical distribution of the electrons in the solar wind is asymmetrical in the wings, because of halo electrons streaming out from Sun along the interplanetary magnetic field. Dubinin *et al.* (1994) have applied the measurements of the electrons in the wings as tracers of the field lines, because streaming electrons have to replicate field line kinks associated with the draping of the IMF around Mars. This approach provides a very sensitive tool for the study of magnetic field topology. Figure 4.1 illustrates this method.

In the solar wind, due to the halo component, the antisunward/sunward asymmetry of the electron fluxes is positive. The draping of the IMF around Mars changes the field direction in some regions and therefore changes the anisotropy of the electron fluxes. In the region where the B_x-component changes sign, because of draping, the sunward flux exceeds the antisunward flux.

While the B_x-component changes sign many times during the tail crossing, the variations in the anisotropy of the halo electrons generally replicates the variations in B_x well, thus indicating that the flux tubes encountered by the spacecraft were populated by halo electrons and thus connected to the IMF. This is an indication that the magnetic field around Mars is primarily induced. On the other hand, there are a number of tail crossings with anomalous characteristics. Figure 4.1 (bottom) shows one such example.

The magnetic field shows a rather stable orientation with respect to the current sheet separating the two lobes. Suprathermal electrons trace the field variations except in the region bounded by the dashed lines. The drop in the electron flux by a factor 3–5 is an interesting feature. A violation of the electron tracing suggests that this region of the tail may be magnetically disconnected from interplanetary space. These observations were considered as indirect evidence of an intrinsic magnetic field. The measurements made by Phobos-2 only covered the near equatorial region. The more recent MGS observations (Acuna *et al.*, 1998) have demonstrated that the regions with strong crustal magnetization, those that can give rise to the observed anomalies in the tail, are mainly localized in the mid and high latitudes of the southern hemisphere.

Further indirect evidence of the presence of a Martian magnetic field came from radio observations of the night-time ionosphere. The single frequency radio-occultations during the primary and extended Mariner 9 missions did not detect its existence (Kliore *et al.*, 1972, 1973). Subsequent and more sensitive dual-frequency Mars 4,5 radio experiments revealed the existence of the Martian night-time ionosphere, with an electron density peak of about 5×10^3 cm^{-3} (Vasiliev *et al.*, 1974) (also, see the Ionosphere section below). However, Viking 1 and 2 showed that this peak occurs only about 40% of the time (Zhang *et al.*, 1990b). Phobos-2 measured typical electron fluxes of $\sim 2 \times 10^8$ cm^{-2} s^{-1} in the magnetotail, and Verigin *et al.* (1991a;b) and Haider *et al.* (1992) suggested that these fluxes are responsible for the measured ionospheric densities (Figure 4.2). Further, they

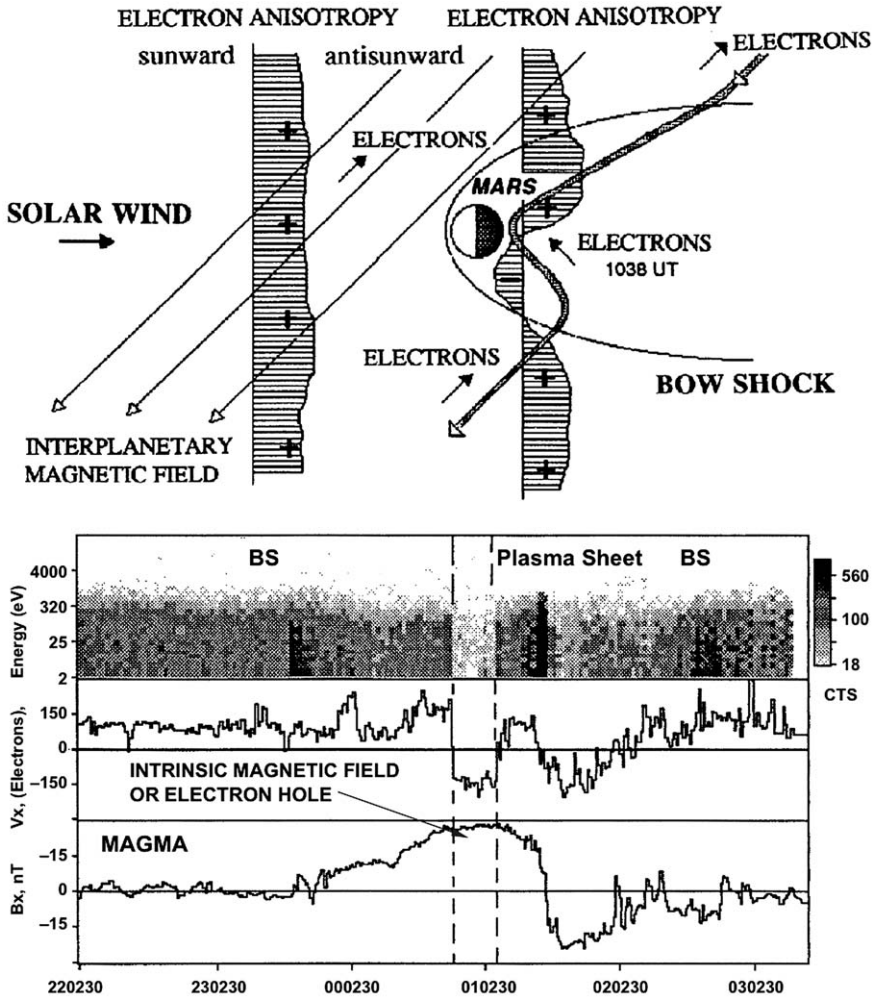

Figure 4.1. (a) A sketch depicting how the halo component of the solar wind electron flux streaming along the interplanetary magnetic field lines traces the magnetic field topology near Mars. Electron fluxes measured by sunward and antisunward looking sensors of the ASPERA instrument in the solar wind will see the antiparallel streaming (left), even in the region where the B_x component of the IMF changes sign because of draping around Mars (right) (from Dubinin *et al.*, 1994). (b) Phobos-2 orbit on March 2, 1989. The interruption of the electron flux in the time interval marked by dashed lines, and the fact that the change in flux occurs without a correlated change in B_x, gives a hint that Phobos-2 encountered flux tubes that are not connected with the IMF (from Dubinin *et al.*, 1994).

proposed that a weak intrinsic magnetic field, partially screening the Martian nightside atmosphere, might frequently prevent magnetotail electrons from reaching the ionosphere.

Finally, straightforward analysis of Martian magnetotail boundary crossings by the Phobos 2 orbiter indicated that equatorial crustal magnetization appears to in-

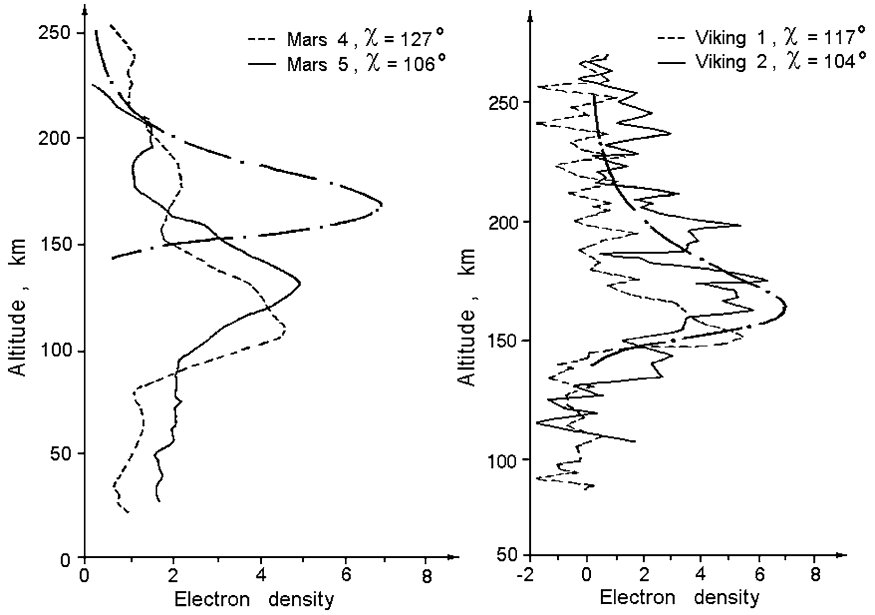

Figure 4.2. The electron density (in units of 10^3 cm^{-3}) profiles in the Martian night-time ionosphere as measured with Mars 4 and 5, and Viking 1 and 2 radio-occultations. Also shown is the calculated electron density (dash–dot). χ is the zenith angle of the point where radio beam was tangent to planet (from Verigin et al., 1991b).

fluence its location (Verigin *et al.*, 2001). Qualitative analysis demonstrated that the magnetotail thickness can be affected significantly by a region of enhanced crustal magnetization, if this region is located in the vicinity of the planetary terminator. The smoothed dashed line in Figure 4.3, which is passing through the MPB (called 'magnetopause' in the reference) positions observed under intermediate ρV^2 conditions (5×10^{-9} dyn cm^{-2} $< \rho V^2 <$ 1.4×10^{-8} dyn cm^{-2}), separates the observations corresponding to low and high ram pressures. This curve has definite bulges, corresponding to enhanced magnetotail thickness, in the ranges of areographic longitudes of about 30°–80°, 120°–160°, 210°–270°, and 300°–340°. These four longitude ranges correspond well to the regions of enhanced magnetization of the Martian crust as reported by Acuña *et al.* (1999). Specific local displacement of the magnetotail boundary downstream of these regions were estimated to be ∼500–1000 km.

4.2. Magnetic field topology

A good insight into the formation of the Martian magnetotail was obtained by observations during the multiple crossings of the tail by the Phobos 2 orbiter. Yeroshenko *et al.* (1990) found that the magnetic field in the magnetotail can be organized into two tail lobes with 'to' and 'away' from Sun directions of the

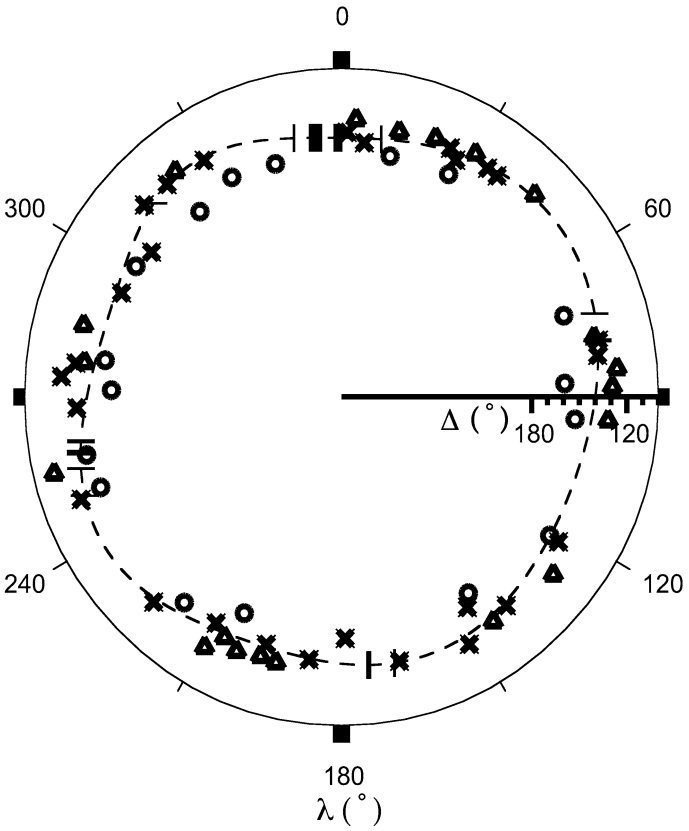

Figure 4.3. Dependence of the tail boundary zenith angle (Δ), observed by Phobos 2, on the east areographic longitude, λ. Boudary locations (i.e., Δ) observed during intermediate ρV^2 conditions (5×10^{-9} dyn cm^{-2} $< \rho V^2 < 1.4 \times 10^{-8}$ dyn cm^{-2}) are denoted by x. The boundary locations observed during low and high solar wind pressures are denoted by triangles and circles, respectively. The dashed line is smoothly drawn through the intermediate locations. The bulges occur at longitudes of strong crustal fields (from Verigin et al., 2001).

magnetic field (Figure 4.4), separated by a thin magnetic neutral sheet. This ordering was achieved by rotating the original reference frame around the solar wind velocity vector until the perpendicular component of the interplanetary magnetic field was aligned with the Y-axis of the rotating reference frame. Presence of the two tail lobes in the rotating reference frame, confirmed later by Schwingenschuh *et al.* (1992a) with the use of a wider data set, provided evidence for the inductive character of the Martian magnetotail.

Similar to the geomagnetic tail, the magnetic field intensity, B_t, in the Martian magnetotail provides pressures balance, with the external solar wind ram pressure ρV^2 and, hence, B_t should be a function of this pressure. Figure 4.5 presents experimental confirmation of this expected dependence, obtained with the use of TAUS

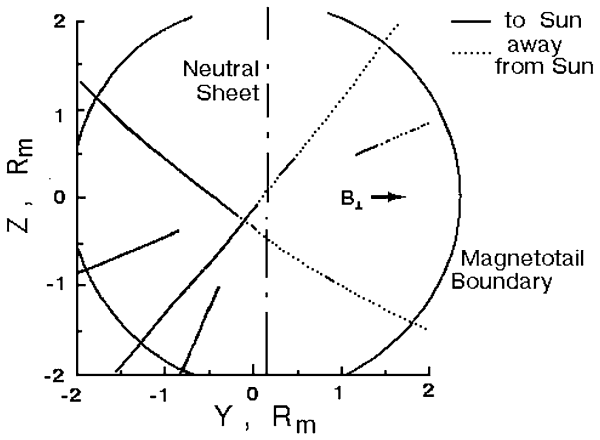

Figure 4.4. The magnetic field in the tail is separated into two lobes (see text) (from Yeroshenko et al., 1990).

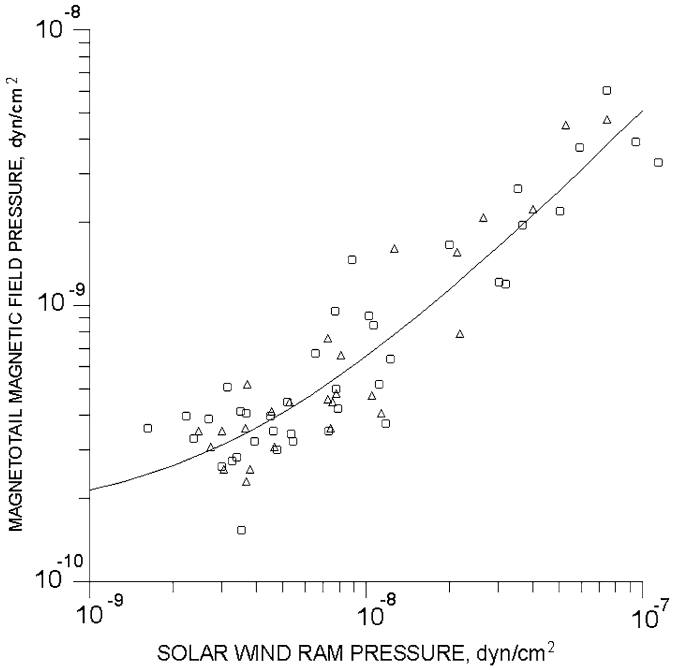

Figure 4.5. Dependence of the magnetic field pressure in the Martian tail on the solar wind ram pressure. Entry and exit of Phobos 2 into and out of the magnetotail are denoted by the dash and Δ symbols, respectively (from Rosenbauer et al., 1994).

and MAGMA data (Rosenbauer *et al.*, 1994). The smooth curve in this figure is the theoretical dependence, given as:

$$B_t^2/8\pi = \rho_p V^2 \sin^2\alpha + p. \tag{4.1}$$

The best-fit coefficients are, $sin^2\ \alpha \approx 0.049 \pm 0.004$ and $p \approx (1.7 \pm 0.3) \times 10^{-10}$ dyne cm^{-2}. Coefficient $\alpha \approx$ arc $\sin(\sqrt{0.049}) \approx 13°$ is just the average flaring angle of the Martian magnetotail boundary at the Phobos 2 orbit. This flaring angle turned out to be considerably less than the geomagnetotail flaring angle at comparable distances ($\approx 22°$), but exceeded the one for the purely induced Venusian magnetotail ($< 9.5°$). Thus, at that time, it was concluded that both intrinsic and induced magnetic fields play an important role in the solar wind interaction with Mars (Rosenbauer *et al.*, 1994).

More detailed information on the shape of the Martian magnetotail, under different solar wind ram pressures, can be found in the tables presented by Verigin *et al.* (1997). The tail region and its correlation with upstream solar wind parameters (e.g., IMF and dynamic pressure) was also studied by Slavin *et al.* (1984), and Luhmann *et al.* (1991), and modeled by Lichtenegger *et al.* (1995).

There are several properties which make Mars a unique object for studying the interaction between the solar wind and a planetary body. This is partly due to the crustal magnetic field (Connerney *et al.*, 1999), which is relatively small and localized so that it cannot play a major role in the interaction as do the magnetic fields of planets like Earth, Jupiter or Saturn. In this respect, Mars is more similar to Venus than it is to Earth.

The induced magnetotail forms as a result of the atmospheric mass loading and subsequent draping of passing magnetosheath flux tubes that sink into the wake. In general, planetary bodies without intrinsic magnetic fields, but with substantial atmospheres, are known to possess such cometlike induced magnetotails.

Phobos-2 observations, as well as MGS observations on the dayside (see relevant section regarding draping, above), have shown that the magnetotail of Mars consists of two lobes of sunward and antisunward fields, their polarity being controlled by the orientation of the cross flow component of the interplanetary magnetic field (Yeroshenko *et al.*, 1990; Schwingenschuh *et al.*, 1992a). Although these measurements suggest an induced nature of the Martian magnetotail (like that of Venus), the lack of observations in the polar regions of the magnetotail cannot exclude the possible existence of a hybrid-like tail for Mars (Dubinin and Podgorny 1980; Axford, 1991), emanating from the magnetic anomalies discovered by Mars Global Surveyor (Acuna *et al.*, 1998; Connerney, 1999).

The hybrid or combined character of the solar wind interaction with Mars is also supported by the results of a spectral analysis of the Phobos-2 magnetic field data (Möhlmann *et al.*, 1991) and the modulation of the tail diameter found in the plasma data (Verigin *et al.*, 2001). The flaring of the Martian tail was investigated (Zhang *et al.*, 1994) and it was found that the magnetotail is similar to the Earth's tail in its dependence on the pressure of the solar wind. The draping at low altitudes

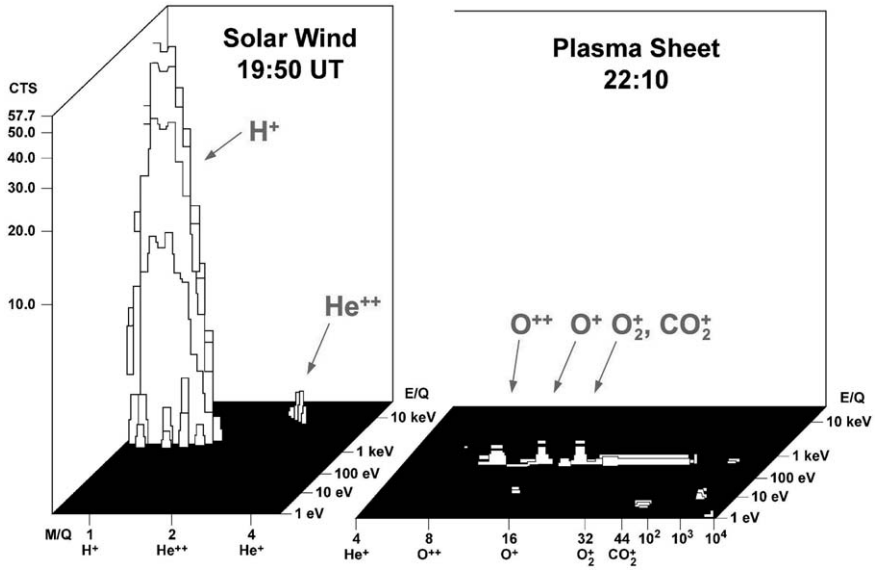

Figure 4.6. $E/q - M/q$ matrix measured by the ASPERA instrument on March 25, 1989 in the solar wind and plasma sheet. The plasma sheet contains mainly ions of the planetary origin. The planetary ions gain the energy (E/q) of about 1 keV q^{-1} (from Dubinin *et al.*, 1993a).

has been investigated using MGS data and was found to be better defined above the ionosphere than in the ionosphere (Crider *et al.*, 2001).

4.3. Plasma acceleration processes in the martian tail

The central tail is the region where energy of the magnetic field, accumulated from the flux of solar wind kinetic energy, is transferred back to the plasma. So far the Phobos 2 orbiter has provided the only plasma measurements in the deep planetary tail. Plasma instruments TAUS (Rosenbauer *et al.*, 1989) and ASPERA (Lundin *et al.*, 1989) revealed that the tail of the Martian magnetosphere has a significant population of planetary ions, primarily oxygen ions. The most intense fluxes of tailward streaming heavy ions (ions with mass/charge ratio $M_i/q_i > 3$) were observed in the magnetotail plasma sheet (Rosenbauer *et al.*, 1989; Verigin *et al.*, 1991a). The velocity and intensity of heavy ion fluxes reach their peak values in the vicinity of the magnetic neutral line. The energy of these ions varies from $\sim$ 100 eV up to $>$ 6 keV. Ion dynamics in the Martian tail were discussed by Dubinin *et al.* (1993a). The remarkable feature of the ASPERA observations is that the energy of the different heavy ions in the plasma sheet at $\sim 2.8\ R_M$ is close to the bulk energy of the protons in the solar wind. Figure 4.6 shows $E/q - m/q$ ion matrixes from the measurements in the solar wind and in the plasma sheet.

It is seen that the O^+ ions and the heavier molecular ions (O_2^+ or CO_2^+) have approximately the same energy/charge as the solar wind protons. Another interest-

ing feature is that ions with $m/q = 8$ (O^{++}) have also approximately the same energy/charge. These features indicate, that to a large degree electric fields must be responsible for the acceleration of these ions. This is not really suprising, because both O^+ and molecular ions have large gyroradii ($r_{O+} \sim 3000$ km in a magnetic field of $B_\perp \sim 5$ nT and $W \sim 1$ keV), which are comparable or larger than the width of the plasma sheet. Dubinin *et al.* (1993a) suggested that the ion acceleration is due to the action of magnetic field stresses. The $\mathbf{j} \times \mathbf{B}$ force is the strongest in the center of the tail:

$$(\mathbf{B} \cdot \nabla)\mathbf{B}/4\pi \cong 1/4\pi(B_\perp \, dB_x/dl_\perp) \tag{4.2}$$

where $B_\perp$ and B_x are the transverse and longitudinal components of the magnetic field and $l_\perp$ is the distance between the spacecraft and the current sheet. The B_x component in the tail can be well modeled by $B_x = B_{ox} \tanh(l_\perp/\delta)$, where δ is a characteristic size of the field reversal region ($\delta \sim 2000$ km). Then the magnetic field stresses are proportional to $K/\cosh^2(l_\perp/\delta)$, and the plasma sheet geometry with respect to the spacecraft can be roughly estimated from the IMF orientation.

The peak ion energy variations are similar to the changes in magnetic field stresses. The important feature of the near-Mars tail is that the heavy ions are not magnetized. This means that the $\mathbf{j} \times \mathbf{B}$ force accelerates the electron fluid and the ions are accelerated by the related ambipolar electric field $E_x \sim (\mathbf{j_e} \times \mathbf{B})_x/(n_e ec)$. The energy gained by the ions in the electric field is on the order of:

$$W \sim qLB_\perp B_{xo}/2\pi n_e \delta \, \cosh^2(l_\perp/\delta). \tag{4.3}$$

Thus $W \sim 1 - 2$ keV if $n_e \sim 5$ cm^{-3}, $L/\delta \sim 5 - 10$, $B_{xo} \sim 20$ nT, $B_\perp \sim 5$ nT. This simple model leads to a reasonable agreement with the observations and explains why oxygen and molecular ions have approximately the same energy and the energy of double-ionized oxygen ions is two times higher. Hence a chain of the processes $n_{\rm sw} m_p V_{\rm sw}^2 \rightarrow B^2/8\pi \rightarrow n_{O+} m_{O+} V_{O+}^2$ explains that $W_{\rm sw}(H^+) \sim W_{\rm tail}(O^+)$ if $n_{\rm sw} \sim n_{\rm tail}$. It is also clear that ions with smaller Larmor radii will gain less energy, and that is also in agreement with the observations (Dubinin *et al.*, 1993a).

The measurements made by the TAUS instrument (Rosenbauer *et al.* 1989, Kotova *et al.*, 1997a) have revealed another interesting feature of the ions in the Martian plasma sheet. 2D ion spectra collected during the elliptical orbits showed a supersonic, highly anisotropic distribution function of heavy ions (Rosenbauer *et al.*, 1989). The 3D distribution function of heavy ions, taken while the spacecraft was spinning, has a 'mushroom cap' shape similar to the shape of proton distributions in the terrestrial plasma sheet boundary layer (Kotova *et al.*, 1997a).

Several acceleration mechanisms were invoked for the explanation of such distributions in the Earth's magnetotail (Eastman *et al.*, 1986). A simple field aligned acceleration in an electric field and the adiabatic deformation of the distribution function due to changes in the magnetic field magnitude were examined by Kotova

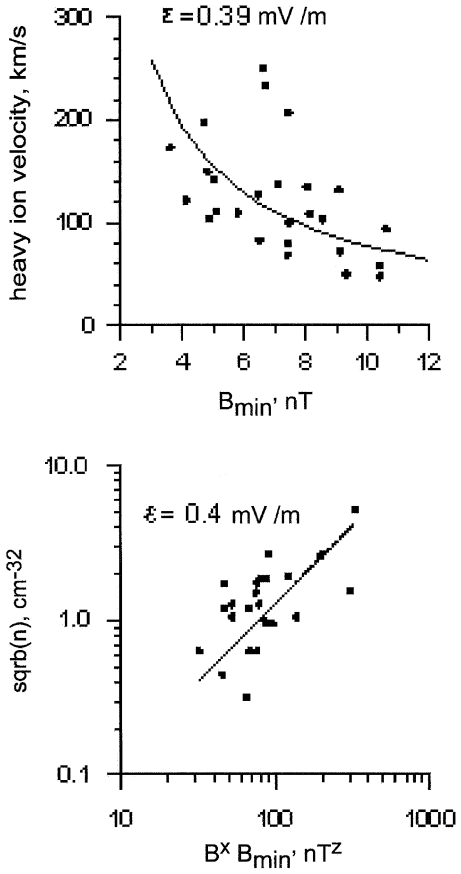

Figure 4.7. Correlations of plasma sheet ion and magnetic field parameters showing evidence for acceleration to occur in the current sheet.

et al. (1997a). It turns out that this model requires the existence of some process that accelerates the ions to velocities of several tens of km s^{-1}. This pre-acceleration may be the result of the direct interaction of ionospheric ions with magnetosheath plasma in the 'polar' regions of the Martian magnetosphere (Verigin *et al.*, 1991a).

Another acceleration mechanism that could account for the 'mushroom cap' shape of the heavy ion spectra, is a classical acceleration in the cross-tail current sheet (Speiser, 1965; Shabanskiy, 1972). The radius of the Martian magnetotail is comparable to the gyroradius of the heavy ions in the plasma sheet. Thus ion kinetic effects in the Martian magnetotail are more important than in the Earth's magnetotail. However, the inverse correlation between the maximum heavy ion velocity (v_{max}) and the minimum magnetic field (B_{min}) in the tail (Figure 4.7) points to the possible existence of a cross-tail electric field in the Martian magnetotail (Kotova *et al.*, 1997a, 2000a). Taking into account that:

$$v_{\max} \approx 2c\varepsilon / B_{\min},$$

where ε is a cross tail electric field in the Martian magnetosphere, c is the velocity of light, the average electric field during the time of the Phobos 2 flight can be estimated as $\varepsilon \approx 0.4$ mV m^{-1}.

Based on the equation (Eastwood, 1972; Hill, 1975):

$$\varepsilon = \frac{B B_{\min}}{\sqrt{4\pi n M_i}}$$

the average electric field can also be estimated from the correlation of $\sqrt{n}$ (n is the heavy ion density) and $B \cdot B_{\min}$ (B is the magnitude of the magnetic field in the tail lobes). The correlation is shown in Figure 4.7 (lower panel), and the average electric field is again $\varepsilon \approx 0.4$ mV m^{-1}.

4.4. Plasma loss

The initial efforts to estimate the loss rate of the Martian ions and neutral gas began about thirty years ago. These first theoretical calculations by Michel (1971), Cloutier *et al.* (1973) and Wallis (1978) indicated a particle loss rate of several grams per second, which we now know is far too low. After the Mars 5 ion measurements at the edge of the Martian magnetotail, Vaisberg (1976) evaluated the planetary heavy ion loss rate through its boundary layer as $\sim 10^{25}$ s^{-1} or ~ 250 g s^{-1}. The absence of a mass-spectrometer aboard this orbiter did not allow the identification of the ion mass and Bezrukikh *et al.* (1978) interpreted their measurements as observations of a proton boundary layer.

The Phobos 2 plasma measurements confirmed the existence of the proton boundary layer. The Phobos 2 instruments had the capability to identify the different masses and that led to the discovery of the magnetotail plasma sheet (Rosenbauer *et al.*, 1989) and to an estimate of the planetary ion loss rate, $\Phi_{\text{esc}} \sim 1$–3×10^{25} s^{-1}, through this structure, (Rosenbauer *et al.*, 1989; Lundin *et al.*, 1989; Lundin and Dubinin, 1992). Similar to the terrestrial magnetotail, the Martian plasma sheet surrounds a narrow current sheet (Figure 4.8). In contrast to the terrestrial case, however, the Martian plasma sheet consist mainly of planetary heavy ions ($m/q > 3$) (Verigin *et al.*, 1991a). Ions with a variety of masses were detected, although oxygen ions appear to be prevalent (Lundin *et al.*, 1989; Dubinin *et al.*, 1993a) with supersonic, highly anisotropic, mushroom cap like distribution functions (see previous section).

The measured values of the ion fluxes in the tail are reliable, but using these values to arrive at an estimate of the total escape flux is associated with significant uncertainties. The uncertainties are mainly associated with the highly variable position of the Martian plasma sheet, which is schematically shown in Figure 4.9, which is based on Phobos 2 TAUS observations (Verigin *et al.*, 1991a). The innermost magnetopause positions are marked in this figure by thin vertical bars.

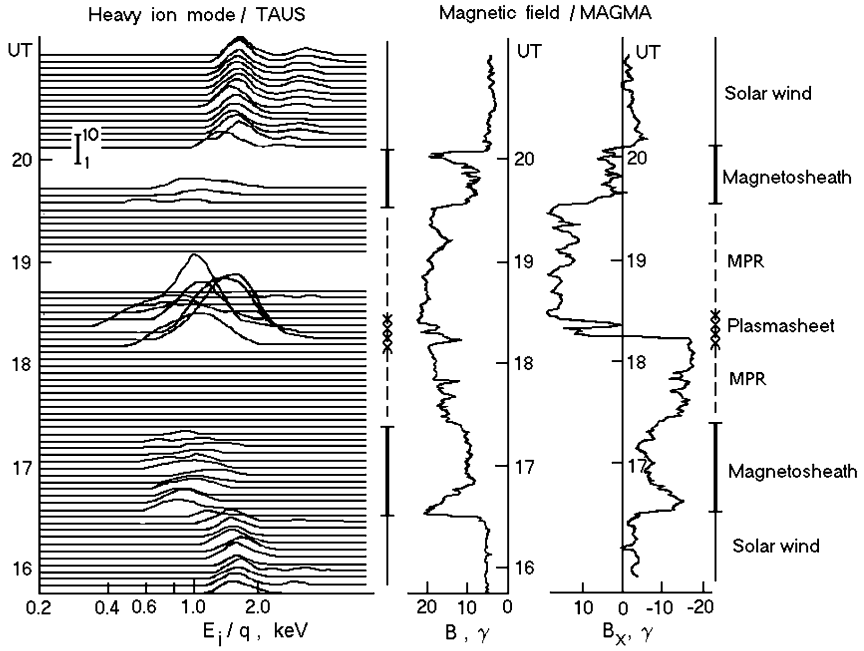

Figure 4.8. Left: Phobos 2/TAUS energy-time spectrogram, which contains heavy ions and protons (admixture) in the Martian magnetotail; Right: total magnetic field and the B_x component (adopted from Verigin *et al.*, 1991a; The authors used the term 'Magnetosphere' for the region labeled MPR). It demonstrates the co-location of a dense plasma population and magnetic field reversal in the Martian magnetotail.

Observations of multiple plasma sheet crossings in some orbits may be caused by plasma sheet motion.

Using information from a variety of observations, Verigin *et al.* (1991a) estimated that the diameter of the Martian magnetotail, D, is approximately 1.5×10^4 km, that the average heavy ion flux in the plasma sheet, F, is about 2.5×10^7 cm^{-2} s^{-1}, and that the plasma sheet thickness, d, is $\sim 0.1D$. The estimate of the plasma sheet thickness was based on the percentage of the time that Phobos 2 spent in the plasma sheet, while crossing the magnetotail (Figure 4.9). The average escape rate of planetary oxygen through the tail is then $\Phi_{esc} \sim F \cdot d \cdot D = 5 \times 10^{24} s^{-1}$. This estimate is in general agreement with other esitmates; the mean suggested escape rate is around $\Phi_{esc} \sim 10^{25}$ s^{-1}, with an uncertainty of about a factor of two.

The ion loss process, through the Martian plasma sheet, is the only one that was observed by in-situ measurements so far, though it is not likely to be the only important planetary oxygen loss process. Another potential escape mechanism is the tailward flow of ionospheric thermal ions (see Section 6.1.2). (Ma *et al.*, 2002; 2004). This tailward flowing plasma may be the source of some of the ions measured in the tail. The hot neutral oxygen densities and escape fluxes at Mars have been calculated, using two different modeling approaches (Kim *et al.*, 1998;

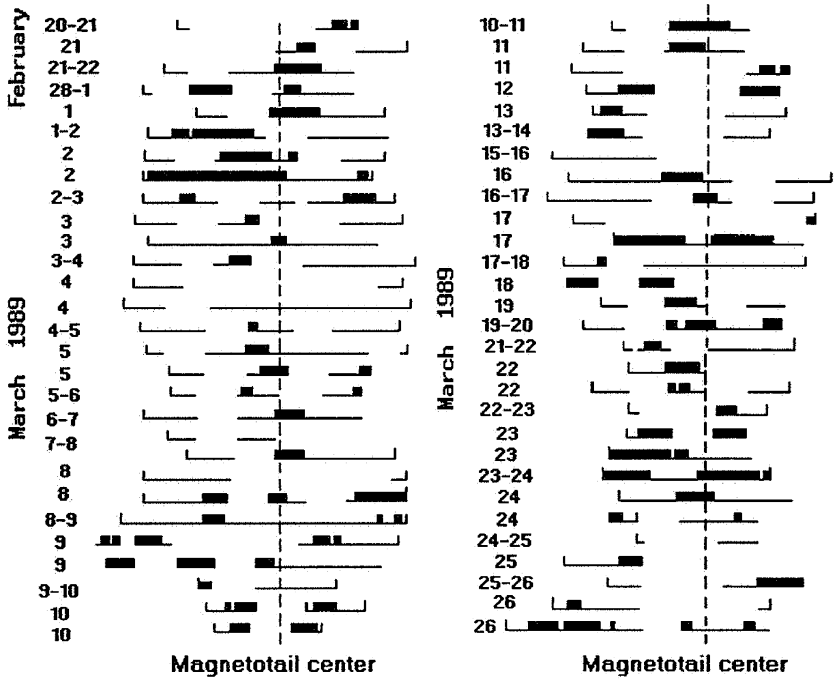

Figure 4.9. Plasma sheet location in the Martian magnetotail as observed during Phobos 2 circular orbits. The dashed line corresponds to the magnetotail center (from Verigin et al., 1991a).

Hodges, 2000). The main source of the hot oxygen atoms was found to be the dissociative recombination of the O_2^+ (see Section 6.3). The estimated escape fluxes vary over the solar cycle; during solar cycle maximum the calculations indicated escape rates, via this mechanism, is in excess of 2×10^{26} s^{-1}. Finally, pick up ion escape and sputtering from the Mars atmosphere also needs to be considered (e.g., Leblanc and Johnson, 2002).

5. The ionosphere

An ionosphere was first detected on Mars by the Mariner 4 spacecraft in 1965 with the radio occultation experiment (Fjeldbo and Eshleman, 1968) and was followed by measurements with Mariners 6 and 7 (Rasool and Stewart, 1971) and Mariner 9 (Kliore *et al.*, 1972). The peak densities were observed to be about 10^5 cm^{-3} and the structure and extent was very different from terrestrial expectations (see Bauer, 1973, for an interesting discussion of these early developments in our knowledge of the ionospheres of Mars and other planets).

The first *in situ* thermospheric and ionospheric measurements ever made for a planet other than Earth were made by instruments onboard the Viking 1 and 2 landers. Neutral composition was measured with mass spectrometers (Nier and

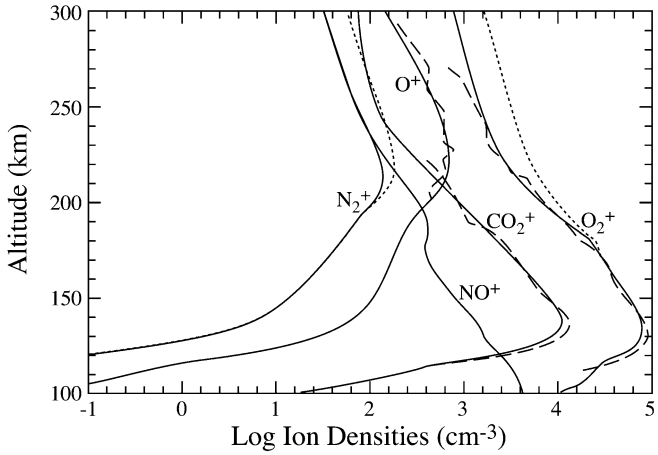

Figure 5.1. Ion densities from a chemical/vertical transport model of the Martian ionosphere for zero outflow upper boundary condition (dashed line) and maximum outflow (solid line). The dotted line are measured profiles from the Viking RPA experiment (Hanson *et al.*, 1977). From Fox (1997).

McElroy, 1977), although not atomic oxygen, and the major ion composition by the retarding potential analyzers (RPA) (Hanson *et al.*, 1977). The measured ion density profiles for CO_2^+, O_2^+ and O^+ are shown in Figure 5.1, illustrating that O_2^+ is indeed the major ion species throughout the Martian dayside ionosphere (c.f., see discussion in Schunk and Nagy, 2000). The observed O^+ density increases with altitude, up to the measurement limit of about 300 km, but never quite becomes the major ion unlike the ionospheres of Earth and Venus. Electron and ion temperature profiles, and photoelectron fluxes, were also measured by the Viking RPA experiments (Hanson *et al.*, 1977; Hanson and Mantas, 1988). These Viking measurements remain our only in situ source of information on 'thermal' ions and electrons at Mars, although the Mars Global Surveyor (MGS) mission has provided important *in situ* measurements of the magnetic field and superthermal electron fluxes (Acuña *et al.*, 1998) and also provided additional radio occultation electron density profiles (Bougher *et al.*, 2001).

Even though *in situ* measurements of the ionosphere are very limited, an extensive set of electron density profiles are available from a number of missions, obtained with the radio occultation technique, over many portions of the solar cycle (Mariners 4, 6, 7, and 9; Viking 1 and 2; the Soviet Mars 4 and 5 missions; MGS). A review of this radio occultation data and a comparison with ionospheric profiles for Venus (mostly from the Pioneer Venus mission) can be found in Zhang *et al.* (1990c) and Kliore (1992). Figure 5.2 shows some of the Viking radio occultation profiles.

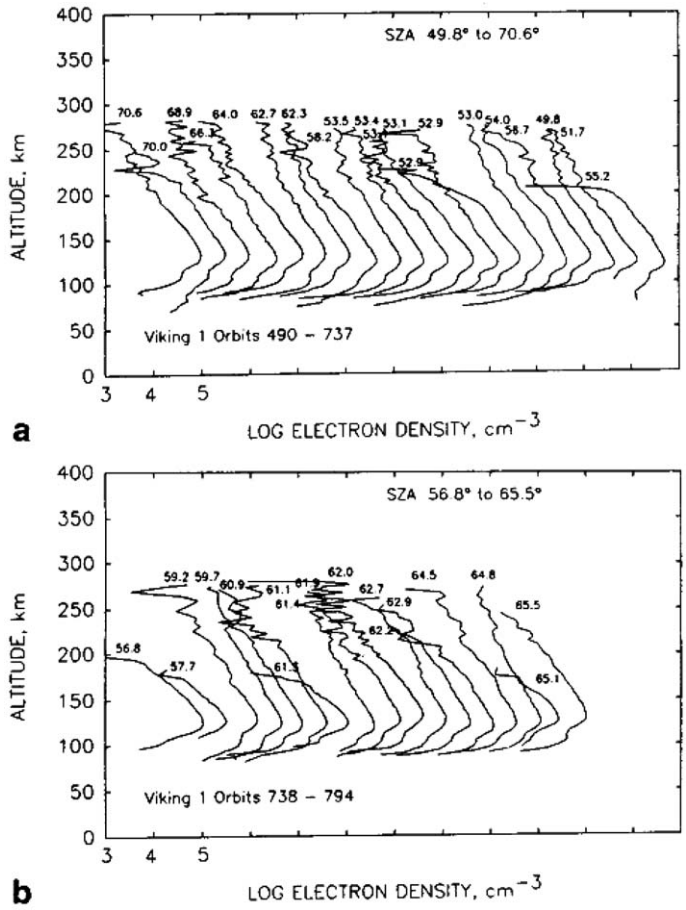

Figure 5.2. Electron density profiles measured on the Martian dayside by the Viking radio occultation experiment on the Viking mission. (a) Orbits 490–737, (b) Orbits 738–794. From Kliore (1992).

5.1. DAYSIDE

The behavior of the ionospheric peak at both Venus and Mars is well-described by Chapman theory, with a peak density at Mars that varies with solar zenith angle, χ, as $n_{\mathrm{emax}} = 2.3 \times 10^5$ cm^{-3}(cos $\chi)^{1/2}$, where all the data has been normalized to an $F10.7$ flux of 150, and where χ is given in degrees (Kliore, 1992). The altitude of the peak is at about 125 km near $\chi = 60°$, and in agreement with Chapman theory this altitude increases with increasing χ. However, the ionospheric peak at 55° was several km higher during the first 71 Mariner 9 orbits than it was at other times. This was attributed to the atmospheric expansion associated with a large dust storm (Stewart and Hanson, 1982).

Other information can also be derived from the radio occultation profiles. As noted by Kliore (1992), with only a few exceptions, all the electron density profiles

exhibit great uniformity in their topside scale heights; the topside scale height is about 35 km. Assuming a photochemical control of the topside ionosphere, the electron density scale height should be twice the neutral CO_2 scale-height ($h_e = 2\ h_n$), which allows the neutral temperature to be remotely monitored (Bauer and Hantsch, 1989; Bauer, 1999). The data is consistent with a Martian thermospheric temperature of $\approx$ 200 K, which also agrees with MGS atmospheric drag measurements (Keating *et al.*, 1998).

The ionopause is a feature almost always observed in the ionosphere of Venus either by the radio occultation technique, or in situ by experiments onboard the Pioneer Venus Orbiter (Kliore, 1992; Brace and Kliore, 1991). The ionopause is marked by sharp decrease in the electron density at the top of the ionosphere. However, no clear ionopause signatures have been observed in the radio occultation profiles at Mars (see Figure 5.2). Interpretation of these observations is considered later.

5.2. NIGHTSIDE

A nightside ionosphere was observed at Mars by the radio occultation experiments on the Mars 4 and 5 spacecraft (Savich *et al.*, 1979) and by the Viking mission (Zhang *et al.*, 1990b). Zhang *et al.* (1990b) concluded that the nightside ionosphere at Mars is generally weaker than that at Venus and the peak altitude is higher. A well-developed ionosphere is present near the terminator. However, its existence deeper on the nightside is more problematic as the following quote from Kliore (1992) notes: '. . .it appears that the nightside ionosphere of Mars more than 10° from the terminator is a rather ephemeral phenomenon. In contrast, on Venus the nightside ionospheric peak is a robust and ubiquitous presence, regardless of solar activity. . .'.

Two mechanisms are known to maintain the nightside ionosphere of Venus: (1) flow of plasma from the dayside topside ionosphere into the nightside, followed by downward flow and recombination, and (2) ionization on the nightside by precipitating electrons (e.g., Brannon *et al.*, 1993; Dobe *et al.*, 1995). The first mechanism is dominant when the dayside ionosphere is unmagnetized, which it ordinarily is, at least during periods of high solar activity. Electron precipitation is able to produce an ionosphere near the peak region, but not at higher altitudes. As a later section will discuss, the dayside ionosphere of Mars is generally magnetized, due to either processes related to the solar wind interaction (Cloutier *et al.*, 1999), or to crustal magnetic fields (Acuña *et al.*, 1998). Therefore it is not surprising, perhaps, that the nightside is not well supplied by plasma from the dayside. However, this is an area that requires both more data and theoretical study.

5.3. IONOSPHERIC ENERGETICS AND AIRGLOW

Dayside electron and ion temperatures generally exceed the neutral temperature in all planetary ionospheres (cf., Schunk and Nagy, 2000) and Mars is not an

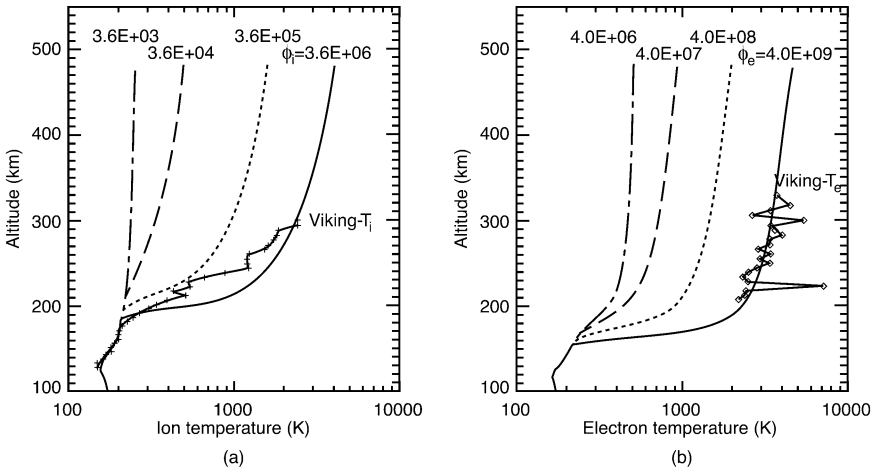

Figure 5.3. Electron and ion temperatures measured by the Viking 1 Retarding Potential Analyzers (Hanson and Mantas, 1988) and some calculated ion and temperature profiles for different topside heat fluxes from (Choi *et al.*, 1998).

exception. The only measured temperature profiles are from the Retarding Potential Analyzer (RPA) experiment on the Viking landers (see Figure 5.3). The electron temperature is about 3000 K for altitude above 200 km and the ion temperature increases from a few hundred K at 200 km up to 3000 K at 300 km. As discussed in Section 6.3, a variety of models (e.g., Rohrbaugh *et al.*, 1979; Choi *et al.*, 1998) have been developed to explain these temperatures and they all require some combination of heat input from the solar wind and/or modification of the thermal conduction coefficients by ionospheric magnetic fields (cf. Nagy and Cravens, 1997).

A key energy input into the thermal ionospheric plasma comes from collisions of this thermal plasma with superthermal electrons. Superthermal electrons have energies significantly in excess of thermal energies, $E > 1$ eV, and have non-Maxwellian energy distributions (cf., Schunk and Nagy, 2000). Two sources contribute to the superthermal electron population, both at Mars and at Venus (e.g, Spenner *et al.*, 1980; Gan *et al.*, 1990): photoelectrons produced by the photoionization of atmospheric neutrals by solar radiation, and solar wind electrons (actually magnetosheath electrons), which make it into the ionosphere along magnetic field lines linking the ionosphere and magnetosheath. Apparently, both superthermal electron sources are present at Mars. The Viking RPA measured superthermal electron fluxes (Mantas and Hanson, 1979), as did the HARP spectrometer on Phobos (Shutte *et al.*, 1989) and the MGS electron reflectometer (Mitchell *et al.*, 2000).

Some superthermal electron flux spectra from MGS are shown in Figure 5.4, as well as a theoretical photoelectron spectrum from Fox and Dalgarno (1979). According to Mitchell *et al.* (2000), spectra in the ionosphere-proper appear to be dominated by the photoelectron contribution, whereas in a boundary layer near the

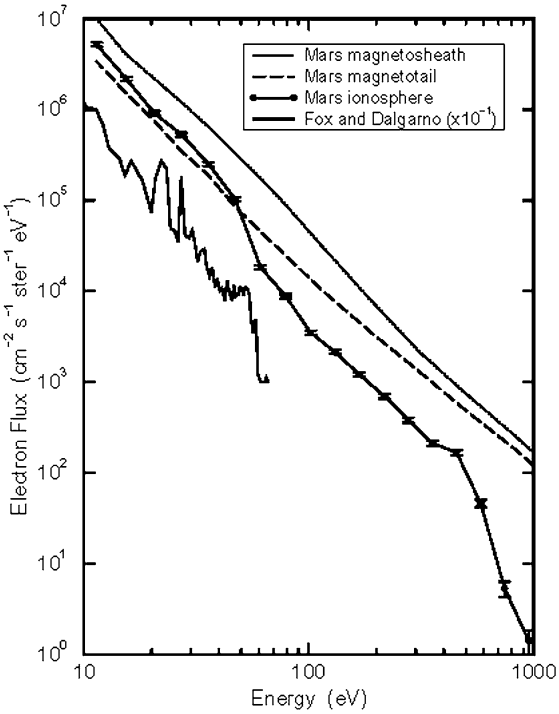

Figure 5.4. Superthermal electron flux versus energy measured by the MGS electron reflectometer in the magnetosheath, in the magnetotail, and in the ionosphere. Also show is a theoretical photoelectron spectrum calculated by Fox and Dalgarno (1979). From Mitchell *et al.* (2000).

top of the ionosphere the spectra take on a more magnetosheath-like appearance. Figure 5.4 from Mitchell *et al.* (2001) also shows this boundary layer which is more apparent for the higher energy electrons. A similar boundary layer was present at Venus and was evident in the measured superthermal electron distributions at that planet (Spenner *et al.*, 1980; Gan *et al.*, 1990).

The ionospheric spectrum for electron energies below about 100 eV is what one would expect from theoretical calculations (see Figure 5.4 again) if the energy resolution is lowered to instrumental values. However, a feature is apparent in the measured ionospheric spectra near 500 eV. This feature is interpreted as being due to Auger electrons produced by the ionization from the K-shell of O atoms, primarily residing in CO_2 (Mitchell *et al.*, 2000). This population of superthermal electrons is associated with the soft X-ray part of the solar spectrum, and it is a useful diagnostic indicating atmospheric origin rather than solar wind origin. Thus it is helpful in mapping out the transition from the ionosphere to the 'solar wind'.

Airglow measurements provide another useful diagnostic of ionization and superthermal electron processes in planetary ionospheres Measurements were made at Mars by the Mariner 6, 7, and 9 missions and also by the Mars 5 mission (cf., Paxton and Anderson, 1991). Prominent CO_2^+ and CO^+ airglow features appear

in the spectrum and are diagnostics of the ionization processes occurring in the ionosphere (see Fox, 1993). The Cameron bands of CO also have a significant contribution from photoelectron excitation. At Venus, measurements of the oxygen 1304 line have been used to deduce energy inputs into the nightside ionosphere by 'auroral' electrons from the magnetotail (Fox and Stewart, 1991), which have also been invoked as one possible source of the nightside ionosphere.

5.4. SOLAR WIND INTERACTION WITH THE IONOSPHERE

For many years it was debated whether or not a significant intrinsic magnetic field existed at Mars, and only recently, with the arrival of MGS, has this issue been settled. MGS is the only spacecraft carrying a magnetometer that has encountered the ionosphere (Acuña *et al.*, 1998). However, we have long realized that magnetic fields induced by the solar wind might be present within the ionosphere (e.g., Cloutier and Daniell, 1979). Prior to MGS, the nature and strength of the Martian magnetic field was estimated indirectly in several ways (cf., Luhmann *et al.*, 1987; Krymskii, 1992), including methods based on observed properties of the ionosphere (Luhmann *et al.*, 1987; Mahajan and Mayr, 1989; Shinagawa and Cravens, 1989, 1992; Zhang *et al.*, 1990b,c; Krymskii, 1992). Overall, these studies suggested that a small, largely horizontal magnetic field (whether induced or intrinsic) of no more than $\approx$ 50 nT was possible. The ionosphere, particularly during solar minimum time periods, was apparently in an 'overpressure' state in which the solar wind dynamic pressure exceeds the maximum ionospheric thermal pressure.

Our understanding of the Martian ionosphere has greatly benefited from the Venus analogy. Extensive studies of the Venus ionosphere, using the large PVO database and numerous theoretical models (cf., Luhmann and Cravens, 1991) demonstrated that an ionosphere of a planet lacking a large intrinsic magnetic field, such as Venus or Mars, should be permeated by large-scale horizontal magnetic fields, extending downward from the 'magnetic barrier' (or MPB), during the overpressure case. On the other hand, the Venus ionosphere was observed to be unmagnetized when the maximum ionospheric pressure significantly exceeded the solar wind dynamic pressure. In this case, a clear ionopause was present and was located at relatively high altitudes. Statistical analyses have shown that the solar wind dynamic pressure exceeds the maximum ionospheric pressure approximately 85% of the time at Mars (Phillips *et al.*, 1984; Zhang *et al.*, 1990c), so that the Martian ionosphere should generally be found to be in the overpressure case, and hence magnetized.

The MGS magnetometer measurements indeed show that the magnetic field in the ionosphere are largely induced (except in regions with significant crustal anomaly fields) (Acuña *et al.*, 1998; Connerney *et al.*, 1999; Cloutier *et al.*, 1999). This is illustrated in Figure 5.5, which shows the measured magnetic field strength and orientation in the ionosphere. Note that the magnetic field is mainly horizontal

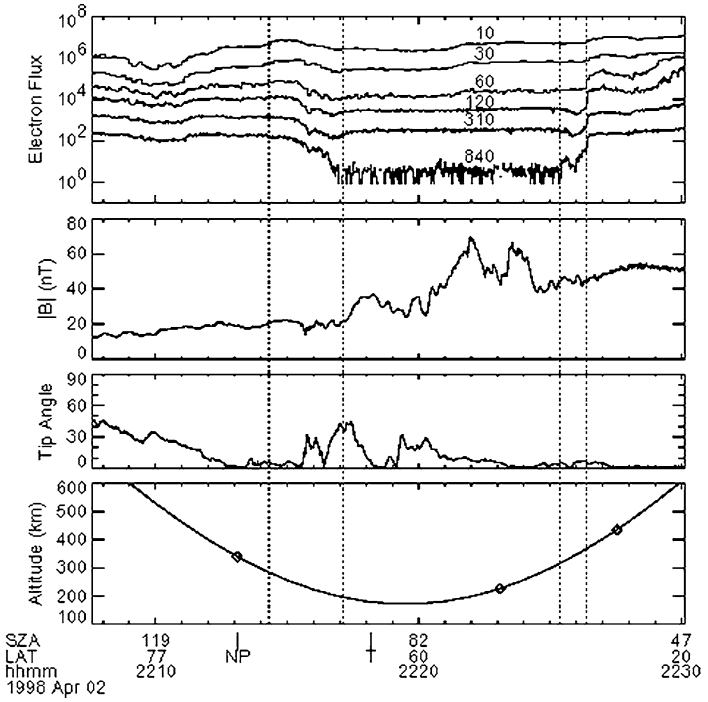

Figure 5.5. Time series of the superthermal electron flux for several energy channels from the MGS electron reflectometer for a April 2, 1998 pass. Units are cm^{-2} s^{-1} $ster^{-1}$ eV^{-1}. Also shown is the magnetic field strength (in nT) and the tip angle of the field (angle from the horizontal). From Mitchell *et al.* (2000).

with a strength of roughly 50 nT or less (Mitchell *et al.*, 2000), as expected for fields induced by the solar wind interaction (Shingawa and Cravens, 1989; Krymskii, 1992; Cloutier *et al.*, 1999). A boundary layer is evident in the superthermal electron fluxes, as discussed above, yet there is no obvious signature of this layer in the magnetic field. Unfortunately, the thermal electron density was not measured *in situ*, so that the overall plasma density structure in this boundary layer is not known. Cloutier *et al.* (1999) notes that a magnetic field rotation occurs near this boundary layer and is analogous to similar field rotation observed near the Venus ionopause.

The observed topside scale height in the Martian ionosphere is only about 35 km, as discussed earlier, and appears to be 'photochemical' rather than the larger scale height that a free ('diffusive') vertical transport would yield. Plasma scale heights from many radio occultation profiles obtained during the Mariner 9 and Viking missions were analyzed and confirm this statement (Izakov and Roste, 1996; Breus *et al.*, 1998; Ness *et al.*, 2000). Horizontal magnetic fields, such as the ones that have now been observed in the ionosphere, will indeed inhibit vertical transport (Shinagawa and Cravens, 1989; Krymskii, 1992).

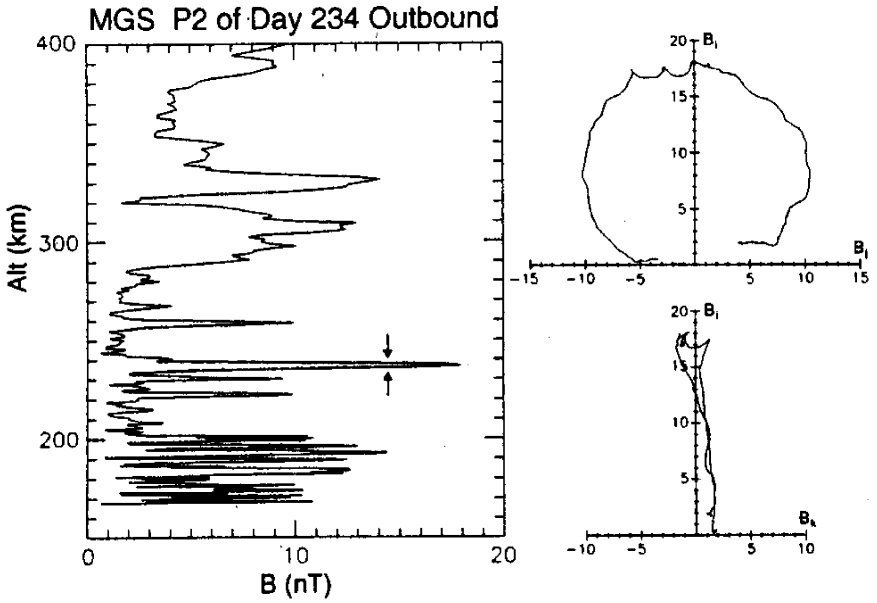

Figure 5.6. On the left: magnetic field strength versus altitude as measured by the MGS magnetometer experiment for Day 234 of 1998. On the right: hodogram of a magnetic flux rope, in principal axis coordinates. From Cloutier *et al.* (1999).

On a few occasions, when the Martian ionosphere appeared to have relatively low magnetic field strength, perhaps associated with low solar wind dynamic pressure conditions, MGS observed spatially narrow features with strong localized field surrounded by low background field (Cloutier *et al.*, 1999). One example of such conditions is given in Figure 5.6 for day 234 of 1998. Cloutier *et al.* (1999) produced a hodogram for one of the magnetic structures and demonstrated that it was a 'force-free' magnetic flux rope. Magnetic flux ropes with similar helical structures were commonly observed by the PVO magnetometer in 'unmagnetized' ionospheres of Venus (Elphic *et al.*, 1980; Luhmann and Cravens, 1991). The formation of magnetic flux ropes at either Venus or Mars is not really understood yet, although much work has been carried out on this topic (cf., Cravens *et al.*, 1997). Some promising suggestions have been made by Krymskii *et al.* (2000) for Venus, in which ropes form, not at the ionopause as some previous theories had suggested, but due to instabilities in the magnetic 'belt', which has been observed by the PVO magnetometer at low altitudes in the ionosphere. Perhaps similar ideas can be applied to flux rope formation in the Martian ionosphere(see Vignes *et al.*, 2002).

5.5. ROLE OF CRUSTAL ANOMALIES

A key difference in the characteristics and dynamics of the ionospheres of the two nonmagnetic planets, Venus and Mars, does exist due to the crustal magnetic anom-

alies that were discovered by the MGS magnetometer at Mars (Acuña *et al.*, 1998, 1999; Connerney *et al.*, 1999; Ness *et al.*, 1999). The local, but fairly widespread crustal magnetic field anomalies, observed by MGS, may create an effective large-scale magnetic field structure in the southern hemisphere (Ma *et al.*, 2002). The major fraction of the planetary magnetic field flux is concentrated near the surface of Mars. The rest of the flux 'escapes' from the planet and, in the context of the solar wind Mars interaction process, can act as an effective dipole. The anomalies can also create regions with effective horizontal (as well as radial) magnetic fields at ionospheric altitudes, where the radio occultation measurements were made (Krymskii *et al.*, 2002).

'Mini-magnetospheres' are formed in regions of strong crustal field (Mitchell *et al.*, 2001) that should strongly affect ionospheric processes, partly by acting as a more effective obstacle to the solar wind, holding it off at altitudes exceeding 400 km (Brain *et al.*, 2003; Ma *et al.*, 2002). For example, the outermost lines of crustal magnetic field should be able to re-connect with IMF lines draped around the mini-magnetospheres, so the region outside the 'closed' magnetosphere is covered with a boundary layer of 'opened' field lines, which connect the Martian surface and the solar wind. Brain *et al.* (2003) have recently studied the reconnection of Martian magnetic fields to the solar wind and found that the reconnection regions cover about 7% of the Martian surface. Outside of the mini-magnetospheres the Martian ionosphere should be qualitatively similar to the ionosphere at Venus as discussed earlier. On the other hand, numerous cusp-like regions should also form above the crustal anomalies through which charged particles can penetrate into the ionosphere and neutral atmosphere resulting in heating and ionization (Brain *et al.*, 2003; Ness *et al.*, 2000).

The crustal anomalies should also affect the nightside ionosphere. Neither day-to-night flow nor electron impact ionization caused by precipitating energetic electrons can repopulate the nightside ionosphere within an intense crustal magnetic field region (mini-magnetosphere) except in the 'cusp' regions. This means that the ionospheric plasma can be denser outside a mini-magnetosphere region than inside it, because day-to-night plasma transport and/or impact ionization caused by energetic electrons precipitating from the magnetotail can keep it populated. Mitchell *et al.*, (2001) have detected plasma voids at around 400 km on the nightside, which correspond to regions of crustal magnetization.

6. Theory and Modeling

In the preceding sections the observed properties of the dayside bowshock, magnetosheath and ionosphere were summarized. Here in this section the theoretical model calculations, associated with these regions are described. The primary challenge of the model calculations is, of course, to explain the details of the interactions, subject to the constraints imposed by the observations (see Introduction).

First we describe three current global models of the solar wind interaction with Mars. This is followed by an outline of the model of hot atom production around Mars and a review of various ionospheric models.

6.1. GLOBAL MODELS OF THE SOLAR WIND/MARS INTERACTION

Before beginning a discussion of the modeling tools used to simulate Mars and some of the results that have been published concerning the solar wind interaction with Mars, it is instructive to consider why one would resort to such simulations. There are a variety of answers to this question. One of them is that the visualization of the full system, provides leading questions, occasionally provides answers, and often provides insight. Also the various models are based on a variety of different assumptions/simplifications and thus can lead to a better understanding of the relative importance of the different mechanisms, controlling the interaction processes. The theoretical models of the solar wind interaction with Mars can be placed in two general categories: fluid and kinetic approaches. The hydrodynamic model calculations of Spreiter and colleagues starting back in the 1960's (Spreiter and Briggs, 1962; Spreiter and Stahara, 1980) provided groundbreaking new insights into the basic, large scale interaction processes between the supersonic solar wind and solar system objects. These hydrodynamic results are still used in some applications (e.g. Zhang *et al.*, 1993a), but to a large degree have been superseded by more sophisticated models during the last decade⋆. The three current models in use are:

(i) The semi-kinetic model developed by Brecht;
(ii) The multi-species, single fluid MHD model developed by Nagy and colleagues
(iii) The two-fluid MHD model developed by Sauer and colleagues.

The challenge for the numerical models is to reproduce, mathematically, the observations described earlier – the boundaries and regions and their characteristics now heuristically understood from the data. In particular, the MPB and MPR, the ionospheric characteristics, the shock, and the unusually large upstream wave activity should be identifiable in the model results. Of course, not all model approaches encompass the entire interaction problem. Therefore the reader will find that one model will be better at explaining the characteristics of the shock, while an other may excel in describing the cause and effect of the MPR and MPB, or the workings of the ionosphere. Indeed, a rather considerable problem in itself is to understand the limitations of the individual model approaches, and their domain of applicability, which typically are not heralded by the model architects ('If the best tool in one's toolbox is a hammer, solutions tend to appear as nails.').

⋆ The results from a new 3D, single fluid, non-ideal MHD model have just been published (Harnett and Wingler, 2003).

6.1.1. *The Semi-Kinetic (Hybrid) Model*

The kinetic simulations most often used in space research are the so-called hybrid particle simulations, where the ions are treated as individual particles, whereas the electron are considered as a massless neutralizing fluid (cf., Brecht *et al.*, 1993). The hybrid model allows easy inclusion of multiple ion species, because they are simply particles following the basic Lorentz force laws and are automatically kinetic in their behavior. This approach to treating the ions permits direct simulation of ion gryo-motion effects and drift motion due to electric and magnetic fields as well as density gradients. The electron momentum equation, given below as Equation (6.5) is equivalent to Ohm's Law, containing the Hall, $\mathbf{J}_e \times \mathbf{B}$ and ∇p_e terms. The Hall term breaks the symmetry of the equations and permits, among other things, filamentation of the plasma, and the propagation of whistler mode waves. The pressure and resisitive terms in the Ohm's law also contribute to the electric field.

The rich suite of electromagnetic modes resulting from the model equations, as well as, the inclusion ion gyromotions, means that the physics of collisionless shock formation are directly simulated in this model. This includes parallel waves and the subsequent acceleration of the ions in the shock structure. One should note that the ion pressure is not needed in any of the equations. This is a fluid dynamic concept and is not valid within the kinetic approach. However, the particle distributions and moments can be calculated in order to investigate the shape of the distribution functions and the ion pressure tensor. Indeed it is the anisotropic pressure, created by the reflected ions at the shock, that leads to the electromagnetic modes within the shock. These wave modes result in two effects. First, they lead to a very structured shock surface. Second, they carry away energy in the form of whistler, Alfvén-Ion-Cyclotron (AIC) waves. This is what leads to shock overshoots seen at the various planets (Russell *et al.*, 1982; Mellot and Livesey, 1987).

The charge neutrality assumption and the neglect of the transverse part of the displacement current (called the Darwin approximation) truncate Maxwell's equations. The charge neutrality removes high speed plasma oscillations, while the charge separation and Darwin approximations remove the light waves. This allows the use of larger cell sizes and larger time steps making the numerical solution of this model easier. Given the above described formulation and approximations the controlling equations are as follows:

$$\nabla \times \mathbf{B} = \mathbf{J}, \tag{6.1}$$

$$\nabla \times \mathbf{E} = -\frac{\partial \mathbf{B}}{\partial t}, \tag{6.2}$$

$$m_i \frac{\partial \mathbf{v}_i}{\partial t} = q_i \{\mathbf{E} + \mathbf{v}_i \times \mathbf{B}\} - q_i \eta \mathbf{J}, \tag{6.3}$$

$$\frac{\partial \mathbf{x}_i}{\partial t} = \mathbf{v}_i, \tag{6.4}$$

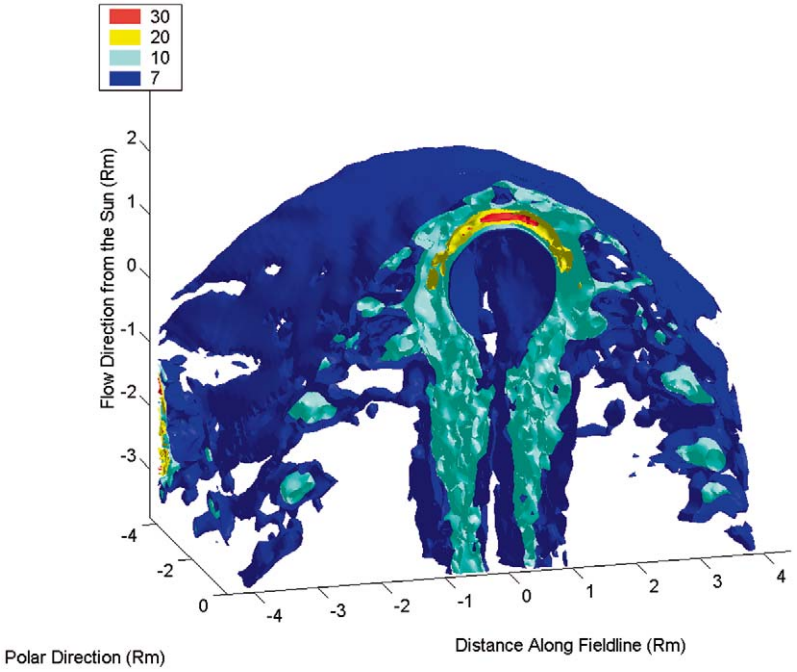

Figure 6.1. A 3-D surface plot of the Martian bow shock cut through the ecliptic plane. The magnetic barrier is symmetric, the shock is symmetric and the two lobes of the magnetotail of Mars are clearly seen. One, can see evidence of the wave structure of the region below the shock. In this perspective the solar wind come from the top of the picture and the IMF is in the plane of the cut through the volume.

$$-en_e\mathbf{E} + \mathbf{J}_e \times \mathbf{B} - \nabla p_e + en_e\eta\mathbf{J} = 0, \tag{6.5}$$

$$\sum_i n_i = n_e, \tag{6.6}$$

where the charge neutrality given in (6.6) holds for scale lengths greater than the Debye length, η is the plasma resistivity, and the subscripts e and i denote electron and ion parameters, respectively. These equations are solved with a predictor-corrector method, first published by Harned (1982). Full details of this hybrid formulation, including the equations solved can be found in Brecht and Thomas (1988).

This approach to global modeling is often considered to be the most complete approach. However, it has certain limitations, the main practical one being that it is very computer intensive. The time steps must be small enough to resolve the fastest of the allowable electromagnetic modes, the whistler wave. The spatial cell sizes must be small enough to resolve the ion gyroradii and the Hall effects. In the case of Mars, this means cells of the order of 100's of kilometers.

This code has been applied to simulations of the solar wind interaction with Mars. In particular, the magnetic topology of Mars in full 3-D was investigated

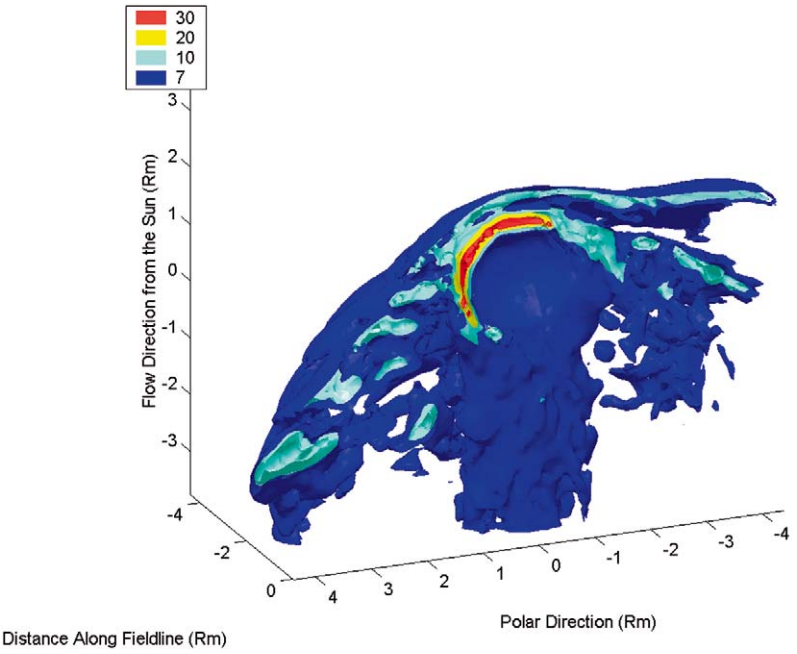

Figure 6.2. A 3-D surface plot of the Martian bow shock cut through the polar regions. The magnetic barrier is highly asymmetric, the shock is also asymmetric and one can see considerable difference between the two polar regions. In this perspective the solar wind comes from the top of the plot. The convection electric field is in the plane of the cut through the volume and points in the positive direction.

in order to see the effects of the kinetic interaction on the shock (Figure 6.1 and Figure 6.2). It was found that the bow shock did not thermalize the solar wind plasma as occurs on other planets (Brecht *et al.*, 1993) and that the shock was asymmetric in the polar directions with the normal solar wind IMF configuration (Brecht and Ferrante, 1991; Brecht *et al.*, 1993; Brecht, 1997a).

It was also suggested by the hybrid simulations that the solar wind deposits a significant amount of energy into the planets ionosphere and atmosphere (Brecht, 1997b). Finally, Phobos 2 orbits have been flown through the hybrid simulations as a way of comparing the results of the simulations with the data obtained by this spacecraft. The results were encouraging and agreed well with the data (Brecht *et al.*, 1993). More recently, as the research has evolved, it has been found that adding an ionosphere and exosphere to the simulations leads to the appearance of flux filaments (Figure 6.3). They only occur in the North Pole of the planet where the IMF is in the ecliptic plane, as is typical for the IMF. Indeed the preponderance of the flux seems to be transported preferentially over the North Pole. Currently the model has started to be used to investigate the role of the crustal magnetic fields (Acuña *et al.*, 1998, 1999) on the shape of the shock, and scavenging of the Martian ionosphere, caused by the solar wind interaction with Mars.

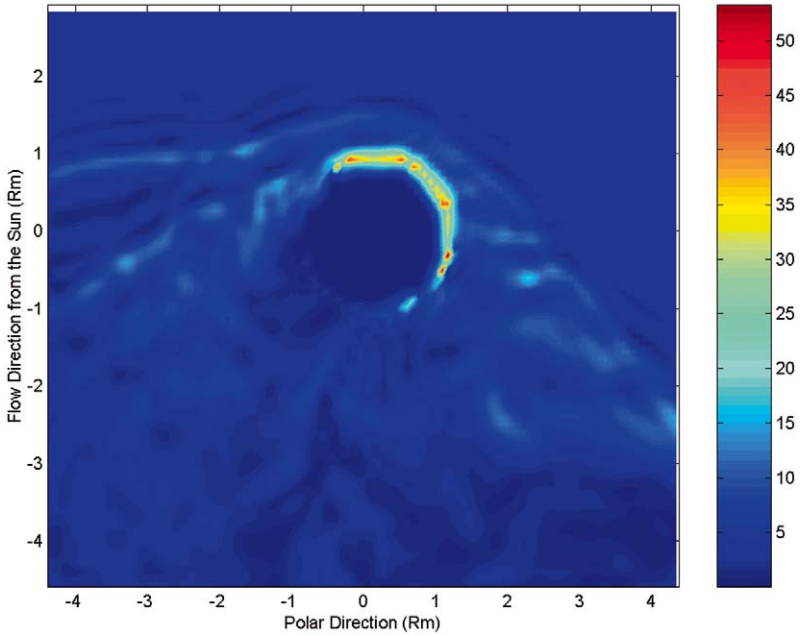

Figure 6.3. A 2-D slice through the simulations shown in Figure 6.1 and Figure 6.2. This plane contains the solar wind flow and the convection electric fields. The magnetic barrier is highly asymmetric and strongest over the North pole of the planet. One, can also see the tendency of the simulation to develop strong regions of magnetic field within the barrier region, suggesting that flux ropes may well be more favorably formed in the North pole region as well.

6.1.2. *The Multi-Species, Single Fluid MHD Model*

It has been argued that the use of semi-kinetic models is especially appropriate for Mars, where the ion gyroradius is of the same order as the planetary radius, which is true mainly outside the bowshock. However, it is important to note that the ideal MHD equations have been found to be successful even in such situations. The possible reason for this maybe the presence of significant wave activity and turbulence, which lead to a wide variety of wave particle interactions, which in turn act as pseudo-collisions. The wave activity and turbulence were observed by the Phobos-2 wave instrument (Grard *et al.*, 1989), and the MGS magnetometer (e.g., Acuña *et al.*, 1998; Cloutier *et al.*, 1999), and was predicted by the semi-kinetic code described above.

Further, there are many questions of interest that are truly fluid in their behavior. This is especially true when one is addressing the influence of the solar wind interaction on the ionosphere and atmosphere. In these regions even the classical collision frequencies are high and the velocities small, resulting in effective gyroradii which are small compared to the scale sizes of the system.

The MHD calculations described next (Ma et al., 2002; 2004) solve the coupled set of equations consisting of a number of continuity equations, one momentum

equation, one energy equation, and one magnetic field equation. The justification for using a single momentum equation is that often the fluids of interest are closely coupled where they exist together (however, see Section 6.1.3). The actual equations (assuming three species) are:

$$\frac{\partial \mathbf{W}}{\partial t} + \{\nabla \cdot \mathbf{F}\}^T = \mathbf{Q}, \tag{6.7}$$

where the total energy density is defined as

$$\varepsilon = \frac{1}{2}\{\rho_1 + \rho_2 + \rho_3\}u^2 + \frac{1}{\gamma - 1}p + \frac{B^2}{2}, \tag{6.8}$$

the state vector, flux tensor, and source vector in Equation (6.7) are

$$\mathbf{W} = \begin{pmatrix} \rho_1 \\ \rho_2 \\ \{\rho_1 + \rho_2 + \rho_3\}\mathbf{u} \\ \mathbf{B} \\ \varepsilon \end{pmatrix}, \tag{6.9}$$

$$\mathbf{F} = \begin{pmatrix} \rho_1\mathbf{u} \\ \rho_2\mathbf{u} \\ \rho_3\mathbf{u} \\ \{\rho_1 + \rho_2 + \rho_3\}\mathbf{uu} + \left\{\frac{B^2}{2}\right\}\mathbf{I} - \mathbf{BB} \\ \mathbf{uB} - \mathbf{Bu} \\ \mathbf{u}\{\varepsilon + p + \frac{1}{2}\} - \{\mathbf{B} \cdot \mathbf{u}\}\mathbf{B} \end{pmatrix}, \tag{6.10}$$

$$\mathbf{Q} = \begin{pmatrix} 0 \\ S_2 - L_2 \\ S_3 - L_3 \\ \{\rho_1 + \rho_2 + \rho_3\}\mathbf{g} - \{\rho_1 + \rho_2 + \rho_3\}\nu\mathbf{u} - \mathbf{u}L_2 - \mathbf{u}L_3 \\ 0 \\ Q_6 \end{pmatrix}, \tag{6.11}$$

where the source term of the energy equation, Q_6, is

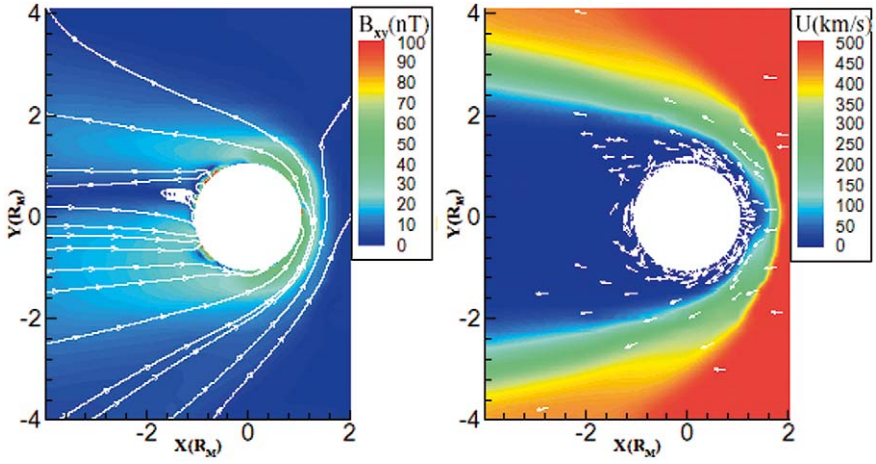

Figure 6.4. The component of the calculated magnetic field (left) and velocity magnitudes (right) in the xy plane. The color plots show the magnitudes; the white lines marked with arrows indicate the vector direction of the magnetic field and the arrows the direction (not the magnitude) of the velocity (from Ma et al., 2002).

$$Q_6 = \{\rho_1 + \rho_2 + \rho_3\}\mathbf{u}\cdot\mathbf{g} - \frac{1}{2}u^2\{L_2 + L_3\} - \{\rho_1 + \rho_2 + \rho_3\}\nu u^2 - \\ - \frac{1}{\gamma - 1}\frac{L_2 p}{\{32\rho_1 + \rho_2 + 2\rho_3\}} - \frac{1}{\gamma - 1}\frac{L_2 p}{\{16\rho_1 + 0.5\rho_2 + \rho_3\}} + \\ + \frac{1}{\gamma - 1}S_2\frac{k}{m_2}T_o + \frac{1}{\gamma - 1}S_3\frac{k}{m_3}T_o \qquad (6.12)$$

and where ρ_1, ρ_2 and ρ_3 are the H^+, O_2^+ and O^+ mass densities, respectively, S_2, S_3 and L_2, L_3 are the O_2^+, and O^+ mass source and loss rates, respectively, p is the total thermal pressure of the plasma, $\mathbf{u}$ is the velocity of the plasma, ν is the ion neutral collision frequency (taken to be $4 \times 10^{-10}\{(O) + (CO2)\}$ s^{-1}, T_o is the temperature of the newly produced ions and the other symbols have their usual definition.

The computational domain defined by $-24\ R_M \leq x \leq 8\ R_M$, $-16\ R_M \leq y$, $z \leq 16\ R_M$, where $R_M = 3396$ km is the radius of Mars, was used in these calculations and the inner boundary was taken to be 140/100 km above the Martian surface. The numerical approach used in solving the equations is described in Powell *et al.* (1999) and the boundary conditions adopted can be found in Ma *et al.* (2002; 2004). A 60-order harmonic expansion for the crustal magnetic field (Arkadi-Hamed, 2001), which reproduces the observed fields very well, was used.

In the calculations published by Ma et al. (2002) the location of the largest crustal field (180 longitude) was pointing sunward, and the solar wind flow direction was parallel with the equator of the planet. Figure 6.4 shows the calculated magnetic field and velocity components in the equatorial plane, while Figure 6.5

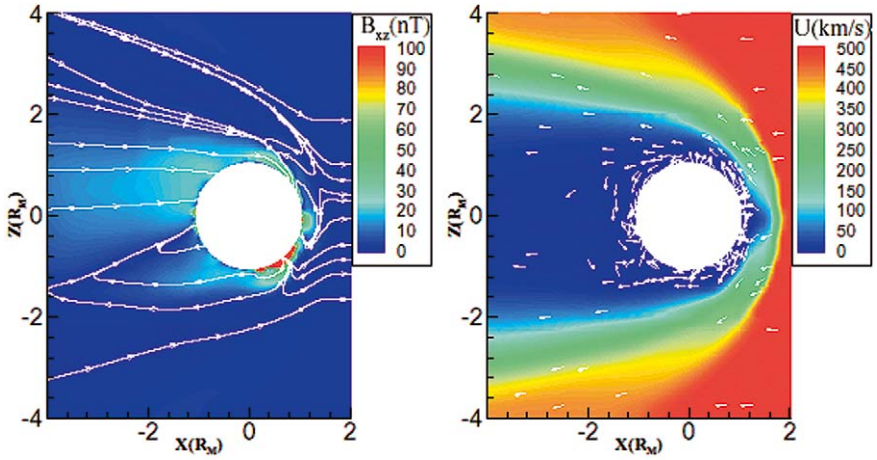

Figure 6.5. The same as Figure 6.4, but in xz plane (from Ma et al., 2002).

shows the field and velocity in the noon-midnight meridian plane. The color plots show the magnitude of the field and velocity components; the white lines show the field directions and the white arrows the direction (not the magnitude) of the velocities. The draping of the IMF is clearly visible in the equatorial plane as indicated in Figure 6.4 and the small 'bends and kinks' are the result of the crustal fields. There also appears to be a flux rope like feature; flux ropes have been observed by the MGS magnetometer (Vignes *et al.*, 2002). The general trend of the plasma flow is upward and toward the terminator on the dayside and either downward into the ionosphere (helping to maintain the nightside ionosphere) or down the tail (and escaping from the planet) on the nightside. Figure 6.5 shows the presence of closed field lines (mini 'magnetocylinders'), the result of the 'merging' of the crustal and IMF fields. The presence of such mini-magnetospheres have been inferred by the electron reflectometer carried aboard the Mars Global Surveyor (MGS) spacecraft (Mitchell *et al.*, 2001). Figure 6.6 shows the plot of the dayside location of the calculated 9 nT values (three times the assumed IMF field) as the proxy for the bowshock position. In order to compare these results with the observed bowshock locations (which have been presented assuming symmetry about the X-axis) the calculated curves are shown both in the $X - Y$ and $X - Z$ planes. The agreement between the calculations and observations (Vignes *et al.*, 2000) are good, especially considering the fact that there is a scatter, of the order of one Mars radius, in the observed locations.

Given the strong spatial variations in the crustal field the ionopause locations are not expected to be spherically symmetric around the planet. MGS results have demonstrated the positive correlation between the ionopause height and the strength of the magnetic field (Mitchell *et al.*, 2002). 'Ionopause' in this case is defined by the change in character of the superthermal electron spectrum (the 'photoelectron boundary'), and does not necessarily coincide with a sharp change

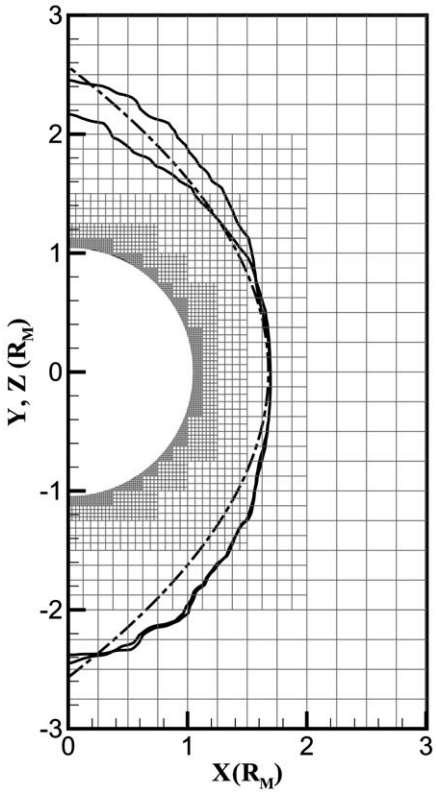

Figure 6.6. Plot showing where the magnetic value is equal to 9 nT in equatorial plane (blue line), and in meridian plane (red line); This value of magnetic field is used as a proxy for the location of the bow shock. Also shown is the mean value of the observed bowshock location (green line) from Vignes *et al.*, 2000 (from Ma et al., 2002).

in the thermal electron density, as was originally meant by this term for the Venus ionosphere.

The model calculations of Ma *et al.*, (2002) also provide some indication of such a situation. They determined the locations where the pressure balance between the kinetic pressure of the ionospheric ions equals the sum of the magnetic pressure and the total (kinetic plus dynamic) solar wind proton pressure. The position of this pressure balance is a reasonable indicator of the ionopause location. They compared the locations of these pressure balances, which they calculated for the the non-magnetic case with those calculated in the presence of crustal fields. They found that the presence of the crustal magnetic fields does raise the 'ionopause' altitude; the largest outward movement is near the strongest field location and corresponds to an altitude increase of about 370 km.

Ma *et al.*, (2002; 2004) also calculated the trans-terminator and tailward escape fluxes. They found that these fluxes decrease in the presence of the crustal field and that they change with solar cycle, as expected. Their calculations indicate

that these ionospheric fluxes make up a significant fraction of the total escape flux estimated from the Phobos-2 measurements (Lundin *et al.*, 1989; Rosenbauer *et al.*, 1989). The calculated trans-terminator flux is also consistent with the 'upper-limit' estimates of Fox (1997). Ma *et al.* (2004) have modified their earlier model and are now using a spherical grid stucture, which leads to much better radial resolution. The ionospheric resolution that they have obtained is about 10 km, considerably less than the plasma scale height, and thus leading to meaningful results in this region.

6.1.3. *Two-Fluid, Multi-Species MHD*

The major initial motivation for constructing an MHD model with separate ion momentum equations was observations made in the different plasma environments of comets, Venus and Mars. In addition, the active experiments in space in which barium and lithium were released into the solar wind creating artificial comets (Bryant *et al.*, 1985) provided further stimulus. These observations indicated that the solar wind protons and the heavy ions of the obstacle have their own separate dynamics. The first of such a model was a one dimensional MHD model, with two momentum equations (Sauer *et al.*, 1990; Baumgärtel and Sauer, 1992). While the classical one-fluid MHD models failed to reproduce a number of important aspects of the observed signatures of the proton flow, the main features of the interaction can be described by an MHD model in which protons and heavy ions develop their own interconnected dynamics (Sauer *et al.*, 1990).

The continuity and momentum equations used in the model are given below for the protons (the same equations are also used for the heavy ions; thus interchanging the subscripts p and h, lead to the heavy ion equations):

$$\frac{\partial n_p}{\partial t} + \nabla \cdot \{n_p \mathbf{u}_p\} = 0, \tag{6.13}$$

$$\frac{\partial \{n_p \mathbf{v}_p\}}{\partial t} + \nabla \cdot \{n_p \mathbf{v}_p \mathbf{v}_p\} = \frac{1}{m_p} \frac{n_p}{n_e} \left\{ e n_h [\mathbf{v}_p - \mathbf{v}_h] \times \mathbf{B} - \nabla \left[\left(p_e + \frac{B^2}{2\mu_o} \right) \mathbf{I} - \frac{\mathbf{BB}}{\mu_o} \right] \right\}, \tag{6.14}$$

$$\frac{\partial p_e}{\partial t} + \nabla \cdot \{\mathbf{v}_e p_e\} + \{\gamma - 1\} p_e \{\nabla \cdot \mathbf{v}_e\} = 0, \tag{6.15}$$

$$\frac{\partial \mathbf{B}}{\partial t} - \nabla \times \left\{ \frac{1}{n_e} \left[n_p \mathbf{v}_p + n_h \mathbf{v}_h - \frac{1}{\mu_o} \nabla \times \mathbf{B} \right] \times \mathbf{B} \right\} = 0, \tag{6.16}$$

where n_p, n_h and n_e are the proton, heavy ion and electron number densities, n_c is the charge density, $\mathbf{B}$ is the magnetic field, p_e is the electron pressure and $\mathbf{v}$ denotes the relevant velocities.

At first a relatively simple model for analyzing the interaction of a flowing plasma with a heavy ion source (which is representative of a cometary or planetary atmosphere), was developed by Baumgärtel and Sauer (1992). This stationary 1D model shows that a sub-sonic/Alfvénic flow penetrating the 'ionospheric'

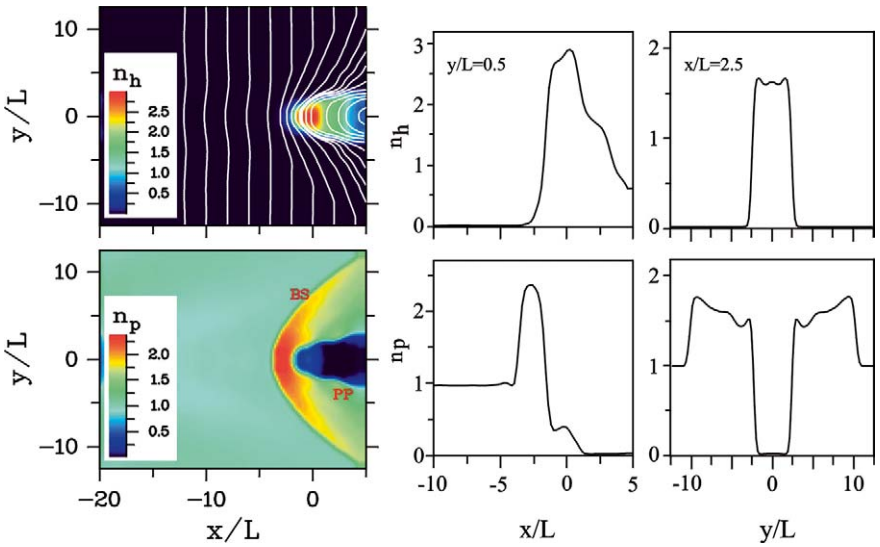

Figure 6.7. Results of 2D bi-ion fluid simulations of solar wind interaction with a heavy ion source. The momentum coupling is provided solely by the ambipolar electric field (the magnetic field is not included in the dynamics calculation). The upper three panels show (from left to right) the spatial distribution of the heavy ion density (n_h), and cuts along $x(y/L = 0.5)$ and $y(x/L = 2.5)$. In the lower three panels the same is shown for the proton density (n_p). A remarkable feature is the formation of a boundary where protons are replaced by heavy ions (MPB). The magnetic field lines shown as white lines in the upper color plot show the enhanced draping at this boundary (adapted from Sauer and Dubinin, 2003).

plasma behaves like a gas in a Laval nozzle. On the front side of the heavy-ion cloud the protons are accelerated and then decelerated after reaching the center of the 'obstacle'. At a 'critical heavy-ion density', which is less than the density of the incoming protons the flow becomes choked. This phenomenon arises from the proton flow becoming sonic before reaching the center of the heavy ion cloud. In reality of course the flow is not one-dimensional and in two dimensions one is lead to expect the formation of a proton flow boundary.

A similar magnetic field-free model, in which a source of heavy ions is included, shows that the self-consistent interaction between the proton flow and the heavy ions leads to the formation of a sharp boundary between both ion fluids. Figure 6.7 shows the spatial dependence of both the proton and heavy-ion densities as color plots (left), together with cuts through the simulation box, representing crossings along the flank ($y/L = 0.5$) and through the tail ($x/L = 2.5$) of the interaction region. The coordinates x and y are normalized by the characteristic scale length, L, of the source function. Since the magnetic field is not included in the dynamics calculation, the coupling between the protons and heavy ions is exclusively provided by the electric field $E \sim \text{grad}\, p_e$, where p_e is the electron pressure. At the MPB (called protonopause in Sauer *et al.*, 1994), the proton density drops sharply to near zero, forming a proton cavity. Simultaneously, the heavy-ion density increases

sharply. Throughout this boundary, momentum is transferred from the protons to the heavy ions, which, because of their higher mass, move slowly inside the proton cavity (MPR). It is important to note that two wave modes exist in such a bi-ion plasma (McKenzie *et al.*, 1993): one is related to the protons ('proton mode') and the other to the heavy ions ('heavy-ion mode').

The magnetic field is calculated from the electron dynamics, like in gasdynamic models (Spreiter and Stahara, 1980), so that the sharp drop of the electron velocity at the MPB leads to enhanced draping of the magnetic field, and an abrupt increase of its magnitude. This effect is seen in the upper color plot of Figure 6.7, where the magnetic field lines are plotted together with the heavy ion density distribution. The collocation of the draping feature and the change of the ion composition is in agreement with the observation (see Section 3.3).

Results from a 2D simulation, using the above equations, in which the solar wind magnetic field is self-consistently included, have been published recently (Sauer and Dubinin, 2000). The source of heavy ions was taken to be an exospheric/ ionospheric density distribution of oxygen, based on reasonable parameters from the literature (the planetary body itself was ignored). The main aim of these studies was to elucidate the momentum and energy coupling between the proton and heavy-ion fluids. By excluding the high-density part of the ionospheric source distribution, no stagnation of the electron flow (determined by both the proton and heavy-ion flows) appeared in the results,. This implies the absence of a stagnation point of the magnetic field flux, or, in other words, the absence of an ionopause. The grad p_e term plays the dominant role in the momentum coupling between the two ion species. A sharp boundary is formed, the MPB, which separates the upwind protons from heavy ions. This occurs at a location where the heavy-ion densities are relatively low compared to the undisturbed proton density. Simulations with different orientations of the solar wind magnetic field shows that the shape of the MPB becomes asymmetric, being rather sharp on one side, with a more gradual transition on the other side (also see Plate 1 by Sauer *et al.*, 1994). The magnetic field piles up at that boundary where the ion composition changes. Thus there is a general feature consisting of a 'magnetic pile-up boundary' (MPB) coinciding with an 'obstacle boundary' for the proton flow. Moreover, this transition is associated with a drop in the electron temperature, which is an additional signature of the bi-ion transition.

Figure 6.8 shows a comparison between Phobos-2 measurements along (a) the elliptical and (b) the circular orbits with corresponding cuts through the appropriate simulation boxes (Sauer and Dubinin, 2000). Overall, there is good agreement. The variations of both the proton and electron densities demonstrate the efficiency of the bi-ion fluid approach. Whereas the proton density drops down at the MPB, the electron density jumps simultaneously (by virtue of charge-neutrality), indicating a change in the ion composition. Also noteworthy is the sharp change in the temperature at the MPB (Figure 6.8b) shown in both the Phobos-2 measurements and the simulations.

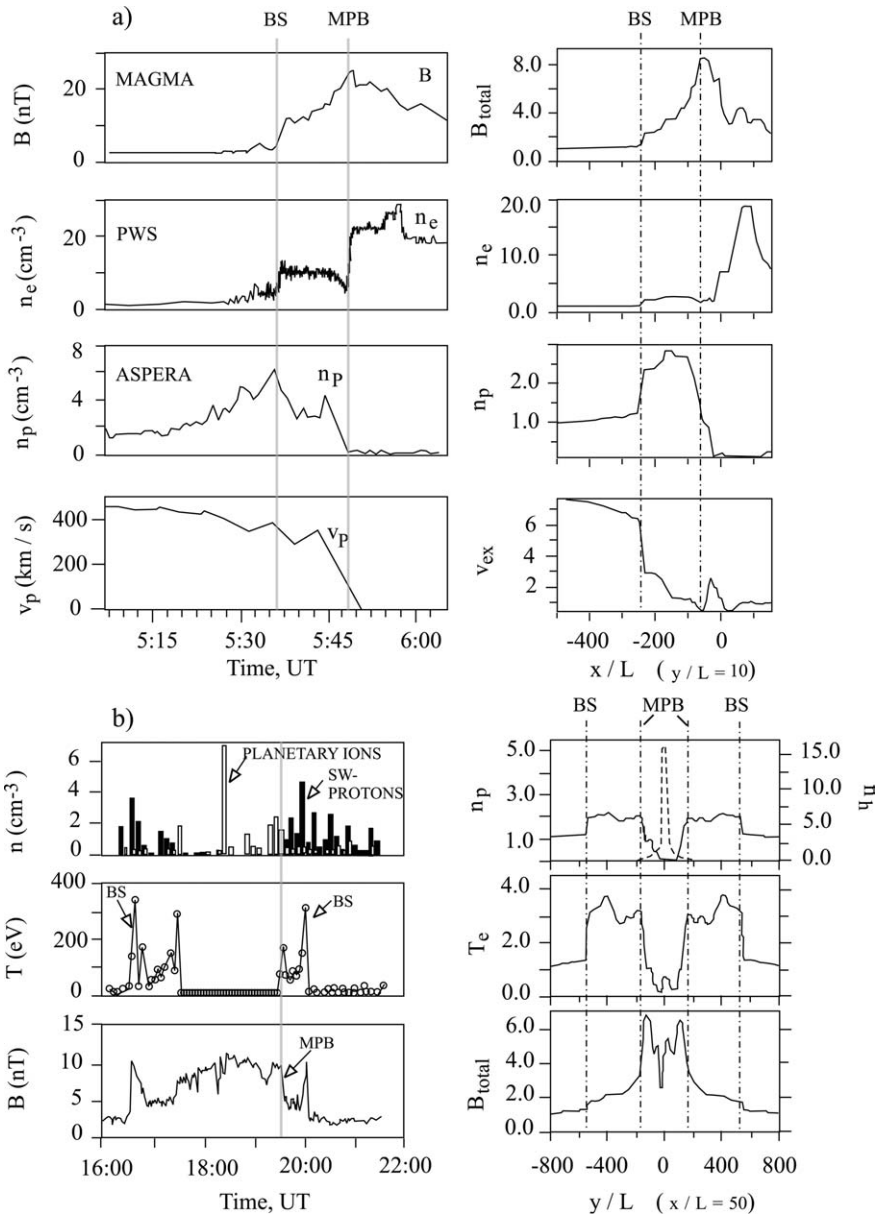

Figure 6.8. Comparison between Phobos-2 measurements (left panels) and bi-ion fluid simulations (right panels) for the third elliptical orbit (a) and one circular orbit (b), after Sauer and Dubinin (2000).

A summary of the insights gained fro the bi-ion fluid simulations is as follows. When the dynamic pressure of the solar wind is not too high, it will be balanced by the ionospheric pressure. Then, three main plasma boundaries exist: the bow shock (BS), the magnetic pile-up boundary (MPB), and the ionopause. The latter may be deformed locally by magnetic anomalies. The MPB is the 'obstacle boundary' for the solar wind protons, determining the position and the shape of the bow shock. In the opposite case of high dynamic solar wind pressure, the ionospheric pressure is insufficient to stand-off the magnetospheric plasma flow, and no ionopause is formed. In this case, the magnetospheric plasma interacts with the localized crustal magnetic fields to create mini-magnetospheres along the flanks of the tail. The MPB is formed in the magnetosheath region, where the exospheric ion density becomes comparable with the solar wind proton density. The other parameters have only a weak influence. This may explain why the bow shock position at Mars does not show the usual solar cycle variation found at Venus.

6.1.4. *Pros and Cons of the Model Approaches*

The solar wind interaction with Mars is a complex physical problem, thus it is appropriate and desirable to have a number of different models available. Given the practical limitations of numerical models described above, each has certain strength and weaknesses. Inter-comparing the results of such calculations, as well as examining agreements and disagreements with observations, advances our understanding of the controlling processes.

In principle, the hybrid kinetic model (e.g., Brecht *et al.*, 1993) should describe the macro and micro-physics of the interaction processes best, and it has been successful in reproducing some of the observed features of the modeled interaction. However, for practical reasons a number of simplifications and assumption must be introduced in order to run the model, thus it also has a number of shortcomings. For example, if one is attempting to perform detailed chemistry calculations then many particles per cell are needed in order to obtain a complete 6 degree of freedom distribution function. This is very costly, and frankly can probably be done as well or better with a fluid approach, unless the distributions are expected to be rather non-maxwellian. Next, the code is complex and requires the developer to be extremely careful in checking the results. This occurs, because particle codes can have numerical instabilities that resemble very closely real plasma instabilities. Further, with the large suite of electromagnetic modes possible in this code care must be given to resolving them both temporally and spatially. This leads to major concerns. Hybrid simulations are computationally intensive and therefore, are not easily run. However, with newer, bigger, and faster machines, even PC's, may be able to run reasonable simulations soon.

On the positive side the MHD model of Ma *et al.* (2002; 2004) is 3D, considers the solar wind protons and the major ionospheric ions separately, via separate continuity equations, and does include the crustal magnetic fields. On the negative side, it assumes only one ion velocity and one plasma temperature. Given all this,

it still provides very good global insight into the interaction, and models bowshock and ionopause locations quite well, consistent with observations. It also predicts the presence of mini-magnetocylinders and gives plasma fluxes, which are also in reasonably good agreement with other estimates and observed values.

The MHD model of Sauer and Dubinin (2000) has, on the positive side, separate momentum equations for the solar wind protons and the heavy planetary ions, allowing for separate velocities. It also allows for momentum transfer by electromagnetic fields from the protons to the heavy ions, which appears to be the fundamental process for the formation of a MPB. In this respect, the use of a 2D model, as long as the electron flow is not stopped, is not a limitation. There is very good agreement between the calculations and the spacecraft observations of the MPB. However, on the negative side, it is a 2D model at this time, and it requires either the assumption of no solid obstacle or axisymmetry. It also neglects ion pressures (temperatures), which result in sharper boundaries, because the cold ions are easy to 'stop' in the simulations. Despite the various shortcomings of the different models, as indicated above, they all make important contributions towards advancing our comprehensive understanding of the interaction processes.

6.2. Hot atoms and X-ray models

The co-existence of solar wind plasma and the planetary neutral gas, results in a strong interaction between them. One of the fundamental collisional interactions is the charge-exchange (CX) process between an energetic ion and cold atmospheric atom, which produces an energetic neutral atom and an ionized gas particle. Examples of CX processes of special importance at Mars are:

$$H_{SW}{}^{+} + H \rightarrow H_{SW} + H^{+}, \tag{6.17}$$

$$H_{SW}{}^{+} + O \rightarrow H_{SW} + O^{+}, \tag{6.18}$$

$$H_{pickup}{}^{+} + H \rightarrow H_{pickup} + H^{+}, \tag{6.19}$$

$$O_{pickup}{}^{+} + H \rightarrow O_{pickup} + H^{+}. \tag{6.20}$$

The first three processes shown above (6.17), (6.18) and (6.19) produce fast hydrogen ENA's, (H-ENA's), while reaction (6.20) produces fast oxygen atoms (O-ENA's). The subscript SW refers to solar wind protons and pickup refers to particles originating from the planetary atmosphere or exosphere. The important feature of these CX processes is that the velocity of the newly formed ENA is about the same as the velocity of the initial energetic ($E \gg 1$ eV) fast ion. Thus the ENA's carry information about the properties of the ions from the site at which they were formed.

The solar wind also contains heavy, multiply charged ions, for example, O^{6+} ions. The charge-exchange with a multiply charged ion, say an n times charged ion X^{n+}, and a neutral, M, is a source of X-ray photons, $h\nu$:

$$X^{n+} + M \rightarrow X^{*(n-1)+} + M^{+} \rightarrow X^{(n-1)+} + M^{+} + h\nu, \tag{6.21}$$

where the superscript * refers to an exited state. The CX processes that produce ENAs and X-rays are of importance from the point of view of potential observations, because they provide opportunities to obtain global images of the source ions.

The Martian atmosphere and exosphere alters the incoming energetic solar wind by (a) 'mass loading' the solar wind with newly created ions produced mainly by photoionization, and solar wind electron impact ionization of the atmospheric gases, and (b) undergoing charge-transfer (charge-exchange) interactions with the solar wind ions. According to some models, a fraction of the solar wind ions (mainly H^+ and He^{++}) directly impact the Martian upper atmosphere near its exobase (at $\sim$ 180 km altitude) (Brecht, 1997b; Kallio and Janhunen, 2001). Others undergo charge-exchange reactions with ambient exospheric and thermospheric neutrals, particularly hydrogen and helium at high altitudes ($h > 500$ km) and oxygen at lower altitudes, and then impact the exobase as ENA's (Kallio *et al.*, 1997). In both cases, solar wind energy is directly deposited into the upper atmosphere, resulting in increased ionization rates and UV emissions. (It should be noted that there is no observational evidence that the solar wind protons required for charge exchange penetrate through the MPB to reach the ionosphere.)

When the effects of such H-ENA precipitation were studied by Monte Carlo simulations, the precipitating hydrogen atoms were estimated to increase the ionization rate by about 1% compared to the ionization rates due to extreme ultraviolet radiation under typical solar wind conditions (Kallio and Barabash, 2000, 2001). This effect is comparable to, or even stronger than similar effects caused by the O^+ and H^+ precipitation (Luhmann and Kozyra, 1991; Brecht, 1997b; Kallio and Janhunen, 2001). Calculations also indicate that a substantial fraction of the precipitating H-ENA is scattered back from the Martian atmosphere, resulting in an H-ENA albedo (Kallio and Barabash, 2001; Holmström *et al.*, 2001). Imaging these H-ENA's would visualize the spots or regions of the most intense ENA precipitation.

All the model calculations described in this section were obtained by using the empirical flow model that is based on Phobos-2 measurements (Kallio, 1996; Kallio and Koskinen, 1999). For all three simulations the atomic and the molecular hydrogen densities were taken from Krasnopolsky and Gladstone (1996) and the cold and hot oxygen densities came from Zhang *et al.* (1993b).

While the energy transfer associated with the proton or ENA precipitation exceeds the one from the O^+ precipitation, the oxygen ions are the ones that cause massive sputtering of the atmosphere (Luhmann and Kozyra, 1991; Luhmann *et al.*, 1992; Kass and Yung, 1995, 1996). The O and CO_2 sputtered by O^+ ions has been estimated to range from 3×10^{23} to 4.7×10^{24}atoms s^{-1}, small compared to the non-thermal escape of the hot oxygen atmospheric component (Kim *et al.*, 1998; Hodges, 2000).

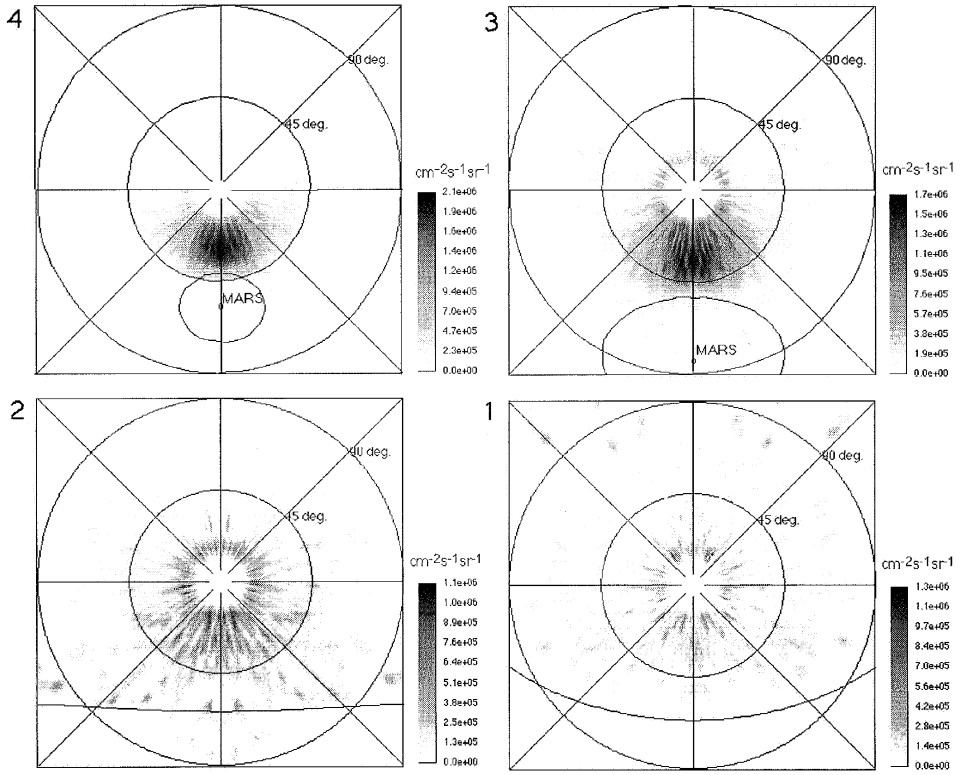

Figure 6.9. Simulated hydrogen ENA particle fluxes at four vantage points No. 4-1 from the apocenter (point No. 4) to the pericenter (point No. 1). The look direction (the polar coordinate axis) is toward the Sun, that is at the center of the images. The inner (outer) circle around the Sun represents the polar angle, θ of 45° (90°). The lines originating from the center of the figures represent constant azimuth angles, φ. The ENAs in the region $\theta < 15°$ are blocked. The solar wind parameters are $n_{sw} = 2.5\ \text{cm}^{-3}$, $U_{sw} = 400\ \text{km s}^{-1}$.

The supersonic solar wind upstream of the bow shock can experience charge-exchange with the Martian hydrogen exosphere (Equation (6.17)) over very long distances resulting in a narrow ($\sim$ 10°) anti-sunward beam of ENA's with the energy of the bulk flow of the solar wind. Figure 6.9 shows simulated directional hydrogen ENA fluxes produced by solar wind protons. The H-ENA flux was integrated over energy as a function of two spherical angles at four positions (1–4) along the orbit of a virtual spacecraft, whose orbit is similar to that of Mars Express. In this fish-eye projection, the look direction (the polar coordinate axis) is toward the Sun. In Figure 6.9 the distance from the Sun (at the center of each of the four images) gives the polar angle, θ. The azimuth angle, φ, measured around the polar axis, was chosen to be zero for the center of Mars. The ENA fish-eye pictures illustrate the integrated fluxes in several directions for the energy range $E > 100$ eV, based on an axially symmetric model for the solar wind proton flow around Mars. Note that in Figure 6.9 the ENA flux at polar angles less than 15° was

set to zero to mimic ENA observations (an ENA instrument cannot look directly toward the Sun because of the EUV radiation from the Sun).

Figure 6.9 illustrates how an H-ENA image evolves when the vantage point moves from the apocenter (position 4) toward the pericenter (position 1). The maximum fluxes are obtained at $\varphi = 0°$, that is, between the Sun and the center of Mars. The spread of the distribution to non-zero φ depends on the proton temperature: a zero proton temperature would give non-zero fluxes only along the $\varphi = 0°$ line, that is, on the line between the Sun and Mars. Non-zero proton temperatures give, instead, non-zero fluxes at other φ angles as well, as is the case in Figure 6.9. Note that the plasma model used is axially symmetric and therefore the solution on the hemisphere $\varphi = 0° - 180°$ and $\varphi = 180° - 360°$ is symmetric. The value of the maximum ENA flux depends on the flux of the solar wind protons, the shape and the distance of the bow shock and the magnetopause, as well as the proton parameters downstream of the bow shock. The ENA fluxes produced by the shocked solar wind are most sensitive to the neutral hydrogen distribution controlled by the exobase temperature and the position of the boundary separating the solar wind and planetary plasmas (Holmström *et al.*, 2002). The ENA images display the entire interaction region and can be converted into global distributions of the proton flow and neutral gas using extracting inversion methods similar to the one developed for Earth (Roelof and Skinner, 2000).

The Martian hydrogen corona provides another source of fast H^+ ions. The accelerated planetary protons, originating from ionization of the hydrogen corona, also charge-exchange with the exospheric gas, resulting in planetary hydrogen ENA emissions (Equation (6.19)). The H-ENAs produced from these pick-up H^+ ions differ from the H-ENAs produced from the shocked solar wind protons in energy, because the pick-up protons can gain an energy up to four times the solar wind energy (Lichtenegger *et al.*, 2002).

The ASPERA/Phobos-2 observations of the plasma inside the Martian magnetosphere have shown the existence of two basic ion populations. The tail beams of H^+ and O^+ with energy 1–3 keV, and the outflowing ionospheric ions, with energy 10–100 eV near the tail flanks (Lundin *et al.*, 1993). The related ENA flux has been estimated to be 10^3 cm^{-2} s^{-1} keV^{-1} for the energy range 1–10 keV, and up to 10^5 cm^{-2} s^{-1} keV^{-1} for lower energies, 10–100 eV (Barabash *et al.*, 1995).

The ENA signal associated with the pick-up oxygen (see Equation (6.20)) was recently investigated in detail by solving numerically the kinetic equations to obtain the global distribution of oxygen ions (Barabash *et al.*, 2002). The O^+ distribution was calculated using self-consistent kinetic simulations (Kallio and Janhunen, 2002), and found, as expected, to have a large asymmetry with respect to the direction of the interplanetary electric field, $\mathbf{E}_{SW} = -\mathbf{U}_{SW} \times \mathbf{B}_{SW}$. When this O^+ distribution was converted to the corresponding O-ENA flux it was found that the fluxes of the oxygen ENA's can reach 10^4 cm^{-2} s^{-1} sr^{-1} eV^{-1} and that it fully reflects the morphology of the oxygen ion population, demonstrating that O-ENA's provide a way to determine the instantaneous oxygen ion escape rate. Similarly, comparison

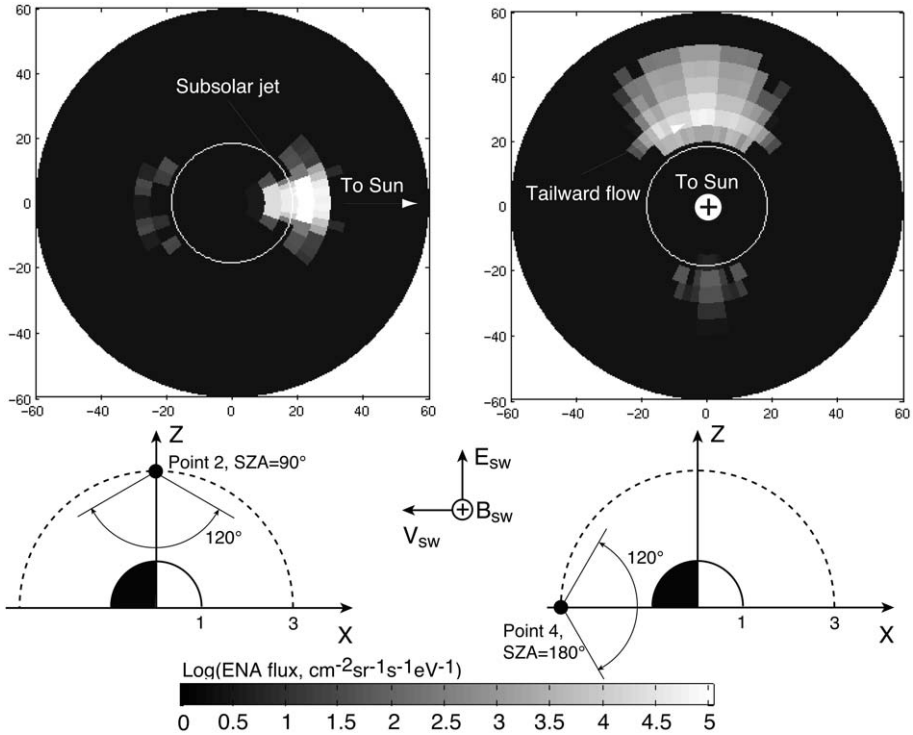

Figure 6.10. Oxygen ENA images for two vantage points: At the terminator plane (point No. 2, the left image) and at the midnight (point No. 4, the right image). The energy range is 0.1–1.65 keV. The position of the vantage points are shown in the inserts as well as the direction of the convective electric field ($\mathbf{E}_{\rm sw}$) in the solar wind, and the interplanetary magnetic field ($\mathbf{B}_{\rm sw}$). Both vantage points are on the *OXZ* plane. The solar wind parameters are $B_{\rm IMF} = 2$ nT, $U_{\rm sw} = 500$ km s^{-1}.

of oxygen ion fluxes measured by the SLED energetic particle telescope onboard Phobos-2 near Mars with predictions from a test particle calculations of pick-up O^+ ions created far from Mars puts limits on the neutral oxygen escape rate from that planet (Cravens *et al.*, 2002).

Figure 6.10 shows an example of the simulated O-ENA images for the energy range of 0.1–1.65 keV. The figure shows the vantage points and the corresponding ENA images in the fish-eye projection for two vantage points, No. 2 and No. 4. The projection is a polar one, with the polar axis pointing towards the center of Mars. The center of Mars is at the center of the figures. The distance from the center of the figures represent the value of the polar theta angle, that is, theta is 0° at the center of the figures. The polar angle is the angle to the solar direction in the plane perpendicular to the planetary center direction.

The energy range selected covers the main oxygen ion population near Mars, and it still makes the result relevant to modern ENA instrumentation. The angular resolution for the line-of-sight grid is 2.5° to 5°. The field of view is 120° in order to cover the entire interaction region. As expected, O-ENA emissions are concen-

Figure 6.11. A computer simulated image of Martian X-ray emissions from charge-exchange between solar wind ions and Mars' exosphere. The view direction is perpendicular to the Mars–Sun line, with the Sun to the left. Mars is seen as a white disc. The solar wind parameters are $n_{\mathrm{sw}} = 2.5\ \mathrm{cm}^{-3}$, $U_{\mathrm{sw}} = 400\ \mathrm{km\ s}^{-1}$.

trated close to the planetary surface, where the neutral density is highest reflecting also the strong asymmetry observed in the ion distribution. Note that Figure 6.10 (point No. 2) shows a strong jet of oxygen ENA coming out from the subsolar point, where the electric and magnetic field configuration effectively accelerates newly formed planetary ions. The tailward flow is also clearly reproduced (Figure 6.10, point 4). In contrast, when simulations for vantage points on the $+Y$ axis at the distance 3 R_M were made, only very weak O-ENA fluxes were obtained. Finally, simulations for a higher energy band of 1.65–5.0 keV showed that O-ENA image morphology is similar to the ones for the lower energy band, but that fluxes are two orders of magnitude lower.

Cravens (2000) suggested that significant X-ray fluxes, resulting from charge-exchange, may be present at Mars (Equation (6.21)). Figure 6.11 shows an example of a computer simulated X-ray image of the solar wind-Mars interaction (Holmström *et al.*, 2002). The maximum directional fluxes were found to be on the order of 10^6 eV cm^{-2} sterad^{-1} s^{-1} and depend on the solar wind conditions and view direction. The energies of the emitted X-rays are mostly below 1 keV.

Several other mechanisms can also generate X-ray emissions at Mars besides charge-exchange between solar wind ions and Mars' exosphere. In particular, fluorescence and elastic scattering of solar X-rays by Mars' atmosphere can also be significant sources. The estimated intensity of Martian X-rays from fluorescent and elastic scattering of solar X-rays somewhat exceeds the charge transfer pro-

duced X-rays (Cravens and Maurellis, 2001), as has just been confirmed by recent Chandra X-ray Observatory observations of Mars (Dennerl *et al.*, 2003). Future observations combined with more precise models for X-ray emissions should allow X-ray imaging to be a complement to ENA imaging in providing global information about the near-Mars space. X-ray emissions from Venus by the X-ray telescope Chandra have also been reported (Dennerl, 2001).

6.3. IONOSPHERE MODELS

As indicated in Section 5.1 the first detection of the ionosphere of Mars was by the Mariner 4 spacecraft in 1965 with the radio occultation experiment (Fjeldbo and Eshleman, 1968), which was soon followed by theoretical interpretations of these results (and that of Venus, as observed by Mariner 5, (Kliore *et al.*, 1967, Eshleman, 1970)). These models were based on photoionization of CO_2 and dissociative recombination of the resulting major ion, CO_2^+ (Herman *et al.*, 1970; McElroy, 1969; Whitten, 1970). However, difficulties arose with this type of model (cf., Bauer, 1973), which motivated the adoption of a more complex chemical scheme involving dissociation products of CO_2, and in particular, atomic oxygen (McElroy and McConnell, 1971; Stewart, 1972; Kumar and Hunten, 1974). The CO_2^+ and O^+ ions created by ionization of the major neutral species, CO_2, are converted to O_2^+ ions, as indicated by the following, simplified chemistry scheme:

$$CO_2 + h\nu \rightarrow CO_2^+ + e, \tag{6.22}$$

$$CO_2^+ + O \rightarrow O_2^+ + CO, \tag{6.23}$$

$$\rightarrow O^+ + CO_2, \tag{6.24}$$

$$O^+ + CO_2 \rightarrow O_2^+ + CO, \tag{6.25}$$

$$O_2^+ + e \rightarrow O + O. \tag{6.26}$$

The dissociative recombination of the O_2^+ ions (Equation (6.26)) produces the hot oxygen corona at both Venus and Mars. (cf., Schunk and Nagy, 2000).

The correctness of this scheme for Mars was confirmed by measurements made by instruments onboard the Viking 1 and 2 landers – the first *in situ* ionospheric measurements ever made for a planet other than Earth. A variety of theoretical models of the ionospheres of Venus and Mars have been developed over the past thirty years. The earliest models were photochemical, but models have become increasingly sophisticated, including both the energetics and magnetohydrodynamic (MHD) processes (cf., Cravens, 1991; Nagy and Cravens, 2002). A photochemical model is appropriate for explaining ion composition for altitudes below about 200 km where chemical time lifetimes are less than transport times. Hanson *et al.* (1977) used such a model to explain the RPA measurements and to deduce the

neutral oxygen abundance (i.e., daytime O to CO_2 ratio of unity at around 200 km, in comparison to 150 km for Venus).

The next step in model sophistication for Mars was the model of Chen *et al.* (1978), who solved the coupled continuity, momentum, and energy equations in one-dimension. Among their findings was that ion transport only affects higher altitudes, although in order to obtain good agreement with measurements above about 250 km, an ion outflow (or escape) upper boundary condition was needed and was presumed to be somehow associated with the solar wind interaction processes. The same model indicated that energy inputs into the ion and electron gases were required at the upper boundary (again presumably associated with the solar wind interaction) in order to obtain agreement with measurements. Other work on the ionospheric energetics has also invoked either energy inputs and/or ionospheric thermal conductivities altered by ionospheric magnetic fields which are induced by the solar wind interaction (see Figure 5.3) (Rohrbaugh *et al.*, 1979; Choi *et al.*, 1998). For example, in the absence of magnetic field effects an input flux of 4×10^9 eV cm^{-2} s^{-1} is needed for the electrons (Choi *et al.*, 1998). Similar studies of the ion composition (Nagy *et al.*, 1980) and the energetics (Cravens *et al.*, 1980) of the Venus ionosphere were undertaken as data was returned from the Pioneer Venus Orbiter (PVO), starting in 1978.

The ion composition and the airglow of the Martian upper atmosphere and ionosphere were examined further by Fox and Dalgarno (1979), and Fox (1993, 1996). Figure 5.1, from the chemical/vertical transport model of Fox (1997), shows both solar minimum and maximum density profiles for a variety of species, including NO^+, N_2^+, CO^+, and C^+, in addition to the three major ions previously discussed. The dominance of O_2^+ as the major ion species independent of solar cycle is evident. By contrast, O^+ is the major ion species at Venus for altitudes above about 170 km (cf., Schunk and Nagy, 2000). To obtain agreement with the Viking data at higher altitudes, Fox (1997) had to assume ion outflow upper boundary conditions, just as Chen *et al.* (1978) did. The deduced flux of O atoms (in all forms) was 5.5×10^7 cm^{-2} s^{-1} for solar minimum and 1.8×10^8 cm^{-2} s^{-1} for solar maximum, values which are comparable to the direct escape rates of O from dissociative recombination of O_2^+ (Fox and Hac, 1997; Kim *et al.*, 1998; Hodges, 2000). Most of the dayside ion outflow will travel to the night, as pointed out by Fox (1997). Some of this trans-terminator flux, will flow down on the nightside and help to maintain the nightside ionosphere, while the rest will escape through the tail (Ma *et al.*, 2002; 2004).

Our understanding of the Martian ionosphere has greatly benefited from the Venus analogy. One-dimensional, multispecies, MHD models of the Venus ionosphere were able to explain the observed structure in both field and density (Shinagawa *et al.*, 1987; Shinagawa and Cravens, 1988). Ion loss due to horizontal day to night flow was included in these models, albeit not self-consistently. Shinagawa (1996) also constructed a two- dimensional MHD model of the Venus ionosphere in which the horizontal flow was handled self-consistently. Similar

multispecies MHD models were constructed for the Martian ionosphere, with and without the inclusion of a small (50 nT or smaller) horizontal intrinsic magnetic field (Shinagawa and Cravens, 1989, 1992). Small intrinsic fields did not significantly affect the ionospheric density structure produced by the models, which was in agreement with the Viking measurements. On the other hand, for a case with an unmagnetized ionosphere (or for ionospheric magnetic fields with significant radial components), plus zero outflow upper boundary condition, Shinagawa and Cravens (1989), found a diffusive equilibrium topside density profile with a plasma scale height larger than the scale height evident in the Viking data. They also stated that this case 'is very similar to what would exist for Mars with a very large intrinsic field, which is completely shielded from the solar wind.' The latest version of the global, 3D, multi-species, MHD model of Ma *et al.* (2004) now has sufficient altitude resolution do be able to do a reasonably good job of estimating the relevant ionospheric parameters. The MGS observations (Acuña *et al.*, 1998; Connerney *et al.*, 1999) showed that: (1) the global-scale intrinsic field is negligibly small, and (2) the field can in places be dominated by large crustal magnetization. The presence of induced horizontal magnetic fields and/or strong crustal fields strongly impacts the ionospheric structure. Theory and modeling efforts have, so far, mainly addressed the Venus-like case of solar wind induced magnetic fields and the associated ionospheric behavior, because of the richness of data from the Pioneer Venus Orbiter. Theoretical interpretations (Krymskii *et al.*, 2002; Ness *et al.*, 2000; Brain *et al.*, 2003) and model calculations (Ma *et al.*, 2002; 2004) of the ionosphere in the presence of crustal magnetization have just begun to appear, as was briefly discussed earlier.

References

Acuña, M. H. *et al.*: 1992, 'Mars Observer Magnetic Fields Investigation', *J. Geophys. Res.* **97**, 7799.

Acuña, M. H. *et al.*: 1998, 'Magnetic Field and Plasma Observations at Mars: Initial Results of the Mars Global Surveyor Mission', *Science* **279**, 1676.

Acuña, M. H. *et al.*: 1999, 'Global Distribution of Crustal Magnetization Discovered by the Mars Global Surveyor MAG/ER Experiment', *Science* **284**, 790.

Acuña, M. H., Connerney, J. E. P., Ness, N. F., Lin, R. P., Mitchell, D., Carlson, C. W., McFadden, J., Anderson, K. A., Rème, H., Mazelle, C., Vignes, D., Wasilewski, P. and Cloutier, P.: 2001, 'The Magnetic Field of Mars : Summary of Results From the Aerobraking and Mapping Orbits', *J. Geophys. Res.* **106**, 23403.

Albee, A. L., Palluconi, F. D. and Arvidson, R. A.: 1998, 'Mars Global Surveyor mission: Overview and Status', *Science* **279**, 1671.

Alfvén, H.: 1957, 'On the Theory of Comet Tails', *Tellus* **9**, 92.

Alexander, C. J. and Russell C. T.: 1985, 'Solar Cycle Dependence of the Location of the Venus Bow Shock', *Geophys. Res. Lett.* **12**, 369.

Arkani-Hamed, J.: 2001, 'A 50-degree Spherical Harmonic Model of the Magnetic Field of Mars', *J. Geophys. Res.* **106**, 23197.

Axford W. I.: 1991, 'A Commentary on Our Present Understanding of the Martian Magnetosphere', *Planetary Space Sci.* **39**, 167.

Barabash, S. *et al.*: 1995, 'Diagnostic of Energetic Neutral Particles at Mars by the ASPERA-C Instrument For the Mars 96 Mission', *Adv. Space Res.* **16**, (4)81.

Barabash, S., Holmström, M., Lukyanov, A. and Kallio, E.: 2002, 'Energetic Neutral Atoms at Mars IV: Imaging of Planetary Oxygen, *J. Geophys. Res.* **107**(A10), 1280.

Bauer, S. J.: 1973, *Physics of Planetary Ionospheres*, Springer-Verlag, New York.

Bauer, S. J. and Hantsch, M. H.: 1989, 'Solar Cycle Variations of the Upper Atmosphere Temperatur of Mars', *Geophys. Res. Lett.* **16**, 373.

Bauer, S. J.: 1999, 'Mars Upper Atmosphere: Response to Solar Activity', *Anzeiger Abt. II* **136**, 19.

Baumgärtel K. and Sauer, K.: 1992, 'Interaction of a Magnetized Plasma Stream with an Immobile Ion Cloud', *Ann. Geophys.* **10**, 763–771.

Bertucci, C., Mazelle, C., Crider, D. et al., 2002, 'Magnetic Field Line Draping Enhancement across the Martian Magnetic Pileup Boundary', EGU Meeting, Nice, France.

Bertucci, C., Mazelle, C., Vignes, D., Crider, D. H., Acuña, M. H., Connerney, J. E. P., Mitchell, D. L., Lin, R. P., Rème, H., Cloutier, R. A., Ness, N. F. and Winterhalter, D.: 2003a, 'Magnetic Field Draping Enhancement at the Magnetic Pileup Boundary from Mars Global Surveyor', Observations, Geophys. Res. Lett. **30**(2), 1099, 10.1029/2002 GL015713.

Bertucci, C., Mazelle, C., Slavin, J. A., Russell, C. T. and Acuna, M. H., 2003b, Magnetic Field Draping Enhancement at Venus; Evidence of Magnetic Pileup Boundary, Geophys. Res. Lett. **30**(17), 1876, doi: 10.1029/2003 GL017271.

Bezrukikh, V. V., Verigin, M. I. and Shutte, N. M.: 1978, 'On the Disclosure of the Heavy Ions in the Region of the Solar Wind Interaction with Mars planet, Kosmicheskie Issledovaniya (Space Research)', **16**(4), 583–587, (in Russian).

Bougher, S. W., Engel, S., Hinson, D. P. and Forbes, J. M.: 2001, Mars Global Surveyor Radio Science Electron Density Profiles: Neutral Atmosphere Implications', *Geophys. Res. Lett.* **16**, 3091.

Brace, L. H. and Kliore, A. J.: 1991, 'The Structure of the Venus Ionosphere', *Space Sci. Rev.* **55**, 81.

Brain, D. A. *et al.*: 2003, 'Reconnection of Martian Crustal Magnetic Fields to the Solar Wind', *J. Geophys. Res.* **108** (A12), 1424, 10.1029/2002 JA009482.

Brannon, J. F., Fox, J. L. and Porter, H. S.: 1993, 'Evidence for Day-to Night Transport at Low Solar Activity in the Venus pre-dawn Ionosphere', *Geophys. Res. Lett.* **20**, 2739.

Brecht, S. H. and Thomas, V. A.: 1988, 'Multidimensional Simulations Using Hybrid Particle Codes', *Comp. Phys. Comm.* **48**, 135.

Brecht, S. H. and Ferrante, J. R.: 1991, 'Global Hybrid Simulation of Unmagnetized Planets: Comparison of Venus and Mars, *J. Geophys. Res.* **96**, 11209.

Brecht, S. H., Ferrante, J. R. and Luhmann, J. G.: 1993, 'Three-dimensional Simulations of the Solar Wind Interaction With Mars', *J. Geophys. Res.* **98**, 1345.

Brecht, S. H.: 1997a, 'Hybrid Simulations of the Magnetic Topology of Mars, *J. Geophys. Res.* **102**, 4743.

Brecht, S. H.: 1997b, 'Solar Wind Proton Deposition into the Martian Atmosphere', *J. Geophys. Res.* **102**, 11287.

Brecht, S. H.: 2002, 'Numerical Techniques Associated with Simulations of Solar Wind Interactions with Non-Magnetized Bodies', *Comparative Aeronomy in The Solar System*, eds. M. Mendillo, A. Nagy and H. Waite, American Geophysical Union, Washington.

Breus, T. K., Krymskii, A. M., Lundin, R., Dubinin, E. M., Luhmann, J. G., Yeroshenko, Ye. G., Barabash, S. V., Mitnitskii, V. Ya., Pissarenko, N. F. and Styashkin, V. A.: 1991, 'The Solar Wind Interaction with Mars: Consideration of Phobos 2 Mission Observations of an Ion Composition Boundary on the Dayside', *J. Geophys. Res.* **96**, 11165–11174.

Breus, T. K. and Krymskii, A. M.: 1992, 'Turbulent Pick-up of New-born Ions near Venus and Mars and Problems of Numerical Modelling of the Solar Wind Interaction with These Planets. –I. Features of the Solar Wind Interaction with Planets', *Planetary Space Sci.* **40**, 121.

Breus, T. K. *et al.*: 1992, 'Turbulent Pick-up of New-born Ions Near Venus and Mars and Problems of Numerical Modelling of the Solar Wind Interaction with These Planets. –II. Two-fluid HD-model', *Planetary Space Sci.* **40**, 131.

Breus, T. K. *et al.*: 1998, 'Conditions in the Martian Ionosphere/atmosphere from a Comparison of a Thermospheric Model with Radio Occultation Data', *Planetary Space Sci.* **46**, 367.

Bryant D., Krimigis, S. M. and Haerendel, G.: 1985, *IEEE Trans. Geosc. Remote Sensing* **GE-23**, 177.

Chen, R. H., Cravens, R. E. and Nagy, A. F.: 1978, 'The Martian Ionosphere in Light of the Viking Observations', *J. Geophys. Res.* **83**, 3871.

Chen, Y, Cloutier, P. A., Crider, D. H., Mazelle, C. and Rème, H.: 2001, 'On the Role of Charge Exchange in the Formation of the Martian Magnetic Pileup Boundary', *J. Geophys. Res.* **106**, 29387.

Choi, Y. W. *et al.*: 1998, 'Effect of the Magnetic Field on the Energetics of Mars's Ionosphere', *Geophys. Res. Lett.* **25**, 2753.

Cloutier P. A. and Daniell, R. E. and Butler: 1973, 'Ionospheric Currents Induced by Solar Wind Interaction with Planetary Atmospheres', *Planetary Space Sci.* **21**, 463.

Cloutier, P. A. and Daniell, R. E.: 1979, 'An Electrodynamic Model of the Solar Wind Interaction with the Ionospheres of Mars and Venus', *Planetary Space Sci.* **27**, 1111.

Cloutier, P. A. *et al.*: 1999, 'Venus-like Interaction of the Solar Wind with Mars', *Geophys. Res. Lett.* **26**, 2685.

Connerney, J. E. P. *et al.*: 1999, 'Magnetic Lineations in the Ancient Crust of Mars, *Science* **284**, 794.

Cravens, T. E., Gombosi, T. I., Kozyra, J. U., Nagy, A. F., Brace L. H. and Knudsen, W. C.: 1980, 'Model Calculations of the Dayside Ionosphere of Venus: Energetics, *J. Geophys. Res.* **85**, 7778.

Cravens, T. E.: 1991, Ionospheric models for Venus and Mars, p. 277 in *Venus and Mars: Atmospheres, Ionospheres, and Solar Wind Interactions*, Geophysical Monograph **66**, American Geophysical Union, Washington DC.

Cravens, T. E., Shinagawa, H. and Luhmann, J. G.: 1997, in S. Bougher, D. Hunten, and R. Phillips (eds.), Magnetohydrodynamic Processes: Magnetic Fields in the Ionosphere of Venus, *Venus II*, University of Arizona Press, Tucson, pp. 61–93.

Cravens, T. E.: 2000, 'X-ray Emission from Comets and Planets', *Adv. Space Res.* **26**, 1443.

Cravens, T. E. and Maurellis, A. N.: 2001, 'X-ray Emission from Scattering and Fluorescence of Solar X-rays at Venus and Mars'. *Geophys. Res. Lett.* **28**, 3043.

Cravens, T. E., Hoppe, A., Ledvina, S. A. and McKenna-Lawlor, S.: 2002, 'Pickup Ions near Mars Associated with Escaping Oxygen Atoms', *J. Geophys. Res.* **107**.

Crider, D. H. *et al.*: 2000, 'Evidence for Electron Impact Ionization in the Magnetic Pile-up Boundary of Mars', *Geophys. Res. Lett.* **27**, 45.

Crider, D. H., Acuña, M., Connerney, J. *et al.*: 2001, 'Magnetic Field Draping Around Mars: Mars Global Surveyor Results', *Adv. Space Res.* **27**(11), 1831.

Crider, D. H., Acuña, M. H., Connerney, J. E. P., Mitchell, D. L., Lin, R. P., Cloutier, P. A., Rème, H., Mazelle, C., Brain, D., Ness, N. F., and Bauer, S.: 2002, 'Observations of the Latitude Dependence of the Location of the Martian Magnetic Pileup Boundary', *Geophys. Res. Lett.* **29**(8), 10.1029/2001 GL013860.

Crider, D. H. *et al.*: 2002, 'Mars Global Surveyor Observations of Solar Wind Magnetic Field Draping Around Mars', *Space Sci. Rev.* **111**(1–2), 203–221.

Crider, D. H., Vignes, D., Krymskii, A. M., Breus, T. K., Ness, N. F., Mitchell, D. L., Slavin, J. A. and Acuña, M. H.: 2003, 'A Proxy for Determining Solar Wind Dynamic Pressure at Mars using Mars Global Surveyor Data', *J. Geophys. Res.* **108** (A12): 1461, 10.1029/2003 JA009875.

Dennerl, K.: 2001, 'Discovery of X-rays from Venus with Chandra. In 'High Energy Universe at Sharp Focus: Chandra Science'. Proceedings of a conference held in St. Paul, MN, 16–18 July 2001. *ASP Conference Series*.

Dennerl, K.: 2002, 'Discovery of X-rays from Mars with Chandra, *Astron. Astrophys.*, **394**, 1119 doi: 10.1051/0004-6361: 20021116.

Dobe, Z., Nagy, A. F. and Fox, J. L.: 1995, 'A Theoretical Study Concerning the Solar Cycle Dependence of the Nightside Ionosphere of Venus', *J. Geophys. Res.* **100**, 14507.

Dolginov Sh., Yeroshenko, Ye. G. and Zhuzgov, D. N.: 1976a, 'Magnetic Field of Mars According to Data Mars-3 and Mars-5 Satellites', *J. Geophys. Res.* **81**, 3353.

Dolginov, Sh., Yeroshenko, Ye. G., Zhuzgov, L. N. Sharova, V. A., Gringauz, K. I., Bezrukikh, V. V., Breus, T. K., Verigin, M. I. and Remizov, A. P.: 1976b, in N. F. Ness (ed.), 'Magnetic Field and Plasma Inside and Outside of the Martian Magnetosphere', *Solar Wind Interaction with the Planets Mercury, Venus, and Mars*, NASA SP-397, 1–20.

Dubinin, E. and Podgorny, I. M.: 1980, 'Combined magnetosphere', *Cosmic Research, Engl. Transl.* **18**, 470.

Dubinin, E. M., Lundin, R., Norberg, O. and Pissarenko, N.: 1993a, 'Ion Acceleration in the Martian Tail: The Phobos Observations, *J. Geophys. Res.* **98**, 3991.

Dubinin, E. M., Lundin, R., Koskinen, H. and Norberg, O.: 1993b, 'Cold Ions at the Bow Shock: Phobos Observations', *J. Geophys. Res.* **98**, 5617.

Dubinin E. M., Lundin, R. and Schwingenschuh, K.: 1994, 'Solar Wind Electrons as Tracers of the Martian Magnetotail Topology, *J. Geophys. Res.* **99**, 21233.

Dubinin E. M., Obod, D., Lundin, R., Schwngenschuh, K. and Grard, R.: 1995, 'Some Features of the Martian Bow Shock', *Adv. Space Res.* **15**(8/9), 423.

Dubinin E. M., Sauer, K., Lundin, R., Baumgartel, K. and Bogdanov, A.: 1996a, 'Structuring of the Transition Region (Plasma Mantle) of the Martian Magnetosphere', *Geophys. Res. Lett.* **23**, 785.

Dubinin, E. M. *et al.*: 1996b, 'Plasma Characteristics of the Boundary Layer in the Martian Magnetosphere', *J. Geophys. Res.* **101**, 27,061.

Dubinin E. M., Sauer, K., Baumgartel, K. and Srivastava, K.: 1998, 'Multiple Shocks Near Mars', *Earth Planets Space* **50**, 279.

Dubinin E. M. and Sauer, K.: 1999, 'The Martian Magnetosphere-A Laboratory for Bi-ion Plasma Investigation', *Astrophys Space Sci.* **264**, 273.

Dubinin E. M., Sauer, K., McKenzie, J. F. and Chanteur, G.: 2002, 'Nonlinear Waves and Solitons Propagating Perpendicular to the Magnetic Field in Bi-ion Plasma with Finite Plasma Pressure', *Nonlinear Processes Geophys.* **9**(2), 87.

Eastman, T. E., DeCoster, R. J. and Frank, L. A.: 1986, 'Velocity Distributions of Ion Beams in the Plasma Sheet Boundary Layer, in *Ion Acceleration in the Magnetosphere and Ionosphere, Geophysical Monograph 38*, AGU, pp. 117, Washington D.C..

Eastwood, J. W.: 1972, 'Consistency of Fields and Particle Motion in the 'Speiser' Model of the Current Sheet', *Planetary Space Sci.* **20**, 1555.

Elphic, R. C. *et al.*: 1980, 'Observations of the Dayside Ionopause and Ionosphere of Venus', *J. Geophys. Res.* **85**, 7679.

Eshleman, V. R.: 1970, 'Atmospheres of Mars and Venus: A Review of Mariner 4 and 5 and Venera 4 Experiments', *Radio Sci.* **5**, 325.

Fjeldbo, G. and Eshleman, V. R.: 1968, 'The Atmosphere of Mars Analyzed by Integral Inversion of the Mariner 4 Occulation Data', *Planetary Space Sci.* **16**, 1035.

Fox, J. L. and Dalgarno, A.: 1979, 'Ionization, Luminosity, and Heating of the Upper Atmosphere of Mars', *J. Geophys. Res.* **84**, 7315.

Fox, J. L.: 1993, 'The Production and Loss of Nitrogen Atoms on Mars', *J. Geophys. Res.* **98**, 3297.

Fox, J. L.: 1996, in G. W. F. Drake (ed.), 'Aeronomy', *Atomic, Molecular, and Optical Physics Handbook*, 940, Am. Institute Phys. Press, Woodbury, NY.

Fox, J. L.: 1997, 'Upper Limits to the Outflow of Ions at Mars: Implications for Atmospheric Evolution', *Geophys. Res. Lett.* **24**, 2901.

Fox, J. L. and Stewart, A. I. F.: 1991, 'The Venus Ultraviolet Aurora a Soft Electron Source', *J. Geophys. Res.* **96**, 9829.

Fox, J. L. and Hac, A.: 1997, 'Spectrum of Hot O at the Exobase of the Terrestrial Planets', *J. Geophys. Res.* **102**, 24005.

Gan, L., Cravens, T. E. and Horanyi, M.: 1990, 'Electrons in the Ionopause Boundary Layer of Venus', *J. Geophys. Res.* **95**, 19023.

Gombosi T. I. *et al.*: 1981, 'The Role of Charge-exchange in the Solar Wind Absorption by Venus4, *Geophys. Res. Lett.* **8**, 1265.

Grard, R., Pedersen, A., Klimov, S., Savin, S., Skalsky, A., Trotignon, J. G. and Kennel, C.: 1989, 'First Measurements of Plasma Waves near Mars', *Nature* **341**, 607.

Grard, R., Nairn, C., Pedersen, A., Klimov, S., Savin, S., Skalsky, A. and Trotignon, J. G.: 1991, 'Plasma and Waves Around Mars', *Planetary Space Sci.* **39**, 89.

Grard, R., Skalsky, S. and Trotignon, J. G.: 1993, in T.J. Combosi (ed.), 'Selected Wave and Plasma Features of the Martian Environment, *Plasma Environment of non-Magnetic Planets, COSPAR Colloq. Ser.* **4**, Pergamon, New York, pp. 321.

Gringauz K. I., Bezrukhikh, V. V., Verigin, M. I. and Remizov, A. P.: 1975, 'Studies of Solar Plasma Near Mars and Along the Earth-Mras Path, 3. Characteristics of Ion and Electron Components Measured on Satellite Mars-5', *Cosmic Res.* **13**, 107.

Gringauz, K. I., Bezrukikh, V. V., Verigin, M. I. and Remizov, A. P.: 1976, 'On Electron and Ion Component of Plasma in the Antisolar Part of Near-martian Space, *J. Geophys. Res.* **81**, 3349.

Gringauz, K. I.: 1976, 'Interaction of Solar Wind with Mars as Seen by Charged Particle Traps on Mars 2, 3 and 5 Satellites', *Rev. Geophys. Space Phys.* **14**, 391.

Gringauz, K. I.: 1981, 'A Comparison of the Magnetospheres of Mars, Venus and the Earth', *Adv. Space Res.* **1**(1), 5.

Haider, S. A., Kim, J., Nagy, A. F., Keller, C. N., Verigin, M. I., Gringauz, K. I., Shutte, N. M., Szego, K. and Kiraly, P.: 1992, 'Calculated Ionization Rates, Ion Densities, and Aiglow Emission Rates Due to Precipitating Electrons in the Nightside Ionosphere of Mars', *J. Geophys. Res.* **97**, 10637.

Hanson, W. B., Sanatani, S. and Succaro, D. R.: 1977, 'The Martian Ionosphere as Observed by the Viking Retarding Potential Analyzers', *J. Geophys. Res.* **82**, 4351.

Hanson, W. B. and Mantas, G. P.: 1988, 'Viking Electron Temperature Measurements: Evidence for a Magnetic Field in the Martian Ionosphere', *J. Geophys. Res.* **93**, 7538.

Harned, D. S.: 1982, 'Quasineutralhybrid Simulation of Macroscopic Plasma Phenomena', *J. Comp. Phys.* **47**, 452.

Harnett, E. M. and Winglee, R. M.: 2003, 'The Influence of a Mini-magnetopause on the Magnetic Pileup Boundary of Mars' *Geophys. Res. Lett.*, **30**, 20, 2074, doi: 1029/2003 GLO17852.

Herman, J. R., Hartle, R. E. and Bauer, S. J.: 1970, 'The Dayside Ionosphere of Venus', *Planetary Space Sci.* **19**, 443.

Hill, T. W.: 1975, 'Magnetic Merging in a Collisionless Plasma', *J. Geophys. Res.* **80**, 4689.

Hodges, R. R.: 2000, 'Distributions of Hot Oxygen for Venus and Mars', *J. Geophys. Res.* **105**, 6971.

Holmström, M., Barabash, S. and Kallio, E.: 2001, 'X-ray Imaging of the Solar Wind-Mars Interaction'. *Geophys. Res. Lett.* **28**, 1287.

Holmström, M., Barabash, S. and Kallio, E.: 2002, 'Energetic Neutral Atoms at Mars I: Imaging of Solar Wind Protons', *J. Geophys. Res.* **107**(A10), 1277.

Ip, W.-H.: 1992a, 'Ion Acceleration at the Current Sheet of the Martian Magnetosphere', *Geophys. Res. Lett.* **19**, 2095.

Ip W.-H.: 1992b, 'Neutral Particle Environment of Mars: The Exosphere-plasma Interaction Effects', *Adv. Space Res.* **12**(9), 205.

Ip W.-H., Breus, R. K. and Zarnowiecki, T.: 1994, 'Termination of the Solar Wind Flow Near Mars by Charge-exchange', *Planetary Space Sci.* **42**, 435.

Izakov, M. N. and Roste, O. Z.: 1996, 'Martian Upper Atmosphere Structure Variation', *Cosmich. Issled.* **34**, N3.

Israelevich P. L. *et al.*: 1994, 'The Induced Magnetosphere of Comet Halley: Interplanetary Magnetic Field During Giotto Encounter', *J. Geophys. Res.* **99**, 6575.

Kallio, E., Koskinen, H., Barabash, S., Lundin, R., Norberg, O. and Luhmann, J. G.: 1994, 'Proton Flow in the Martian Magnetosheath', *J. Geophys. Res.* **99**, 23547.

Kallio, E.: 1996, 'An Empirical Model of the Solar Wind Flow Around Mars' *J. Geophys. Res.* **101**, 11133.

Kallio, E., Luhmann, J. G. and Barabash, S.: 1997, 'Charge Exchange Near Mars: The Solar Wind Absorption and Energetic Neutral Atom Production', *J. Geophys. Res.* **102**, 22183.

Kallio, E. and Koskinen, H.: 1999, A Test Particle Simulation of Oxygen Ions and Solar Wind Protons Near Mars', *J. Geophys. Res.* **104**, 557.

Kallio, E. and Barabash, S.: 2000, 'On the Elastic and Inelastic Collisions Between the Precipitating Energetic Hydrogen Atoms and the Martian Atmospheric Neutrals', *J. Geophys. Res.* **105**, 24973.

Kallio, E. and Barabash, S.: 2001, 'Atmospheric Effects of Precipitating Energetic Hydrogen Atoms to the Martian Atmosphere', *J. Geophys. Res.* **106**, 165–177.

Kallio, E. and Janhunen, P.: 2001, 'Atmospheric Effects of Proton Precipitation in the Martian Atmosphere and its Connection to the Mars-Solar Wind Interaction', *J. Geophys. Res.* **106**, 5617.

Kallio, E. and Janhunen, P.: 2002, 'Ion Escape from Mars in a Quasi-neutral Hybrid Model', *J. Geophys. Res.* **107**(A3), 10.1029/2001 JA000090.

Kass, D. M. and Yung, Y. L.: 1995, 'Loss of Atmosphere from Mars due to Solar Wind Sputtering, *Science* **268**, 697.

Kass, D. M. and Yung, Y. L.: 1996, 'Response: The Loss of Atmosphere from Mars', *Science* **274**, 1932.

Keating G. M. *et al.*: 1998, 'The Structure of the Upper Atmosphere of Mars. In situ Accelerometer Measurements from Mars Global Surveyor', *Science* **279**, 1672.

Kim, J., Nagy, A. F., Fox, J. L. and Cravens, T. E.: 1998, 'Solar Cycle Variability of Hot Oxygen Atoms at Mars', *J. Geophys. Res.* **103**, 29339.

Kivelson, M. G., Khurana, K. K. and Volwerk, M.: 2002, 'The Permanent and Inductive Magnetic Moments of Ganymede.' *Icarus*, **157**, 2, 502.

Kliore, A. J. *et al.*: 1967, 'Atmosphere and Ionosphere of Venus from Mariner 5 S-band Radio Occultation Experiment', *Science* **158**, 1683.

Kliore A. J., Cain, D. C., Fjeldbo, G., Seidel, B. L. and Rasool, S. I.: 1972, 'Mariner-9 S-band Occultation Experiment: Initial Results on the Atmosphere and Topography of Mars', *Science* **175**, 313.

Kliore A. J., Fjeldbo, G., Seidel, B. L., Sykes, M. J. and Woiceshyn, P. M.: 1973, 'S-band Radio Occultation Measurements of the Atmosphere and Topography of Mars with Mariner 9 - Extended Mission Coverage of Polar and Intermediate Latitudes', *J. Geophys. Res.* **78**, 4331.

Kliore, A. J.: 1992, 'Radio Occultation Observations of the Ionospheres of Mars and Venus, *Venus and Mars: Atmospheres, Ionospheres and Solar Wind Interactions*', 265, *Geophys. Monograph* **66**, American Geophysical Union.

Kotova, G. A., Verigin, M. I., Shutte, N. M., Remizov, A. P., Rosenbauer, H., Riedler, W., Schwingenschuh, K., Zhang, T.-L., Szego, K. and Tatrallyay, M.: 1997a, 'Planetary Heavy Ions in the Magnetotail of Mars: Results of the TAUS and MAGMA Experiments Aboard PHOBOS 2', *Adv. Space Res.* **20**(2), 173.

Kotova, G., Verigin, M., Remizov, A., Shutte, N., Slavin, J., Szego, K., Tatrallyay, M., Rosenbauer, H., Livi, S., Richter, A., Schwingenschuh, K. and Zhang, T.-L.: 1997b, 'The study of the Solar Wind Deceleration Upstream of the Martian Terminator Bow Shock', *J. Geophys. Res.* **102**, 2165.

Kotova, G. A., Verigin, M. I., Remizov, A. P., Shutte, N. M., Rosenbauer, H. *et al.*: 2000a, 'Heavy Ions in the Magnetosphere of Mars: Phobos 2/TAUS Observations', *Phys. Chem. of the Earth (C)* **25**, 157.

Kotova G. A., Verigin, M. I., Remizov, A. P., Rosenbauer, H., Livi, S., Riedler, W., Schwingenschuh, K., Tatrallyay, M., Szego, K. and Apathy, I.: 2000b, 'On the Possibility of Identifying of Heavy Ion Acceleration Processes in the Magnetotail of Mars', *Earth Planets Space* **52**.

Krasnopolsky, V. A. and Gladstone, G. R.: 1996, 'Helium on Mars: EUVE and PHOBOS Data and Implications for Mars'Evolution', *J. Geophys. Res.* **101**, 15765.

Krymskii, A. M.: 1992, in J. G. Luhmann, M. Tatrallyay, and R. O. Pepin (eds.), 'An Interpretation of the Large Scale Ionospheric Magnetic Fields and the Altitude Distribution of the Ionosphere Plasma on the Dayside of Venus and Mars, *Venus and Mars, Atmospheres, Ionospheres, and Solar Wind Interactions, Geophys. Monograph* **66**, 289.

Krymskii, A. M., Breus, T. K., Ness, N. F. and Acuña, M. H.: 2000, 'The IMF Pile-up Regions near the Earth and Venus: Lessons for the Solar Wind – Mars Interaction', *Space Sci. Rev.* **92**, 535.

Krymskii, A. M., Breus, T. K., Ness, N. F., Acuña, M. H., Connerney, J. E. P., Crider, D. H., Mitchell, D. L. and Bauer, S. I.: 2002, 'Structure of the Magnetic Field Flux Connected with Crustal Magnetization and Top-side Ionosphere of Mars', *J. Geophys. Res.* **107** (A9), 1245, doi: 10.1029/2001 JAO000239.

Kumar, S. and Hunten, D. M.: 1974, 'An Ionospheric Model With an Exospheric Temperature of 350 K', *J. Geophys. Res.* **79**, 2529.

Leblanc, F. and Johnson, R. E.: 2002, 'Role of Molecular Species in Pickup Ion Sputtering of the Martian Atmosphere', *J. Geophys. Res.* **107**(E2), 10.1029/2000JE001473.

Lichtenegger, H., Schwingenschuh, K., Dubinin, E. and Lundin, R.: 1995, 'Particle Simulation in the Martian Magnetotail', *J. Geophys. Res.* 21659.

Lichtenegger, H., Dubinin, E. and Ip, W.-H.: 1997, 'The Depletion of the Solar Wind near Mars', *Adv. Space Res.* **20**(2), 143.

Lichtenegger, H. and Dubinin, E.: 1998, 'Model Calculations of the Planetary Ion Distribution in the Martian Tail', *Earth Planets Space* **50**, 445.

Lichtenegger, H. and Dubinin, E.: 1999, 'Charge-exchange in the Magnetosheath of Mars', *Adv. Space Res.*.

Lichtenegger, H., Dubinin, E., Schwingenschuh, K. and Riedler, W.: 2000, 'The Martian Plasma Environment: Model Calculations and Observations', *Adv. Space Res.* **26**, 1623.

Lichtenegger, H., Lammer, H. and Stumptner, W.: 2002, 'Energetic Neutral Atoms at Mars III: Flux and Energy Distribution of Planetary Energetic H atoms', *J. Geophys. Res.* **107**, (A10), 1279, doi: 10.1029/2001 JA000322.

Liu, Y., Nagy, A. F., Clinton, P. T., Groth, D. L., DeZeeuw, L. and Gombosi, T. I.: 1999, '3D multi-fluid MHD Studies of the Solar Wind Interaction with Mars', *Geophys. Res. Lett.* **26**, 2689.

Liu, Y, Nagy, A. F., Gombosi, T. I., DeZeeuw, D. L. and Powell, K. G.: 2001, 'The Solar Wind Interaction with Mars: Results of Three-dimensional Three-species MHD Studies', *Adv. Space Res.* **27**, 1837.

Luhmann, J. G.: 1986, 'The Solar-Wind Interaction with Venus', *Space Sci. Rev.* **44**(3–4, 241.

Luhmann, J. G. and Cravens, T. E.: 1991, 'Magnetic Fields in the Ionosphere of Venus', *Space Sci. Rev.* **55**, 201.

Luhmann, J. G. and Kozyra, J. U.: 1991, 'Dayside Pickup Oxygen Ion Precipitation at Venus and Mars: Spatial Distributions, Energy Deposition and Consequences', *J. Geophys. Res.* **96**, 5457.

Luhmann, J. G. *et al.*: 1987, 'Characteristics of the Mars-like Limit of the Venus – Solar Wind Interaction', *J. Geophys. Res.* **92**, 8545.

Luhmann, J. G., Russell, C. T., Schwingenschuh, K. and Yeroshenko, Ye.: 1991, 'A Comparison of Induced Magnetotails of Planetary Bodies: Venus, Mars, and Titan', *J. Geophys. Res.* **95**, 11199.

Luhmann, J. G. *et al.*: 1992, 'Evolutionary Impact of Sputtering of the Martian Atmosphere by O+ Pickup Ions', *Geophys. Res. Lett.* **19**, 2151.

Lundin, R., Zakharov, A., Pellinen, R., Borg, H., Hultqvist, B., Pissarenko, N., Dubinin, E. M., Barabash, S. V., Liede, I. and Koskinen, H.: 1989, 'First Measurements of the Oonospheric Plasma Escape from Mars', *Nature*, **341**, 6243, 609.

Lundin, R. *et al.*: 1990, 'Plasma Composition Measurements of Martian Magnetosphere Morphology', *Geophys. Res. Lett.* **17**, 877.

Lundin, R. and Dubinin, E. M.: 1992, 'Phobos-2 Results on the Ionospheric Plasma Escape from Mars', *Adv. Space Res.* **12**(9), 255.

Lundin, R. *et al.*: 1993, in T. I. Gombosi (ed.), 'ASPERA Observations of Martian Magnetospheric Boundaries', *Plasma Environments of Non-magnetic Planets* Pergamon Press, p. 311.

Ma, Y., Nagy, A. A. F., Hansen, K. C., DeZeeuw, D. L., Gombosi, T. I. and Powell, K. G.: 2002, '3D Multi-fluid MHD Studies of the Solar Wind Interaction with Mars in the Presence of Crustal Fields', *J. Geophys. Res.* **107**, (in press).

Ma, Y., Nagy, A. F. and Sokolov, I. V. and K. C. Hansen: 2004, 3D, Multispecies, High Spatial Presolution MHD Studies of the Solar Wind Interaction with Mars, *J. Geophys. Res.*, **109**, 2003 JAO10367.

Mahajan, K. K. and Mayr, H. G.: 1989, 'Venus Ionopause During Solar Minimum', *Geophys. Res. Lett.* **16**, 1477.

Mantas, G. P. and Hanson, W. B.: 1979, 'Photoelectron Fluxes in the Martian Ionosphere', *J. Geophys. Res.* **84**, 369.

Marubashi, K., Grebowsky, J. M., Taylor, H. A. *et al.*: 1985, 'Magnetic Field in the Wake of Venus and the Formation of Ionospheric Holes', *J. Geophys. Res.* **90**, 1385.

Mazelle, C., Rème, H., Sauvaud, J. A., d'Uston, C., Carlson, C. W., Anderson, K. A., Curtis, D. W., Lin, R. P., Korth, A., Mendis, D. A., Neubauer, F. M., Glassmeier, K. H. and Raeder, J.: 1989, 'Analysis of Suprathermal Electron Properties at the Magnetic Pile-up Boundary of Comet P/Halley', *Geophys. Res. Lett.* **16**(9), 1035.

Mazelle, C, Rème, H., Neubauer, F. M. and Glassmeier, K.-H.: 1995, 'Comparison of the Main Magnetic and Plasma Features in the Environments of Comets Grigg-skjellerup and Halley', *Adv. Space Res* **16**, (4)41–(4)45.

Mazelle C., Vignes, D., Rème, H., Sauvaud, J. A., d'Uston, C., Acuña, M. H., Connerney, J. E. P., Wasilewski, P., Lin, R. P., Mitchell, D. L., Anderson, K. A., Carlson, C. W., McFadden, J., Curtis, D. W., Cloutier, P. A., Crider, D. H., Law, C. C., Bauer, S. J., Ness, N. F. and Winterhalter, D.: 1998, 'Analysis of the Magnetic 'Pile-up' Boundary at Mars, *Eos Trans. AGU* Fall Meet. Suppl., Abstract P12A-09.

Mazelle, C., Bertucci, C., Rème, H., Mitchell, D. L., Lin, R. P., Vignes, D., Crider, D. H., Acuña, M. H., Connerney, J. E. P., Sauer, K., Chen, Y., Cloutier, P. A., Ness, N. F., and Winterhalter, D.: 2002, 'The Magnetic Pileup Boundary at Mars: A Comet-like Feature in the Interaction of the Planet Atmosphere with the Solar Wind', *in preparation*.

McComas D. J., Spence, H. E., Russell, C. T. *et al.*: 1986, 'The Average Magnetic-field Draping and Consistent Plasma Properties of the Venus Magnetotail'. *J Geophys Res.* **91**, 7939.

McElroy, M. B.: 1969, 'Structure of the Venus and Mars Atmospheres', *J. Geophys. Res.* **74**, 29.

McElroy, M. B. and McConnell, J. C.: 1971, 'Atomic Carbon in the Atmospheres of Mars and Venus', *J. Geophys. Res.* **76**, 6674.

McElroy, M. B. and McConnell, J. C.: 'Dissociation of CO_2 in the Martian Atmosphere', *J. Atmos. Sci.* **28**, 1437.

McKenzie J. F., Marsch, E., Baumgartel, K. and Sauer, K.: 1993, 'Wave and Stability Properties of Multi-ion Plasmas with Applications to Winds and Flows', *Annal. Geophysikae* **11**, 341.

McKenzie J. F., Sauer, K. and Dubinin, E.: 2001, 'Stationary Waves in a Bi-ion Plasma Transverse to the Magnetic Field', *J. Plasma Physics* **65**, 197.

Mellott, M. M. and Livesey, W. A.: 1987, 'Shock Overshoots Revisited', *J. Geophys. Res.* **92**, 13661.

Michel, F. C.: 1971, 'Solar-wind-induced Mass Loss from Magnetic Field-free Planets', *Planetary Space Sci.* **19**, 1580.

Mitchell, D. L. *et al.*: 2000, 'Oxygen Auger Electrons Observed in Mars' Ionosphere', *Geophys. Res. Lett.* **27**, 1827.

Mitchell, D. L., Lin, R. P., Mazelle, C., Rème, H., Cloutier, P. A., Connerney, J. E. P., Acuña, M. H. and Ness, N. F.: 2001, 'Probing Mars' Crustal Magnetic Field and Ionosphere with the MGS Electron Reflectometer', *J. Geophys. Res.* **106**, 23419.

Mitchell, D. L., Lin, R. P., Rème, H., Cloutier, P. A., Connerney, J. E. P., Acuña, M. H. and Ness, N. F.: 2002, 'Probing Mars' Crustal Magnetic Field and Ionosphere with the MGS Electron Reflectometer, Lunar and Planetary Science XXXIII.

Motschmann, U., Sauer, K., Roatsch, T. and McKenzie, J. F.: 1991, 'Subcritical Multiple-ion Shocks', *J. Geophys. Res.* **96**, 13841.

Möhlmann, D. *et al.*: 1991, 'The Question of an Internal Martian Magnetic Field', *Planetary Space Sci.* **39**, 83.

Möhlmann D.: 1992, 'The Question of a Martian Planetary Magnetic Field', *Adv. Spave. Res.* **12**(8), 213.

Mura, A., Milillo, A., Orsini, S., Kallio, E. and Barabash, S.: 2002, 'Energetic Neutral Atoms at Mars II: Energetic Neutral Atom Production near Phobos', *J. Geophys. Res.* **107**(A10), 1278.

Nagy, A. F., Cravens, T. E., Smith, S. G., Taylor, H. A. and Brinton, H. C.: 1980, 'Model Calculations of the Dayside Ionosphere of Venus: Ionic Composition', *J. Geophys. Res.* **85**, 7795.

Nagy, A. F., Gombosi, T. I., Szego, K., Sagdeev, R. Z., Shapiro, V. D. and Shevchenko, V. I.: 1990, 'Venus Mantle - Mars Planetosphere: What are the Similarities and Differences', *Geophys. Res. Lett.* **17**, 865.

Nagy, A. F. and Cravens, T. E.: 1997, in S. W. Bougher, D. M. Hunten and R. J. Phillips (Eds.), 'Ionosphere: Energetics', *Venus II* p. 189.

Nagy, A. F. and Cravens, T. E.: 2002, in M. Mendillo, A. Nagy and H. Waite (Eds.), 'Solar System Ionospheres', *Atmospheres in the Solar System: Comparative Aeronomy* p. 39, Geophys. Mon. 130, American Geophysical Union.

Ness, N. F., Acuña, M. H., Connerney, J., Wasilewski, P., Mazelle, C., Sauvaud, J., Vignes, D., d'Uston, C., Rème, H., Lin, R., Mitchell, D. I., McFadden, J., Curtis, D., Cloutier, P. and Bauer, S.: 1999, 'MGS Magnetic Fields and Electron Reflectometer Investigation: Discovery of Paleomagnetic Fields due to Crustal Remnance', *Adv. Space Res.* **23**(11), 1876.

Ness, N. F. *et al.*: 2000, 'Effects of Magnetic Anomalies Discovered at Mars on the Structure of the Martian Ionosphere and Solar Wind Interaction as Follows from Radio Occultation Experiment' *J. Geophys. Res.* **105**, 15991.

Neubauer, F. M.: 1987, 'Giotto Magnetic-field Results on the Boundary of the Pile-up Region and the Magnetic Cavity', *Astron. Astropys.* **187**, 73.

Neubauer, F. M., Marschall, H., Pohl, M., Glassmeier, K.-H., Musmann, G., Mariani, F., Acuña, . H., Burlaga, L. F., Ness, N. F., Wallis, M. K., Schmidt, H. U. and Ungstrup, E.: 1993, 'First Results from the Giotto Magnetometer Experiment During the P/Grigg-Skjellerup Encounter', *Astron. Astrophys.* **268**, L5–L8.

Nier, A. J. and McElroy, M. B.: 1977, 'Composition and Structure of the Mars' Upper Atmosphere: Results from the Neutral Mass Spectrometers on Viking 1 and 2', *J. Geophys. Res.* **82**, 4241.

Norberg, O., Barabash, S. and Lundin, R.: 1993, in T. Gombosi (ed.), 'Observations of Molecular Ions in the Martian Plasma Environment', *Plasma Environments of Non-magnetic Planets, COSPAR Colloquia Series*, **4**, p. 299.

Paxton, L. J. and Anderson, D. E.: 1991, 'Far Ultraviolet Remote Sensing of Venus and Mars', in *Venus and Mars: Atmospheres, Ionospheres, and Solar Wind Interactions*, 112, Geophysical Monograph 66, American Geophysical Union, Washington DC.

Pedersen A., Nairn, C., Grard, R. and Schwingenschuh, K.: 1991, 'Deviation of Electron Densities from Differential Potential Measurements Upstream and Downstream of the Bow Shock and in the Magnetosphere of Mars', *J. Geophys. Res.* **96**, 11243.

Phillips, J. L., Luhmann, J. G. and Russell, C. T.: 1984, 'Growth and Maintenance of Large-scale Magnetic Fields in the Dayside of Venus', *J. Geophys. Res.* **89**, 10676.

Powell *et al.*: 1999, 'A solution-adaptive Upwind Scheme for Ideal Magnetohydrodynamics', *J. Comp. Phys.* **154**, 284.

Rasool, S. I. and Stewart, R. W.: 1971, 'Results and Interpretation of S-band Occultation Experiments n Mars and Venus', *J. Atmos. Sci.* **28**, 869.

Rème, H., Mazelle, C., Sauvaud, J. A., d'Uston, C., Froment, F., Lin, R. P., Anderson, K. A., Carlson, C. W., Larson, D. E., Korth, A., Chaizy, P. and Mendis, D.A.: 1993, 'Electron Plasma Environment at Comet Grigg-Skjellerup: General Observations and Comparison with the Environment at Comet Halley', *J. Geophys. Res.* **98**, 20965.

Riedler, W,., Mohlmann, D., Oraevsky, V. N., Schwingenschuh, K., Eroshenko, Ye., Rustenbach, J., Aydogar, Oe., Berghofer, G., Lichtenegger, H., Delva, M., Schelch, G., Pirsch, K., Fremuth, G., Steller, M., Arnold, H., Raditsch, T., Ayster, U., Fornacon, K.-H., Schenk, H. J., Michaelis, H., Motschmann, U., Roatsch, T., Sauer, K., Schroter, R., Kurths, J., Lenners, D., Linthe, J., Kobzev, V., Styashkin, V., Achache, J., Slavin, J., Luhmann, J. G. and Russell, C. T.: 1989, 'Magnetic Fields Near Mars: First Results', *Nature* **341**, 604.

Roelof, E. C. and Skinner, A. J.: 2000, 'Extraction of Ion Distributions from Magnetospheric and EUV Images', *Space Sci. Rev.* **91**, 437.

Rohrbaugh, R. P., Nisbet, J. S., Blauler, E. and Hesman, J. R.: 1979, 'The Effect of Energetically Produced O2+ on the Ion Temperatures of the Martian Thermosphere', *J. Geophys. Res.* **84**, 3327, 1979.

Rosenbauer, H., N. Shutte, I. Apathy, A. Galeev, K. Gringauz, H. Gruenwaldt, P. Hemmerich, K. Jockers, P. Kiraly, G. Kotova, S. Livi, E. Marsh, A. Richter, W. Riedler, A. Remizov, R. Schwenn, K. Schwingenschuh, M. Steller, K. Szego, M. Verigin, and M. Witte, Ions of martian origin and plasma sheet in the martian magnetotail: Initial results of TAUS experiment, Nature, 341, 612, 1989.

Rosenbauer, H., M. Verigin, G. Kotova, S. Livi, A. Remizov, W. Riedler, K. Schwingenschuh, N. Shutte, J. Slavin, K. Szego, M. Talrallyay and T.-L. Zhang: 1994, On the Correlation of the Magnetic Field in the Martian Magnetotail to the Solar Wind Parameters, *J. Geophys. Res.* **99**, 17199.

Russell, C. T., Hoppe, M. M. and Livesay, W. A.: 1982, 'Overshoots in Planetary Bow Shocks', *Nature* **296**, 45.

Russell, C. T.: 1985, in B. Tsurutani and R. Stone (eds) *Planetary bow shocks, Collisionless Shocks in the Heliosphere: Reviews of Current Research, Geophysical Monograph* **35**, Washington DC, p. 109.

Russell, C. T. *et al.*: 1988, 'Solar and Interplanetary Control of the Location of the Venus Bow Shock', *J. Geophys. Res.* **93**, 5461.

Sagdeev, R. Z. and Zakharov, A. V.: 1989, 'Brief History of the Phobos Mission', *Nature* **341**, 585.

Sauer K., Baumgärtel, K., Axnäs, I. and Brenning, N.: 1990, 'A Fluid Simulation of the AMPTE Solar Wind Lithium Release', *Adv. Space Res.* **10**, 95.

Sauer, K., Roatsch, T., Motschmann, U., Schwingenschuh, K., Lundin, R., Rosenbauer, H. and Livi, S.: 1992, 'Observations of Plasma Boundaries and Phenomena around Mars with Phobos 2', *J. Geophys. Res.* **97**, 6227.

Sauer, K., Roatsch, T., Baumgartel, K. and McKenzie, J. F.: 1992, 'Critical Density Layer as Obstacle at Solar Wind-Exosphere Ion Interaction', *Geophys. Res. Lett.* **19**, 645.

Sauer, K., Bogdanov, A. and Baumgartel, K.: 1994, 'Evidence of an Ion Composition Boundary (Protonopause) in Bi-Ion Fluid Simulations of Solar Wind Mass Loading', *Geophys. Res. Lett.* **21**, 2255.

Sauer, K., Bogdanov, A. and Baumgartel, K.: 1995, 'The Protonopause–an Ion Composition Boundary in the Magnetosheath of Comets, Venus and Mars', *Adv. Space Res.* **16**(4), 153.

Sauer, K., Dubinin, E., Baumgartel, K. and Bogdanov, A.: 1996, 'Bow-Shock 'Splitting' in Bi-Ion Flows', *Geophys. Res. Lett.* **23**, 3643.

Sauer, K., Dubinin, E. and Baumgartel, K.: 1998, 'Nonlinear MHD Waves and Discontinuities in the Martian Magnetosheath. Observations and 2D bi-ion MHD Simulations', *Earth Planets Space* **50**, 793.

Sauer, K., McKenzie, E. J. F. and Dubinin, E.: 2000, in M. Verheest, M. Goosens, M. A. Hellberg and R. Bharuthram (eds), *Waves and nonlinear structures in bi-ion plasmas, in: Waves in Dusty,*

Solar and Space Plasmas Vol. 537 *AIP Conference Proceedings*, p. 327, American Institute of Ophysics, Melville, N.Y..

Sauer, K. and Dubinin, E.: 2000, 'The Nature of the Martian 'Obstacle Boundary', *Adv. Space Res.* **26**(10), 1633.

Savich, N. A. *et al.*: 1979, in N. F. Ness (ed) *The nighttime ionosphere of Mars from Mars 4 and 5 radio occultation dual-frequency measurements, Solar Wind Interaction with the Planets Mercury, Venus, and Mars*, NASA Special Publication 397, Washington, DC.

Schunk, R. W. and Nagy, A. F.: 2000, *Ionospheres*, Cambridge University Press.

Schwingenschuh, K., Riedler, W., Yeroshenko, Y. *et al.*: 1987, 'Magnetic-Field Draping in the Comet Halley Coma - Comparison of Vega Observations with Computer-Simulations', *Geophys. Res. Lett.* **14**, 640.

Schwingenschuh, K., Riedler, W., Lichtenegger, H., Yeroshenko, Ye., Sauer, K., Luhmann, J. G., Ong, M. and Russell, C. T.: 1990, 'Martian Bow Shock: Phobos Observations', *Geophys. Res. Lett.* **17**, 889.

Schwingenschuh, K. *et al.*: 1992a, 'The Martian Magnetic Field Environment: Induced or Dominated by an Intrincic Magnetic Field', *Adv. Space Res.* **12**(9), 213.

Schwingenschuh, K. a. W. R.: 1992b, in H. K. Biernat, G. A. Bachmaier, S. J. Bauer and R. P. Rijnbeek (eds), Solar wind interaction with nonmagnetic and weakly magnetized bodies in the solar system. *Proceedings of the Workshop 'The Solar Wind-Magnetosphere System'*, 247.

Shabanskiy, V. P.: 1972, *Phenomena in the Near Terrestrial Space*, Nauka, pp. 167–190, Moscow (in Russian).

Shinagawa, H., Cravens, T. E. and Nagy, A. F.: 1987, 'A One-Dimensional Time-Dependent Model of the Magnetized Ionosphere of Venus', *J. Geophys. Res.* **92**, 7317.

Shinagawa, H. and Cravens, T. E.: 1988, A One-Dimensional Multi-Species Magnetohydrodynamic Model of the Dayside Ionosphere of Venus', *J. Geophys. Res.* **93**, 11263.

Shinagawa, H. and Cravens, T. E.: 1989, 'A One-Dimensional Multispecies Magneto Hydodynamical Model of the Dayside Ionosphere of Mars', *J. Geophys. Res.* **94**, 6506.

Shinagawa, H. and Cravens, T. E.: 1992, 'The Ionospheric Effects of a Weak Intrinsic Magnetic Field at Mars', *J. Geophys. Res.* **97**, 1027.

Shinagawa, H.: 1996, 'A Two-Dimensionsl Model of the Venus Ionosphere, 1. Unmagnetized Ionosphere', *J. Geophys. Res.* **101**, 26911.

Shutte, N. M. *et al.*: 1989, 'Observations of Electron and Ion Fluxes in the Vicinity of Mars with the HARP Spectrometer', *Nature* **341**, 614.

Slavin, J. A., Elphic, R. C. and Russell, C. T.: 1979, 'A Comparison of Pioneer Venus and Venera Bow Shock Observations: Evidence for a Solar Cycle Variation', *Geophys. Res. Lett.* **6**, 905.

Slavin, J. A. and Holzer, R. E.: 1982, 'The Solar Wind Interaction with Mars Revisited', *J. Geophys. Res.* **87**, 10285.

Slavin, J. A., Holzer, R. E., Spreiter, J. R., Stahara, S. S. and Chaussee, D. S.: 1983, Solar Wind Flow about the Terrestrial Planets, 2. Comparisons with Gasdynamic Theory and Implications for Solar Planetary Interactions', *J. Geophys. Res.* **88**, 19.

Slavin, J. A. and Holzer, R. E.: 1983, 'Solar Wind Flow about the Terrestrial Planets 2, Comparison with Gasdynamic Theory and Implications for Solar-Planetary Interactions', *J. Geophys. Res.* **88**, 19.

Slavin, J. A., Smith, E. J. and Intriligator, D. S.: 1984, 'A Comparative Study of Distant Magnetotail Structure at Venus and Earth', *Geophys. Res. Lett.* **11**, 1074.

Slavin, J. A., Smith, E. J., Tsurutani, B. T. *et al.*: 1986, 'Giacobini-Zinner Magnetotail: ICE Magnetic Field Observations', *Geophys. Res. Lett.* **13**, 283.

Slavin, J. A., Schwingenschuh, K., Riedler, W. and Yeroshenko, Ye.: 1991, 'The Solar Wind Interaction with Mars: Mariner 4, Mars 2, Mars 3, Mars 5 and Phobos 2 Observations of Bow Shock Position and Shape', *J. Geophys. Res.* **96**, 11235.

Speiser, T. W.: 1965, 'Particle Trajectories in Model Current Sheets, 1.Analytical Solutions', *J. Geophys. Res.* **70**, 4219.

Spenner, K., Knudsen, W. C., Miller, K. L., Novak, V., Russell, K. L. and Elphic, R. C.: 1980, 'Observation of the Venus Mantle, the Boundary Region Between Solar Wind and Ionosphere', *J. Geophys. Res.* **85**, 7655.

Spreiter, J. R. and Briggs, B. R.: 1962, 'Theoretical Determination of the Form of the Boundary of the Solar Corpuscular Stream Produced by the Interaction with the Magnetic Dipole Field of the Earth', *J. Geophys. Res.* **67**, 37.

Spreiter, J. R. and Stahara, S. S.: 1980: 'A New Predictive Model for Determining Solar Wind – Terrestrial Planet Interactions', *J. Geophys. Res.* **85**(6), 769.

Stewart, A. I.: 1972, 'Mariner 6 and 7 Ultraviolet Ultraviolet Spectrometer Experiment: Implications of CO_2^+, CO, and O Airglow', *J. Geophys. Res.* **77**, 54.

Stewart, A. I. and Hanson, W. B.: 1982, in A. Kliore (ed) Mars Upper Atmosphere: Mean and Variations, in the *Mars Reference Atmosphere, Adv. Space Res.* **2**, 87.

Szegö, K., Glassmeier, K. H., Brinca, A., Bingham, R., Cravens, T., Fischer, C., Fisk, L., Gombosi, T., Harendel, G., Lee, M., Mazelle, C., Moebius, E., Motschmann, U., Isenberg, P., Sauer, K., Shapiro, V., Schwadron, N., Tsurutani, B. and Zank, G.: 2000, 'Physics of Mass Loaded Plasma', *Space Sci. Rev.* **94**, 429.

Szego, K.: 2001, 'Present Understanding of the Dayside Mantle of Venus and Mars', *Adv. Space Res.* **28**, 841.

Trotignon, J. G., Grard, R. and Slavin, S.: 1991, 'Plasma Wave System Measurements of the Martian Bow Shock from the Phobos 2 Spacecraft', *J. Geophys. Res.* **96**, 11253.

Trotignon, J. G., Grard, R. and Skalsky, A.: 1993, 'Position and Shape of the Martian Bow Shock: the Phobos 2 Plasma Wave System Observations', *Planetary Space Sci.* **41**, 189.

Trotignon, J. G., Dubinin, E., Grard, R., Barabash, S. and Lundin, R.: 1996, 'Martian Planetopause as Seen by the Plasma Wave System Onboard Phobos 2, *J. Geophys. Res.* **101**, 24965.

Vaisberg, O. L., Bogdanov, A. V., Smirnov, V. N. and Romanov, S. A.: 1975, 'Initial Results of Ion Flux Measurements by RIEP-2801M Instrument on Mars-4 and Mars-5', *Cosmic Res.* **13**, 112.

Vaisberg, O. L.: 1976, in D. J. Williams (ed) Mars - plasma environment, *Physics of Solar Planetary Environments*, Vol. 2. AGU, Boulder, Colorado, 854.

Vaisberg, O. L.: 1992, in J. G. Luhmann, M. Tatrallyay and R. O. Pepin (eds), The solar wind interaction with Mars: A review of results from early soviet missions to Mars, in *Venus and Mars: Atmospheres, Ionospheres, and Solar wind Interactions*, *Geophys. Monogr.* **66**, NW, Washington, p. 311.

Vasiliev, M. B., Vyshlov, A. S., Kolosov, M. A., Savich, A. I. *et al.*: 1975, 'Preliminary Results of the Two Frequency Radio Sounding of the Martian Ionosphere by Using the Mars Interplanetary Stations in 1974', *Kosmicheskie issledovanija* **13**, 48 (in Russian).

Verigin, M. I., Shutte, N. M., Galeev, A. A., Gringauz, K. I., Kotova, G. A., Remizov, A. P., Rosenbauer, H., Hemmerich, P., Livi, S., Richter, A. K., Apathy, I., Szego, K., Riedler, W., Schwingenschuh, K., Stellar, M. and Yeroshenko, Ye. G.: 1991a, 'Ions of Planetary Origin in the Martian Magnetosphere (Phobos 2/Taus Experiment)', *Planetary Space Sci.* **39**, 131.

Verigin, M. I., Gringauz, K. I., Shutte, N. M., Haider, S. A., Szgo, K., Kiraly, P., Nagy, A. F. and Gombosi, T. I.,: 19916, *J. Geophys. Res.*, **96**, 19307.

Verigin, M. I., Gringauz, K. I., Kotova, G. A., Remizov, A. P., Shutte, N. M., Richter, A., Riedler, W., Schwingenschuh, K., Szego, K., Apathy, I. and Tatrallyay, M.: 1993, 'The Dependence of the Martian Magnetopause and Bow Shock on Solar Wind Ram Pressure According to Phobos 2 TAUS Ion Spectrometer Measurements', *J. Gephys. Res.* **98**, 1303.

Verigin, M., Kotova, G., Shutte, N., Remizov, A., Szego, K., Tatrallyay, M., Apathy, I., Rosenbauer, H., Livi, S., Richter, A. K. Schwingenschuh, K., Zhang, T.-L., Slavin, J. and Lemaire, J.: 1997, 'Quantitative Model of the Martian Magnetopause Shape and its Variation with the Solar Wind Ram Pressure Based on Phobos 2 Observations', *J. Geophys. Res.* **102**, 2147.

Verigin, M. I., Kotova, G. A., Remizov, A. P., Styazhkin, V. A., Shutte, N. M., Zhang, T.-L., Riedler, W., Rosenbauer, H., Szego, K., Tatrallyay, M. and Schwingenschuh, K.: 1999, 'Shape and Location of Planetary Bow Shocks', *Cosmic Res.* **37**, 34.

Verigin, M. I., Kotova, G. A., Remizov, A. P., Szegö, K., Tátrallyay, M., Slavin, J., Rosenbauer, H., Livi, S., Riedle, W., Schwingenschuh, K. and Zhang, T.-L.: 2001, 'Evidence of the Influence of Equatorial Martian Crustal Magnetization on the Position of the Planetary Magnetotail Boundary by Phobos 2 Data', *Adv. Space Res.* **28**(6), 885.

Vignes, D. *et al.*: 2000, 'The Solar Wind interaction with Mars: Locations and Shapes of the Bow Shock and the Magnetic Pile-up Boundary from the Observations of the MAG/ER Experiment Onboard Mars Global Surveyor', *Geophys. Res. Lett.* **27**, 49.

Vignes, D., Acuña, M. H., Connerney, J. E. P., Crider, D. H., Mazelle, C. and Rème, H.: 2002, 'Factors Controlling the Location of the Bow Shock at Mars', *Geophys. Res. Lett.* **29**, 9, 42, 1328 doi: 10.029/2001 GL014513.

Wallis, M. K.: 1978, 'Exospheric Density and Escape Fluxes of Atomic Isotopes on Venus and Mars', *Planetary Space Sci.* **26**, 949.

Whitten, R. C.: 1970, 'The Daytime Upper Atmosphere of Venus', *J. Geophys. Res.* **75**, 3707.

Yeroshenko, Ye., Riedler, W., Schwingenschuh, K., Luhmann, J. G., Ong, M. and Russell, C. T.: 1990, 'The Magnetotail of Mars: Phobos 2 Observations', *Geophys. Res. Lett.* **17**(6), 885–888.

Zakharov, A. V.: 1992, in J. G. Luhmann, M. Tatrallyay and R. Pepin (eds), The plasma environment of Mars: Phobos mission results, *Venus and Mars: Atmospheres, Ionospheres, and Solar Wind Interactions*, p. 327, *Geophysical Monograph* **66**, Washington, D.C..

Zhang, T. L., Luhmann, J. G. and Russell, C. T.: 1990a, 'The Solar Cycle Dependence of the Location and Shape of the Venus Bow Shock', *J. Geophys. Res.* **95**, 14961.

Zhang, M. H. G., Luhmann, J. G. and Kliore, A. J.: 1990b, 'An Observational Study of the Nightside Ionospheres of Venus and Mars with Radio Occultation Methods', *J. Geophys. Res.* **95**, 17095.

Zhang, M. H. G., Luhmann, J. G. and Kliore, A. J.: 1990c, 'A Post-Pioneer Venus Reassessment of the Martian Dayside Ionosphere as Observed by Radio Occultation Methods', *J. Geophys. Res.* **95**, 14829.

Zhang, T. L., Luhmann, J. G. and Russell, C. T.: 1991, 'The Magnetic Barrier at Venus', *J. Geophys. Res.* **96**, 11145.

Zhang, M. H. G., Luhmann, J. G., Nagy, A. F., Spreiter, J. R. and Stahara, S. S.: 1993a, 'Oxygen Ionization Rates at Mars and Venus: Relative Contributions of Impact Ionization and Charge Exchange', *J. Geophys. Res.* **98**, 3311.

Zhang, M. H. G., Luhmann, J. G., Bougher, S. W. and Nagy, A. F.: 1993b, 'The Ancient Oxygen Exosphere of Mars: Implication for Atmospheric Evolution', *J. Geophys. Res.* **98**, 10915.

Zhang, T. L., Schwingenschuh, K., Russell, C. T., Luhmann, J. G., Rosenbauer, H., Verigin, M. I. and Kotova, K.: 1994, 'The Flaring of the Martian Magnetotail Observed by the Phobos 2 Spacecraft', *Geophys. Res. Lett.* **21**, 1121.